Annual Report 2003

Address:	Prof. Dr. Burkard Hillebrands Fachbereich Physik Technische Universität Kaiserslautern Erwin-Schrödinger-Straße 56 67663 Kaiserslautern, Germany Tel.: +49-(0)631-205-4228 Fax.:+49-(0)631-205-4095
Postal address:	Postfach 3049 67653 Kaiserslautern, Germany
Internet:	http://www.physik.uni-kl.de/hillebrands/
E-Mail:	hilleb@physik.uni-kl.de

Our Group

From left to right:

Oskar Liedke, Bernd Pfaff, Sybille Müller, Alexander André,
Dr. Sergej O. Demokritov, Dr. Q.F. Xiao, Markus Weber,
Dr. Kurt Jung, Steffen Blomeier, Dr. Alexander Serga,
Dr. Vladislav Demidov, Dr. Galina Khlyap, Dr. Mikhail Kostylev (guest),
Andreas Beck, Dr. Mireia Blanco-Mantecón, Patricia Martin Pimentel,
Markus Laufenberg (guest), Christian Bayer, Dr. Jürgen Fassbender,
Hans Nembach, Dr. Björn Roos, Heike Schuster,
Dr. Thomas Wittkowski, Martin Rohmer, Dieter Weller,
Prof. Dr. Burkard Hillebrands

Contents

Chapter 1: Introduction

Dear colleagues and friends,

again we report on our research from the last twelve months, the period of November 2002 to October 2003. Our university changed its name and is now a “Technische Universität” (University of Technology) to better account for the focus on technology and natural sciences. As a consequence, the university’s corporate identity was brought to an up-to-date standard which also affects our Annual Report: you might notice that this year we have a new cover using the new university layout.

We continue to work mostly in the field of magnetization dynamics and ion modification in magnetic systems, fields which generated a lot of interest in the last years. In recent years we have moved from studies of eigen modes in small magnetic objects to dynamical properties in general, and tried to establish the field of nonlinear spin waves in the general field of nonlinear wave phenomena. A highlight is the discovery of symmetry breaking modes in an active ring structure, which we were able to make after the development of phase sensitive parametric amplification. As one example we studied so-called “Möbius” solitons, which need to travel twice about the ring to meet the initial phase condition. We studied the process of spin wave reflection and transmission from a region with a local field inhomogeneity and observed spin wave tunneling. In advancing our experimental capabilities we have developed the technique of micro-Brillouin-light-scattering allowing us now to investigate single micrometer sized magnetic elements. Progress was also made in the field of ion irradiation of magnetic systems. We showed how modification of the coupling in exchange bias system can be achieved by short heating pulses from a laser. In the Fe/Cr/Fe-trilayer system we demonstrate the potential to magnetically pattern such structures on small length scales using a focused ion beam machine.

Much of this work is embedded in the German priority program (“Schwerpunktprogramm”) entitled “Ultrafast magnetization processes” funded by the Deutsche Forschungsgemeinschaft as well as by the European Community Research Training Networks on “Ultrafast Magnetization Processes in Advanced Devices” (ULTRASWITCH) and “New Exchange Bias Systems for Advanced Magnetic Devices” (NEXBIAS). A third Research Training Network on “Ultrasmooth Magnetic Layers for Advanced Devices”is currently in negotiation with the European Community and addresses new techniques for preparing ultra-smooth magnetic films for magnetic sensors. Applied work was conducted in the European IST network “Low Power Magnetic Random Access Memory with optimised Writing Time and Level of Integration” (NEXT). Since beginning of 2003 a new research center “Materialien für Mikro- und Nanosysteme” has been established at our University providing a basis for local funding.

Both Sergej Demokritov and Jürgen Fassbender received a call on new positions: Sergej received a call on an associate professor position in the United States, which he had to refuse for sudden personal reasons. Jürgen received an offer for a deputy research director position at the Institut für Ionenstrahlphysik und Materialbearbeitung in Dresden. Congratulations to both!

Kurt Jung, who worked in our group since its beginning in 1995 on the position of an “Akademischer Oberrat” and later of an “Akademischer Direktor” took early retirement and left the group end of September. We wish him all the best for his new time.

Two members of our group received their Ph.D.: Tim Mewes, who then started a post-doctoral stay in the group of Chris Hammel in Ohio, and Stefan Poppe, who took a senior reseacher position at the reseach centrum C.E.A.S.A.R. in Bonn.

Our work would not have been possible without valuable collaborations with people all over the world. They are too many to list them here all. In particular we would like to thank, in alphabetical order, Dima Berkow, Harry Bernas, Klaus Bewilogua, John Chapman, Claude Chappert, Darrell Comins, Hajo Elmers, Claude Fermon, Jacques Ferré, Colm Flannery, Paulo Freitas, Loris Giovannini, Volker Herzog, Boris Kalinikos, Gregor Kiefel, Mikhail Kostylev, Natalia Kreines, Norbert Lampe, Wolfram Maaß, Jan Marien, Günter Marx, Roland Mattheis, Andrezj Maziewski, Jacques Miltat, Alexandra Mougin, Fabrizio Nizzoli, Josep Nogues, Carl Patton, Günter Reiss, Günter Reiße, Frank Richter, John R. Sandercock, Gerd Schönhense, Andreas Schreyer, Andrei Slavin, Bob Stamps, André Thiaville, Stefan Visnovsky and Steffen Weißmantel for their interactions with us and their strong input to our work. Collaborations within the Fachbereich Physik at the University of Kaiserslautern (Martin Aeschlimann, Michael Fleischhauer, Henning Fouckhardt, Wolfgang Hübner, Herbert Urbassek, Richard Wallenstein, Sandra Wolff, Christiane Ziegler and their groups), the Institut für Oberflächen- und Schichtanalytik as well as the newly established Nano+Bio-Center have been very stimulating. It was a pleasure to work together with Lumera Lasers GmbH (Rolf Knappe) in setting up our new pulsed laser system. I am especially grateful to Heinz Busch and Udo Grabowy and their start up company NTTF GmbH for the close contact. I am much obliged to Stefan Sattel and his team from the TZO GmbH for providing convenient general conditions for our work in Rheinbreitbach.

I would also like to thank all our sponsors, which are the Deutsche Forschungsgemeinschaft, the Bundesministerium für Bildung, Wissenschaft, Forschung und Technologie, the Humboldt Foundation, the Deutscher Akademischer Austauschdienst, the European Community, INTAS, the State of Rheinland-Pfalz and the University of Kaiserslautern. My special thanks go to Andreas Beck and Sibylle Müller for their help in preparing this report.

It is my special pleasure to greet all former group members. May this report help to stay in touch with each other.

If you are interested in our work I would be happy to hear from you. If you have any questions, comments, suggestions, or any kind of criticism, please contact us.

With all my best wishes for Christmas, and a Happy New Year,

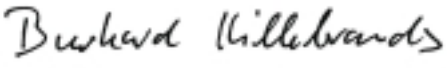

Kaiserslautern, November 2003

Chapter 2: Personnel

2.1 Members of the group

Group leader:

Prof. Dr. Burkard Hillebrands

Senior scientists:

Dr. habil. Sergej Demokritov, Hochschuldozent	
Dr. habil. Jürgen Fassbender, Privatdozent	
Dr. Kurt Jung, Akad. Direktor	until 09/03

Postdocs:

Dr. Mireia Blanco-Mantecón	
Dr. Vladislav Demidov	
Dr. Stefan Poppe	until 08/03
Dr. Marc Rickart	until 12/02
Dr. Alexander Serga	
Dr. Q.F. Xiao	since 07/03
Dr. Galina Khlyap	since 10/03
Dr. Björn Roos	since 08/03
Dr. Thomas Wittkowski	

PhD students:

Dipl.-Phys. Christian Bayer	since 02/03
Dipl.-Phys. Andreas Beck	
Dipl.-Phys. Lisa Kleinen (Rheinbreitbach)	
Dipl.-Phys. Patricia Martin Pimentel	since 08/03
Dipl.-Phys. Tim Mewes	until 11/02
Dipl.-Phys. Hans Nembach	
Dipl.-Phys. Maciej Oskar Liedke	since 11/02
Dipl.-Phys. Stefan Poppe	until 05/03
Dipl.-Phys. Martin Rohmer	since 04/03
Dipl.-Phys. Markus Weber	since 11/02

Diploma Students:

Alexander André	since 03/03
Steffen Blomeier	since 12/02
Dirk Hoffmann	since 09/03

Engineers and Technicians

Günther Moog (Rheinbreitbach)
Bernd Pfaff
Dipl.-Ing. (FH) Dieter Weller

Secretaries:

Sibylle Müller
Heike Schuster (Forschungsschwerpunkt MINAS)

2.2 Visiting scientists, postdoctoral fellows and exchange students

Prof. Boris Kalinikos, Electrotechnical University St. Petersburg,
St. Petersburg, Russia — 21.11.02 - 22.11.02, 12.05.03 - 13.05.03

Boris spent two short research stays in Kaiserslautern as a part of our cooperation in the frame of an INTAS project. Discussions with him have helped us a lot in understanding the origin of non-linear excitations in active rings.

Prof. Robert L. Stamps, Department of Physics,
University of Western Australia, Perth, Australia — 30.10.03 - 02.11.03

Bob spent a short research stay in Kaiserslautern. He helped a lot in understanding ion irradiation induced modifications of the exchange bias effect. He was also involved in the interpretation of magnetization dynamics results.

Prof. J. Darrell Comins, Department of Physics,
University of the Witwatersrand, Johannesburg, South Africa — 07.07.03 - 06.08.03

Darrell spent one month in Kaiserslautern, working successfully on the interpretation of resonant surface excitations guided in layered structures and their utilization for the determination of material parameters. Essential progress in the preparation of a comprehensive review article on surface Brillouin scattering from bulk solids and layered structures has been achieved.

Prof. Andrei Slavin, University of Rochester, Michigan, U.S.A. — 04.06.03 - 22.06.03

Andrei spent a short research stay in our lab. He was heavily involved in the modelling of localized modes of spin wave wells created in confined magnetic objects.

Dimitry Kholin, Ph.D. student, Institute for Physical Problems,
Moscow, Russia — 16.02.03 - 20.03.03

Dimitry is working on the fundamental properties of biquadratic and non-collinear coupling in layered magnetic systems. He investigates the interplay between the type of the coupling and the morphology of interfaces.

Dr. Mikhail Kostylev, Electronics Faculty,
St. Petersburg Electrotechnical University St.Petersburg, Russia — since 15.09.03

Mikhail is working on the problem of nonlinear spin waves financed by a DFG project. In particular he works on theory of spin-wave parametric amplification and generation in magnetic films and magnetic-film-based active resonators by using pulsed microwave parallel magnetic pumping.

Markus Laufenberg, Ph.D. student,

INESC Microsistemas e Nanotecnologias, Lisboa, Portugal 06.10.03 - 24.10.03

Markus has prepared samples for our magnetooptical experiments on the current induced transfer of magnetic momentum. During his short stay in Kaiserslautern, which was a secondment within the EU founded ULTASWITCH project, he was also involved in the Brillouin light scattering investigations of the prepared samples.

2.3 Guest seminars

Prof. Theo Rasing 17.02.03	Faculty of Natural Sciences, Math. and Informatics, University of Nijmwegen, Niederlande *Ultrafast magnetization dynamics and switching* Physikalisches Kolloquium
Dr. Xiao Qunfeng 12.05.03	Van der Waals-Zeeman Institute, Amsterdam, The Netherlands *Experimental study of nanoscale exchange coupling* Sonderkolloquium
Prof. Robert D. Shull 13.06.03	NIST, Gaithersburg, MD, USA *Magnetic images of magnetization reversal in exchange-biased bilayers* Sonderkolloquium
Dr. Claude Chappert 16.06.03	CNRS, Université Paris-Sud, Orsay, France *Ultrafast switching of magnetic nanostructures: fundamentals and applications* Physikalisches Kolloquium
Prof. J. Darrell Comins 21.07.03	Department of Physics, University of the Witwatersrand, Johannesburg, South Africa *High temperature light scattering in superionic fluorides* Sonderseminar
Dr. Radek Lopusnik 12.08.03	NIST, Boulder, Colorado, USA *Magnetization dynamics study in ferromagnetic and semiconductor materials* Sonderkolloquium
Dr. Britta Hausmanns 07.10.03	Universität Duisburg-Essen *Magnetowiderstand und Ummagnetisierungsprozesse in einzelnen nanostrukturierten magnetischen Leiterbahnen* Sonderkolloquium
Prof. Robert L. Stamps 30.10.03	University of Western Australia, Australia *Five orders of dynamics: spin processes at* 10^{-6} *to* 10^{-10} *meters* Kolloquium des Schwerpunktes Materialien für Mikro- und Nanosysteme

2.4 Visits of group members at other laboratories

Steffen Blomeier	University of Glasgow, United Kingdom 27.03.-27.04.09 Host: Prof. Dr. J. Chapman
Christian Bayer	University of Minnesota, USA 02.04.-25.09.03 Host: Prof. P. Crowell
Steffen Blomeier	University of Glasgow, United Kingdom 17.08.-14.09.09 Host: Prof. Dr. J. Chapman
Alexander André	Oakland University, Rochester, USA 31.10.03-30.11.03 Host: Prof. Dr. A.N. Slavin
Sergej O. Demokritov	University Perugia, Italy 06.03.03-20.03.03 Host: Dr. J. Gubbiotti

2.5 Group member photo gallery

Alexander André
Diploma student

Christian Bayer
Ph.D. student

Andreas Beck
Ph.D. student

Dr. Mireia Blanco-Mantecón
Postdoc

Steffen Blomeier
Diploma student

Dr. Vladislav Demidov
Postdoc

Dr. habil. Sergej O. Demokritov
Senior scientist and lecturer

Dr. habil. Jürgen Fassbender
Senior scientist and lecturer

Prof. Dr. Burkard Hillebrands
Group leader

Dirk Hoffmann
Diploma student

Dr. Kurt Jung
Senior scientist

Lisa Kleinen
Ph.D. student

Dr. Galina Khlyap
Postdoc

Maciej Oskar Liedke
Ph.D. student

Patricia Martin Pimentel
Ph.D. student

Dr. Tim Mewes
Postdoc

Günther Moog
Technician

Sibylle Müller
Secretary

Hans Nembach
Ph.D. student

Bernd Pfaff
Technician

Dr. Stefan Poppe
Postdoc

Dr. Marc Rickart
Postdoc

Martin Rohmer
Ph.D. student

Dr. Björn Roos
Postdoc

Heike Schuster
Secretary

Dr. Alexander Serha
Senior scientist

Markus Weber
Ph.D. student

Dieter Weller
Mechanical engineer

Dr. Thomas Wittkowski
Postdoc

Dr. Q.F. Xiao
Postdoc

Chapter 3: Research Topics

The field of magnetism in films and multilayers is currently one of the strongest developing areas in modern solid state physics. This is caused both by the challenging developments in the discovery and understanding of the basic physical phenomena, and by the strong impact into industrial applications in the areas of sensors and information storage technology. New mechanisms like interlayer exchange coupling, the giant magnetoresistance effect, the room-temperature tunneling magnetoresistance effect, and, since very recently, spin current phenomena were discovered all within the last one and a half decade. Applications based on these effects were developed, like the magnetic read head based on the giant magnetoresistance effect found in nearly every hard disk drive sold nowadays. The combination with microelectronics, the so-called field of magnetoelectronics is strongly expanding and bridging the gap between conventional magnetism and semiconductor physics in view of potential applications in sensor devices and magnetic random access memories.

Most of our research projects are in this field. A main focus is on spin dynamics. We study the eigen-frequency spectrum of excitations of the magnetization on the frequency scale using the Brillouin light scattering technique, and the temporal evolution by time resolved magneto-optic methods. We investigate high frequency properties like spin waves, time dependent magnetization effects, and fast magnetic switching.

A key issue is the fabrication of high-quality epitaxial film and multilayer systems and devices using molecular beam epitaxy as prototype systems to study fundamental problems.

In the field of applications we address problems of fast magnetic switching, the exchange bias effect and tunneling magnetoresistance. We transfer our results into actual devices by working closely together with industrial partners.

Magnetic films are very attractive and versatile nonlinear media. Considering spin waves in films as one example of nonlinear waves we study nonlinear effects which are of a great importance for nonlinear science in general.

As a second working area we develop and investigate carbon films for medical applications in the framework of the Institute for Thin Film Technology in Rheinbreitbach. A special focus is on the determination of elastic properties of hard coating materials.

Overview on projects

1) Epitaxial magnetic films and multilayers: growth, structure and magnetic properties

The preparation of samples with highest possible structural quality and characterization is very important to be able to study magnetic phenomena with the necessary precision. We achieve this by using molecular beam epitaxy employing the standard *in-situ* methods for chemical and structural analysis. They comprise Auger spectroscopy for chemical analysis, low and high energy electron diffraction, and *in-situ* scanning tunneling and atomic force microscopy. To characterize the magnetic properties we perform *in-situ* Brillouin light scattering spectroscopy and magneto-optic Kerr effect magnetometry. *Ex-situ*, the samples are investigated using Brillouin light scattering, vector Kerr magnetometry, vibrating sample magnetometry, and more. Scientific subjects are magnetic anisotropies induced at interfaces and by controlled defects, and interlayer coupling effects between magnetic films in multilayers. Special attention is paid

to the interplay between the morphology at the interfaces (atomic defects, steps, roughness and interdiffusion) and the magnetic properties.

2) Surface smoothing

It is very important to fabricate films and multilayers with maximum degree of smoothness. Undesirable roughness, for example, results in a reduced figure of merit in magnetoelectronic devices. We develop a technology to smooth surfaces of the films after their preparation. For this purpose we use low-energy beams of argon ions. Mono-energetic, low-energy ions allow for a very controllable smoothing process of the surface without creation of an essential number of defects.

3) Dynamic magnetic properties of laterally patterned nanostructures

We investigate the basic magnetic properties of systems patterned on the micrometer to nanometer scale. In particular we focus on the domain structure and the change in the spin wave mode spectrum due to lateral confinement effects. We have developed a Brillouin light scattering setup, operating in a Fourier microscope like mode, to obtain sub-micrometer scale spatial information about the distribution of dynamic excitations in small magnetic objects. We also developed a micro-focus Brillouin light scattering system to investigate single magnetic elements. Using those methods we have observed lateral quantization of spin waves in magnetic stripes and rectangular elements. Main results are the observation of quantized modes and of edge modes existing in areas with a large internal field gradient, and static and dynamic coupling effects between magnetic objects. The experiments are accompanied by numerical simulations.

4) Nonlinear properties of high-amplitude spin waves

Spin waves with high precession angles are an interesting object for the investigation of general effects of nonlinear wave propagation in dispersive, anisotropic, and dissipative media. Contrary to nonlinear optical pulses, the spectrum of spin waves can be easily manipulated, by, e.g., changing the orientation and the value of the applied magnetic field. In addition spin waves are much slower than light pulses making their observation easier.

Using the time-resolved Brillouin light scattering technique developed in our lab, we measure the intensity distribution of spin waves propagating in a magnetic film with spatial and temporal resolution. Central problems are: the amplification of spin waves in the linear and nonlinear intensity regimes, the formation of instabilities (e.g. self-focusing), the propagation of nonlinear excitations (solitons, magnetic “bullets”) and excitations in nonlinear media with a nontrivial topology such as rings. An important development of these studies is the investigation of self-generation of solitons and bullets in loops with an electronic feedback, the development of a spin wave soliton “laser”, and the discovery of symmetry-breaking spin wave modes like the “Möbius” solitons.

5) Fast magnetic switching

For memory devices it is of special importance how fast and secure magnetic domains can be written and the magnetization of a single magnetic object can be reversed. The corresponding time scale is in the picosecond to nanosecond regime. In order to investigate these phenomena a time-resolved scanning magneto-optic Kerr microscope has been constructed. The time evolution of the magnetization is sensed stroboscopically. The magnetization dynamics, spin

wave propagation effects and in particular the switching behavior of thin magnetic films and nanostructures are investigated.

6) Magnetic nanopatterning

Light ion irradiation is an excellent tool to locally modify magnetic properties on the submicrometer scale, without affecting the surface topography. This effect is used to magnetically pattern ultrathin films and multilayers using resist masks patterned by electron beam lithography. The major difference between this technique and conventional lithographic techniques is that the environment of the nanostructures can also be magnetic (paramagnetic, antiferromagnetic). A focus is on coupled magnetic systems, such as exchange bias bilayers and exchange coupled trilayers. Using a focused ion beam we were able to pattern epitaxial Fe/Cr/Fe(001) trilayers changing the the sign of the interlayer coupling with a lateral resolution better than 200 nm.

7) Exchange bias systems

The investigation of exchange bias systems is of fundamental as well as technological importance. The effect is a shift of the hysteresis loop along the field axis, and it appears in multilayers of coupled ferromagnetic and antiferromagnetic films. We study in particular structurally well characterized epitaxial bilayers. The role of defects and interfacial mixing is investigated using ion irradiation in order to artificially create disorder. Ion irradiation techniques are also applied to modify the magnitude and direction of the exchange bias field. TEM studies are carried out to investigate the structural and magnetic properties as well as their dependency on the irradiation with He^+ and Ga^+ ions. A picosecond all-optical pump-probe setup was developed to study thermal activated unpinning of the exchange coupling at the FM/AFM interface. This is of high technological interest, especially for magnetic sensor and storage applications.

8) Elastic properties of hard, super-hard and inhomogeneous films and multilayers

We prepare hard and super-hard films and investigate their elastic properties using Brillouin light scattering. Research subjects are amorphous carbon (a-C:H and ta-C:H) and boron nitride films, which are prepared using unbalanced magnetron sputtering. The elastic constants are determined from the dispersion curves of surface and film phonons (Rayleigh and Sezawa modes). One of our aims is to prepare hard and super-hard films with minimized internal stresses.

9) Biofunctionalized surfaces for medical applications

Amorphous thin carbon films are known to be very biocompatible, and they can be prepared by various deposition techniques to qualify for miscellaneous applications in the biological and medical field. At the Institute for Thin Film Technology we develop in close collaboration with our spin off company NTTF GmbH biocompatible and biofunctionalized surfaces for medical implants, surgical instruments and cellbiological equipment. Currently we are working on carbon coatings for endwelling catheters and cell culture dishes (both made of temperature sensitive polymers) as well as on the development of diffusion barrier coatings on polymers.

Chapter 4: Equipment

A) Preparation and characterization of thin films and multilayers

1. multi–chamber molecular beam epitaxy system (Pink GmbH) comprising
   a. deposition chamber
      (electron beam and Knudsen sources, RHEED, LEED, Auger)
   b. scanning tunneling and atomic force microscopy chamber
      (*in-situ* STM/AFM, Park Scientific)
   c. Brillouin light scattering and Kerr magnetometry chamber
      (magnetic field 1.2 T, temperature range 80 – 400 K)
   d. load lock chamber
   e. preparation chamber
      (optical coating, heating station 2300°C)
   f. transfer chamber
   g. atom beam oxidization chamber with *in-situ* four-probe resistively measurement stage
2. two-chamber UHV multideposition system
   a. deposition chamber
      (electron beam and Knudsen sources, LEED, Auger)
   b. ion beam sputtering chamber with ion beam oxidation module and mask system
3. two-chamber UHV deposition system with *in-situ* 5 keV ion beam irradiation station
4. two-magnetron sputtering system for hard coatings
5. atomic force microscope (Solver, NT-MDT)
6. clean room facility with flow box, spin coater, etc.

B) Magnetic characterization

1. vibrating sample magnetometer with alternating gradient magnetometer option
   (magnetic field 1.6 T, room temperature)
2. vibrating sample magnetometer
   (magnetic field 5 T, temperature range 2 – 350 K)
3. two vector Kerr magnetometers
   (longitudinal and transverse Kerr effect, magnetic field 1.2 T, temperature range 2 – 350 K, automated sample positioning)
4. high-field polar Kerr magnetometer
   (magnetic field 5 T, temperature range 2 – 350 K)
5. time-resolved vector Kerr magnetometer (10 ps time resolution and microwave setup for generation of short field pulses)
6. scanning Kerr microscope with time resolution
7. picosecond all-optical pump-probe setup (adjustable delay up to 6 ns; ps-laser Lumera Lasers GmbH)

8. magnetic force microscope with magnet (NT-MDT)
9. two Brillouin light scattering spectrometers, computer controlled and fully automated (magnetic field 2.2 T) with stages for
   a. low temperature measurements ($2 - 350$ K)
   b. space-time resolved measurements for spin wave intensity mapping (resolution 50 µm, 0.83 ns)
   c. micro-focus measurements (focus diameter 0.5 µm)
   d. *in-situ* measurements
   e. elastic measurements
10. microwave setup (up to 32 GHz) comprising a network analyzer, microwave amplifiers, modulators, pulse generators, etc.
11. magnetotransport setups (magnetic field 1.5 T, temperature range $20 - 400$ K)

C) Equipment at the Institute for Thin Film Technologies (IDST), Rheinbreitach

1. Preparation of thin films:
   a. chemical vapor deposition (CVD) facility
   b. physical vapor deposition (PVD) facility
   c. plasma enhanced CVD (PECVD) facilities with an inductively coupled rf-plasma beam source and several magnetrons of different sizes
2. Surface and thin film analysis:
   a. profilometer: measurement of coating thickness and roughness determination of intrinsic stress and Young modulus
   b. Ball on Disk: measurement of friction coefficient analysis of surface friction
   c. Revetest: determination of adhesive strength analysis of microcracks
   d. microindention: determination of plastic and elastic microhardness (Vickers)
   e. optical contact angle measurement: determination of solid surface free energy and surface tension evaluation of hydrophobicity and hydrophilicity
   f. reflection- and transmission-spectroscopy (UV-VIS): optical measurements with wavelength range from 185 nm to 915 nm (resolution 1 nm), determination of absorption coefficient and optical gap (Tauc)
   g. (environmental) scanning electron microscopy (ESEM)[1]: comprehensive structural microanalysis of conducting, isolating, anorganic, organic and wet samples
   h. energy dispersive X-ray microanalysis (EDX)[1]: non-destructive fast analysis of elements
   i. neutron activation analysis (NAA)[2]: qualitative und quantitative analysis of main and trace components
   j. elastic recoil detection analysis (ERDA)[2]: analysis of trace elements with depth resolution analysis of hydrogen content

[1] in cooperation with NTTF GmbH, Rheinbreitbach

[2] (accelarator enhanced analysis in cooperation with the accelarator laboratories of the Universities of Munich, Bonn and Cologne

k. Rutherford Backscattering (RBS)[2]: analysis of trace elements with depth resolution
l. synchrotron-X-ray-fluorescence (SYXRF)[2]: non-destructive analysis of elements

Chapter 5: Transfer of Technology

1. Magnetism

With our facilities within the Department of Physics at the University of Kaiserslautern we offer consultance and transfer of technology in the areas of thin film magnetism, magnetic film structures and devices, magnetic sensors, and in corresponding problems of metrology.

We are equipped to perform magnetic, transport, elastic and structural measurements of films and multilayer systems.

This is in detail:

- magnetometry (magnetic field up to 5 T, temperature range 2 - 400 K) using vibrating sample magnetometry, Kerr magnetometry, Brillouin light scattering spectroscopy
- magnetic anisotropies, optionally with high spatial resolution
- magneto-transport properties
- test of homogeneity of magnetic parameters
- exchange stiffness constants in magnetic films
- elastic constants
- surface topography

2. Institut für Dünnschichttechnologie (IDST) - Transferstelle der Technischen Universität Kaiserslautern, Rheinbreitbach

(Institute for Thin Film Technology - Center for Technology Transfer of the University of Kaiserslautern, Rheinbreitbach)

As part of technology transfer the Institute of Thin Film Technology (IDST) offers among other activities

- consultance in tribological problems
- development of product specific coatings
- optimization of coatings especially for medical applications
- coating of polymers and temperature sensitive materials
- coating of samples and small scale production series
- management for R&D-projects

The institute is located in Rheinbreitbach about 20 km south of Bonn in the Center for Surface Technologies (TZO) to support the economy in the northern part of the Rheinland-Pfalz State.

Address:

Institut für Dünnschichttechnologie
Maarweg 30-32
53619 Rheinbreitbach, Germany

Scientific director:

Prof. Dr. B. Hillebrands phone: +49 631 205 4228
e-mail: hilleb@physik.uni-kl.de

Contact:

Lisa Kleinen phone: +49 2224 900 693
fax: +49 2224 900 694
e-mail: kleinen@physik.uni-kl.de

Please contact us for more information.

Chapter 6: Experimental Results

A. Dynamic Magnetic Phenomena

6.1 Reflection and tunneling of spin waves through a region of inhomogeneous magnetic field

S.O. Demokritov, A.A. Serga, A. Andre, V.E. Demidov, M.P. Kostylev, and B. Hillebrands[1]

Propagation of spin waves in an inhomogeneous magnetic field was discussed for the first time in the sixties [1–4]. It was Schlömann, who first realized a close similarity between spin wave propagation and a quantum mechanical particle [1]. In fact, neglecting the magnetic dipole interaction and magnetic anisotropies, the Landau-Lifshitz equation describing magnetization dynamics can be rewritten in the form of the Schrödinger equation with the dynamic magnetization $m \propto \exp(i\omega t)$ being the wave function and the magnetic field playing the role of potential energy:

$$-\frac{2A}{M_S}\frac{\partial^2 m}{\partial z^2} + H(z)m = \frac{\omega}{\gamma}m \quad , \tag{1}$$

where A is the exchange stiffness, M_S is the saturation magnetization, and γ is the gyromagnetic ratio of the medium. For the simplest case of an unconfined magnetic medium the dispersion spectrum of a plane spin wave $(m \propto \exp(iqz))$ can be then written as:

$$h\nu = \hbar\omega = \Delta(z) + \frac{2\hbar\gamma A}{M_S}\,q^2 \quad , \tag{2}$$

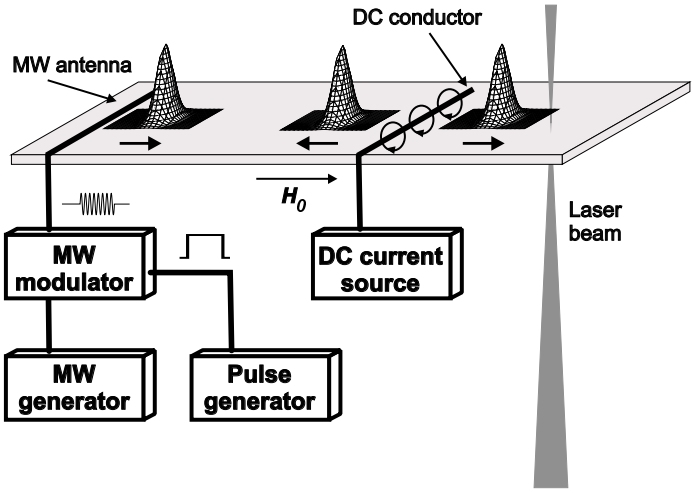

Fig. 1: Schematic layout of the Brillouin light scattering setup in the forward scattering geometry with space and time resolution for the study of spin wave propagation through an inhomogeneous magnetic field. For a discussion of the components see the main text.

[1] In collaboration with A.N. Slavin, Department of Physics, Oakland University, Rochester, Michigan, USA.

where $\Delta(z) = \hbar\gamma H(z)$ is the gap of the spectrum, which is reminiscent to the dispersion of a particle in a potential field $U(z)$,

$$E = U(z) + \frac{\hbar^2}{2m} q^2 \quad . \tag{3}$$

Thus, if a spin wave of frequency ω enters a region where the field $H = H(z)$ varies, i.e., where the gap $\Delta(z)$ is nonzero in Eq. (2), the wave keeps propagating through the inhomogeneous field, albeit with changing wavevector, $q = q(z)$ to fulfill the dispersion law Eq. (2). However, if the value of the gap locally exceeds the value of the initial energy of the spin wave, there exists no real wavevector anymore to fulfill the dispersion law for the given frequency ω. The wave is reflected from this region, which thus can be considered as a potential barrier for the wave. Recently it was shown that a strongly inhomogeneous internal field in magnetic micro-stripes resulting from demagnetizing effects can cause turning points within the stripe which reflect spin waves and thus create a spin wave well [5–7].

A quantitative analysis of the spin wave reflection from a field inhomogeneity taking into account only the exchange interaction and neglecting the magnetic dipole interaction shows that the dynamic magnetization beyond the turning point is not zero: it just changes its dependence on z from sinusoidal ($m \propto \exp(iqz)$) to exponential ($m \propto \exp(-\lambda z)$) [4]. The spin waves tunnel through the barrier.

Here we present a study of spin wave propagation in a magnetic film and the reflection from a region with local field inhomogeneity. Contrary to previous studies [1, 2, 5] the magnetic dipole interaction dominantly determines the properties of spin waves under consideration. We show that, if the forbidden region is narrow enough, an essential spin wave tunneling process takes place. We investigate the mechanism of the tunneling and demonstrate that it has a magnetic dipole origin.

The used experimental setup is schematically shown in Fig. 1. Spin wave packets in a transparent yttrium ion garnet (YIG) film on a gallium gadolinium garnet (GGG) substrate are generated by a microstrip antenna and are detected using the time- and space-resolved Brillouin light scattering (BLS) technique [8]. Both the homogeneous external field and the static magnetization are oriented in the plane of the film parallel to the propagation direction of the spin waves, z. In this case the dynamic magnetization components are m_x and m_y. Such an orientation of the field and the magnetization corresponds to the magneto-static backward volume wave (MSBVW) geometry, characterized by a negative group velocity of the spin waves [9]. The microwave excitation part consists of a microwave generator and a modulator, which is controlled by a pulse generator (pulse length $10 - 30\,\mathrm{ns}$) and connected to the antenna situated on the YIG strip for spin wave generation. MSBVW spin-wave packets are generated with a carrier frequency $\omega = 2\pi \cdot 7.095\,\mathrm{GHz}$ and a carrier wavevector $q = 210 - 220\,\mathrm{cm}^{-1}$, the value of q being determined by the dispersion relation of the spin wave in an external field of $H_0 = 1840\,\mathrm{Oe}$. A narrow conductor of $50\,\mu\mathrm{m}$ diameter mounted across the film carrying a dc-current is used to create a local inhomogeneous field, $H_j(z)$. Depending on the direction of the dc-current, the total field (and, thus, the gap of the spin wave spectrum) is locally either enhanced or reduced by the Oersted field of the current up to a maximum field inhomogeneity of about $\pm 200\,\mathrm{Oe}$.

The idea of the experiment is further illustrated in Fig. 2. As mentioned above, the frequency of the MSBVW spin wave decreases with increasing wavevector and the allowed states are situated below the zero-wavevector gap Δ_0. Thus, to realize a scenario of spin wave reflection at a field inhomogeneity, one should not increase, but decrease the field (gap). The inset of Fig. 2 illustrates

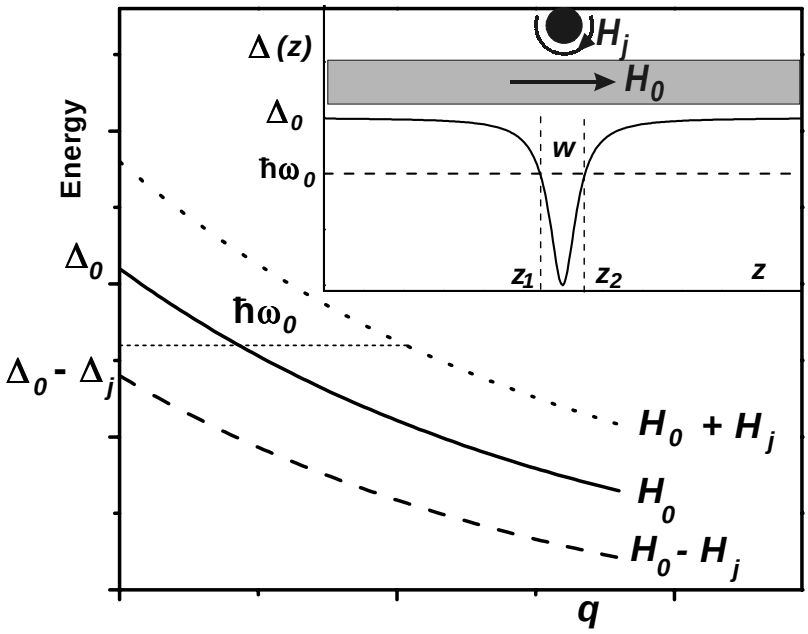

Fig. 2: Schematic spectrum of MSBVW spin waves in a magnetic film. $\Delta(z)$ is the gap of the spectrum. The inset illustrates the profile of the gap, the locations z_1 and z_2 of the turning points and the forbidden interval of width w due to the inhomogeneous field caused by the dc-conductor.

the geometry of the field, the profile of the gap, and the creation of the turning points z_1 and z_2. The turning points are determined be the condition $\hbar\omega = \Delta(H(z) = H_0 - H_j(z))$. As it is seen from the inset of Fig. 2, this equation has two solutions, z_1 and z_2, and the interval between the turning points is a forbidden region with no spin-wave state with ω. The width of the interval $w = z_2 - z_1$ will be considered as the barrier width for spin wave tunneling. On the other hand, an enhanced magnetic field does not essentially disturb the propagation: spin waves propagate through the inhomogeneity by increasing the wavevector according to the local field.

Measurements of the propagation of spin-wave packets through the field inhomogeneity using the space and time resolved Brillouin light scattering technique are displayed in Fig. 3. Two sequences of snapshots are shown for different delay times. Figure 3a corresponds to an enhancement of the local field by the dc-current, whereas the images shown in Fig. 3b were obtained at reduced local field. Each snapshot displays the distribution of the spin-wave intensity over the film normalized to its maximum.

Figure 3a demonstrates no essential reflection of the spin waves. As it is discussed above, a region with a slightly enhanced local field cannot contain a turning point for a MSBVW spin-wave packet. The wave accommodates its wavevector according to the dispersion law and passes almost unaffected through the region of field inhomogeneity. An observed weak reflection is due to the non-adiabatical nature of the process: In fact, the above discussion implies that the wavelength of the wave is much smaller than the lateral scale of the field inhomogeneity. In the experiment, however, these two values are of the same order of magnitude.

A much more interesting effect is illustrated in Fig. 3b corresponding to a reduced local field. One can easily see that the region of the reduced field inhibits propagation of spin waves. Due to local field reduction the region of the inhomogeneous field serves as a forbidden region or a barrier for the wave and reflects it. However, the spin-wave packet is partially reflected and partially transmitted by the barrier. The transmission and reflection probabilities depend on the barrier width and height and the wavevector of the wave. Indeed, this effect is reminiscent to the quasi-classical quantum mechanical problem of particle reflection and tunneling.

To understand the physics of the observed spin wave tunneling the transmission coefficient, defined

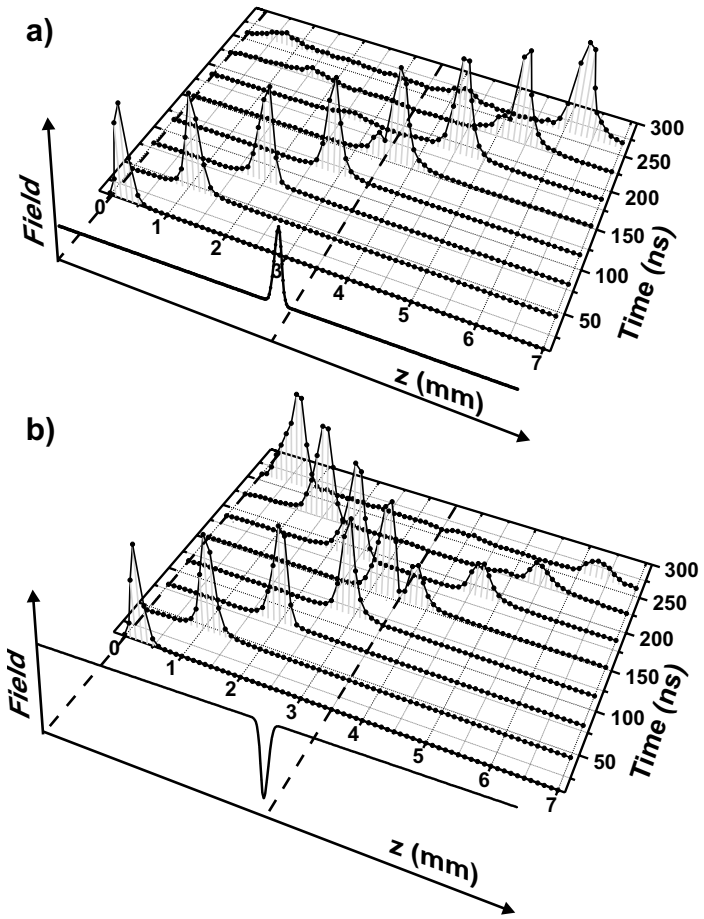

Fig. 3: Propagation of a MS-BVW spin-wave packet across a YIG film with local field inhomogeneity, observed by space- and time-resolved BLS. Snapshots of the spin-wave intensity at given delay times are shown. a) field/gap has a local maximum, creating a potential dip for the wave; b) field/gap has a local minimum, creating a potential barrier for the wave. The field profiles are displayed in the bottom of each panel. The maximum absolute value of H_j is the same for the both panels and is about 56 Oe.

for the intensity of the wave, T, was measured as a function of the dc-current. In agreement with the above consideration T is close to unity until the dc-current reaches a given value, j_c, which corresponds to the creation of a turning point just below the dc-conductor. Fig. 4a presents the normalized barrier transmission coefficient, $T_b = T(j)/T(j_c)$. As it is seen in the inset of Fig. 2, by increasing the value of the dc-current the turning points can be moved away from each other. The profile of the inhomogeneous field, the positions of the turning points and, accordingly, the width of the barrier, w, can be easily calculated for a given j for the experimental geometry. For the sake of clarity T_b is shown as a function of w. With increasing w the transmission coefficient decreases. From a comparison of the measured dependency $T_b(w)$ with the predictions of different theoretical models the origin of the spin wave tunneling will be clarified.

Despite the obvious similarity with the quantum mechanic problem, the physics of the spin wave tunneling is more complicated since the long-range magnetic dipole interaction important for magnetic systems must be taken into account. To begin with, let us first follow a simple approach neglecting the dipole interaction [10]. In this case the Landau-Lifshitz equation for a sinusoidal excitation $m \propto \exp(i\omega t)$ can be rewritten in the form of the Schrödinger equation, Eq. (1). If $H(z)$ is a slow function of z, the solution of Eq. (1) can be written as as a wave $m \propto \exp(iqz)$ with a z-dependent wavevector obeying:

$$q^2(z) = (\omega/\gamma - H(z))/D \quad , \tag{4}$$

where $D = 2A/M_S$ is the exchange stiffness constant ($D = 5 \cdot 10^{-9}\,\mathrm{Oe\,cm^2}$ for YIG). Thus, the solution of Eq. (1), $m(z)$, is either a sinusoidal ($H < \omega/\gamma$, outside the barrier) or an exponential

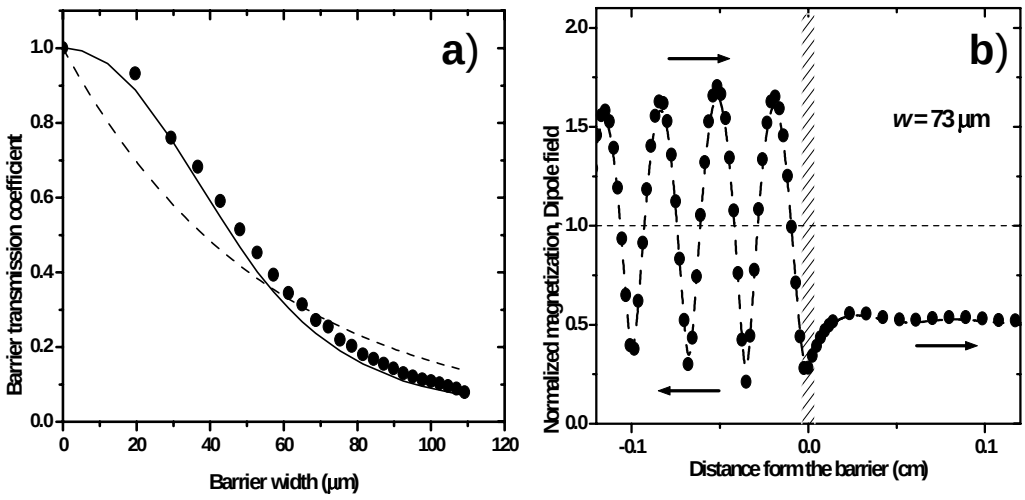

Fig. 4: a) Barrier transmission coefficient as a function of the barrier width. Full circles: experimental values. Dash line: results of the analytical approach, neglecting the magnetic dipole interaction. Solid line: results of the numerical simulations. b) Profiles of the dynamic magnetization (full circles) and dipole field in the wave. Incident, reflected, and tunneling waves are considered. The barrier is indicated by the hatched area. The horizontal dotted line corresponds to the value of the magnetization amplitude without the barrier.

($H > \omega/\gamma$, inside the barrier) function of z. As it is seen from the above analysis, the possibility to penetrate into forbidden regions and tunnel through them is an intrinsic property of spin waves even for the simplest model. However, this approach cannot explain the described experimental observations. First of all, the predicted dependence of $T_b(w)$ is exponential: $T_b(w) = \exp(-2|\int_{z1}^{z1+w} q(z)dz)|)$. The dashed line in Fig. 4 is calculated based on the above expression. It is clear that the prediction of this model disagrees with the experiment. Moreover, as follows from Eqs. (1) and (4), the field must be *increased* to create a strongly reflective barrier. This is in obvious contradiction with the experiment (see Fig. 3).

Next we consider a more realistic approach. It is known [11] that not the exchange, but the magnetic dipole interaction dominantly determines the properties of spin waves with $q \approx 10^2 - 10^3\,\mathrm{cm}^{-1}$ in YIG films. Therefore, this interaction has to be taken into account in our analysis. Unfortunately, due to the non-local origin of the interaction the analytical analysis is very complex. Instead, a numerical approach has been used. The stationary case was considered and the Landau-Lifshitz equation has been rewritten as a vector integral equation, which then has been solved using the iterational convergence method. For excitations with a time dependence $\propto \exp i\omega t$ the equation for $m_x(z)$ yields:

$$m_x(z) = \chi(z) \times \left[\int_{-\infty}^{\infty} G_{xx}(z,z') m_x(z') dz' + h_x^s(z) \right] \tag{5}$$

where $\chi(z) = 4\pi M_S H(z)/(H^2(z) - (\omega/\gamma)^2)$ is the diagonal term of the complex magnetic susceptibility of the medium taking into account the field non-uniformity. $G_{xx}(z,z')$ is a component of the magnetostatic Green function in its real space presentation [12], and $h^s(z)$ is the magnetic microwave field of the antenna. Wave damping was taken into account in an usual way [11], i.e., by adding an imaginary part to the static magnetic field: $H(z) \to H(z) + i\Delta H$, where ΔH is the linewidth of ferromagnetic resonance of the film. In zero approximation the analytical solution of Eq. (5) for spatially homogeneous static magnetic field $H(z) = H_0$ is used:

$$m_x(z) = \int_{-\infty}^{\infty} \frac{(\chi_0' - i\chi_0'')\exp(ikz)\langle h_x^s\rangle_k}{[1-\chi_0'(P(k)-1)] + i\chi_0''(P(k)-1)} dk \quad , \tag{6}$$

where $\langle h_x^s\rangle_k$ is the spatial Fourier component of $h^s(z)$, $\chi_0 = \chi$ for $H(z) = H_0$, and $P(k)$ is the dipole matrix element calculated in [13]. A numerical algorithm providing fast convergence of the iterational equation Eq. (5) with the start function Eq. (6) has been constructed. The Fast Fourier Transform algorithm for discrete values of z and k was used followed by the Runge-Kutta technique to solve the resulting system of differential equations. The numerically obtained dependence of $T_b(w)$ is shown in Fig. 4a by the solid line. The quantitative agreement between the theory and the experiment is striking, especially if one takes into account that no fitting parameter was used in the simulations. Thus, one can conclude that the observed effect is tunneling of dipolar spin waves through the field inhomogeneity. It is important to mention that not only the dipole field, but the dynamic magnetization as well tunnels through the barrier. This is illustrated by Fig. 4b, where the calculated profiles of the dynamic magnetization and that of the dipole field are presented. A standing wave on the left side of the barrier is due to interference between the incident and reflected waves. It is in fact observed in the experiment if longer spin wave pulses, as shown in Fig. 3, are used. But what is more important, the relation between the dynamic magnetization (full circles) and the dipole field (dashed line) is almost the same outside as well as inside the barrier. Thus, Fig. 4b clearly demonstrates that the observed tunneling effect is tunneling of the dynamic magnetization.

Support by the Deutsche Forschungsgemeinschaft is gratefully acknowledged. The work is supported in part by the European Communities Human Potential programme under contract number HRPN-CT-2002-00318 ULTRASWITCH.

References

[1] E. Schlömann, Spin-Wave Spectroscopy, in: *Advances in Quantum Electronics*, Ed. J.R. Singer (Columbia University Press, New York, 1961).
[2] J.R. Eshbach, Phys. Rev. Lett. **8**, 357 (1962).
[3] J.R. Eshbach, J. Appl. Phys. **34**, 1298 (1963).
[4] E. Schlömann, J. Appl. Phys. **35**, 159 (1964).
[5] J. Jorzick, S.O. Demokritov, B. Hillebrands, M. Bailleul, C. Fermon, K.Y. Guslienko, A.N. Slavin, D.V. Berkov, N.L. Gorn, Phys. Rev. Lett. **88**, 047204-1 (2002).
[6] J.P. Park, P. Earnes, D.M. Engebretson, J. Berezovsky, P.A. Crowell, Phys. Rev. Lett. **89**, 277201-1 (2002).
[7] C. Bayer, S.O. Demokritov, B. Hillebrands, A.N. Slavin, Appl. Phys. Lett. **82**, 607 2003.
[8] S.O. Demokritov, B. Hillebrands, A.N. Slavin, Phys. Rep. **348**, 441 (2001).
[9] R.W. Damon, J.R. Eshbach, J. Phys. Chem. Solids **19**, 308 (1961).
[10] E. Schlömann, R.I. Joseph, J. Appl. Phys. **35**, 167 (1964).
[11] A.G. Gurevich, G.A. Melkov, *Magnetization Oscillations and Waves* (CRC Press, New York, 1996).
[12] K.Y. Guslienko, S.O. Demokritov, B. Hillebrands, A.N. Slavin, Phys. Rev. B **66**, 132402 (2002).
[13] B.A. Kalinikos, A. Slavin, J. Phys. C.: Solid State Phys. **19**, 7013 (1986).

6.2 Brillouin light scattering measurements of single micrometer sized magnetic elements

V.E. Demidov, S.O. Demokritov, and B. Hillebrands[1]

Brillouin light scattering (BLS) spectroscopy is well known as a powerful and flexible tool for the investigation of dynamic magnetization processes, for a recent review see [1]. Among the main advantages of this technique the wide dynamic range and the potential to realize local measurements of the amplitude of the dynamic magnetization are of importance. The BLS technique is especially useful when investigations of dynamic magnetic properties of micrometer sized magnetic elements are concerned. Recently, BLS spectroscopy has been successfully employed for studies of arrays of micrometer sized magnetic wires and dots, see, e.g., [2, 3] and the references therein. However, in a standard BLS experiment the diameter of the laser spot, which is used for probing the dynamic magnetization, is much larger than the typical size of a magnetic element to be studied. As a result, usual BLS measurements always demand large arrays of absolutely identical elements and cannot be used for the investigation of a single one.

The purpose of this work is to elaborate a novel BLS setup with a probing laser spot in the submicrometer range, and to test this setup by measuring the dynamic magnetization in a single micrometer sized magnetic element.

The layout of the micro-BLS setup is shown in Fig. 1. An argon ion laser produces a vertically polarized probing beam with a diameter of 2 mm. In order to reduce the divergence of the beam the latter is expanded by a factor of ten by means of a beam expander and confined in diameter by a diaphragm with an aperture of 3 mm. The resulting beam is transmitted through a thin-film polarizer increasing the polarization degree of the beam up to 10^4. Then the beam is reflected by a polarizing beamsplitter and focused by a microscope objective on the surface of the magnetic sample placed into a magnetic field applied parallel to its plane. The angle between the plane of

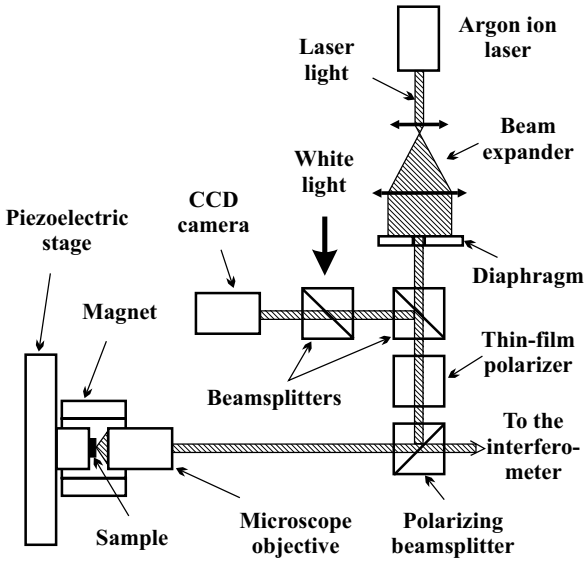

Fig. 1: Layout of the micro-BLS setup.

[1] In collaboration with M. Laufenberg and P.P. Freitas, INESC Microsistemas e Nanotecnologias, Lisboa, Portugal.

the sample and the axis of the objective is equal to 90°. The objective is characterized by the magnification of 100×, the working distance of 4 mm, and the numerical aperture of 0.75. The objective allows a focusing of the beam down to about 500 nm. In order to position the laser spot to the desired place on the sample, the latter is mounted on a piezoelectric stage, which allows positioning in two directions with a precision of about 50 nm. The total scanning range of the stage amounts to a value of 100 µm. At the surface of the magnetic sample the light is inelastically scattered by spin waves. As a result, the frequency of the scattered light is shifted by the value of the frequency of the spin wave. In addition to that, the plane of polarization of the scattered light is rotated by 90° [4]. The latter allows a partial separation of the weak scattered light from the very intensive light reflected from the surface of the sample. This separation is fulfilled by the above-mentioned polarizing beamsplitter, which transmits the horizontally polarized scattered light and reflects the remaining part of the light back in the direction of the laser. The beamsplitter suppresses the vertically polarized component in the transmitted light by a factor of 10^4, which provides a reasonable signal-to-noise ratio for the following analysis. Finally the scattered light is analyzed by means of a tandem Fabry-Pérot interferometer operating in multipass configuration [5].

In order to find a micrometer sized magnetic element on the surface of a sample, which normally has dimensions of a few millimeters, a viewing system is integrated into the BLS setup. This system consists of a CCD camera supplied with a telescopic objective, two beamsplitters, and a source of white light (see Fig. 1). It uses the reflected light separated from the scattered light by the polarizing beamsplitter. The system allows the direct observation of the surface of the sample and the position of the probing laser spot on the screen of a monitor during measurements.

The BLS technique is known for its selectivity with respect to the wavevector of a spin wave [4]. For the case of scattering from non-confined media this selectivity is usually determined by an aperture of the objective collecting the scattered light. For the case of a confined medium such as a small magnetic element and/or the case of a finite size of the probing laser spot, the selectivity is drastically affected by the uncertainty in the wavevector of the scattered light caused by the spatial confinement. As far as in the micro-BLS setup the spot size $w = 500\,\text{nm}$ is very small, the uncertainty in the wavevector of the scattered light is rather large and is of the value of $\Delta k = 2\pi/w = 1.26 \cdot 10^5\,\text{cm}^{-1}$. Taking into account the value of the numerical aperture of the objective, $NA = 0.75$, and the wavelength of the incident light, $\lambda = 514\,\text{nm}$, one can easily calculate the largest wavenumber k_{max} of spin waves that can be detected by our setup. This value was found to be equal to about $4.9 \cdot 10^5\,\text{cm}^{-1}$. This indicates that keeping the axis of the objective at 90° to the plane of the sample we simultaneously collect a signal from spin waves having wavenumbers of up to $4.9 \cdot 10^5\,\text{cm}^{-1}$. However, starting from a certain wavenumber $k_c < k_{max}$ the light scattered by spin waves starts partially to leave the cone of rays passing the objective and the signal becomes significantly smaller. For our case k_c is equal to about $5 \cdot 10^4\,\text{cm}^{-1}$.

The micro-BLS setup was tested using samples having a geometry, which is typical for integrated magnetic memory circuits. Each sample contains 16 magnetic elements with dimensions of $a \cdot b = 1.3 \cdot 2.3\,\mu\text{m}^2$. A schematic view of a magnetic element is shown in the inset to Fig. 2. The elements consist of two magnetic layers, separated by a 4 nm thick Cu spacer. The bottom magnetic layer is a 10 nm thick CoFe film, whereas the top one is 5 nm thick NiFe film. The elements are placed at the top of a 40 µm wide and 60 nm thick Al stripe, which plays the role of the bottom electrode. The 60 nm thick upper electrode has the shape of a narrow stripe crossing the magnetic element along its short side. The width of the upper electrode is chosen to be 0.4 µm in order to leave a large enough part of the upper magnetic layer accessible for the BLS measurements. During the BLS measurements the laser spot was kept in the middle of the uncovered area of the upper magnetic

layer. The external magnetic field of strength H was applied along the long side of the magnetic element.

Figure 2 shows a typical spectrum of thermal spin waves accumulated during 30 minutes (thick solid line). As seen from Fig. 2, the signal from thermal waves is rather weak but, nevertheless, it can be clearly seen above the level of noise. The small measured intensity of the scattered light originates from the very small power of the probing laser light, which can be focused to 500 nm diameter on the surface of the sample without danger to overheat the latter. For different samples the maximum power level depends on the thermal conductivity of the substrate. For the samples investigated here this value was found to be equal to 2 mW.

As seen from Fig. 2, despite the small dimensions of the magnetic element, the spectrum of thermal waves does not demonstrate clear resonant peaks and appears as a continuous one. In order to understand this fact the theoretical resonant spectrum was calculated for the element using the dispersion law for spin waves propagating arbitrarily to the direction of magnetization in tangentially magnetized ferromagnetic films [6]. The resonant frequencies were found neglecting the non-uniformity of the internal magnetic field. The quantization of the in-plane wavevector k of spin waves was calculated using the magnetic wall boundary conditions for dynamic magnetization at the edges of the element: $k^2 = (n\pi/a)^2 + (m\pi/b)^2$, where $n, m = 1, 2...$ The frequencies of the 16 lowest-order resonances are shown in Fig. 2 by the vertical solid lines. These resonances are divided into four sets s1-s4. The different sets are characterized by different values of n, whereas the resonances within each set are characterized by different values of m. The resonances shown by the strongest lines correspond to $m = 1$. With the increase of m the strength of the corresponding lines decreases. The resonant spectrum was calculated for the strength of an internal magnetic field $H_i = 385$ Oe, which was used as an adjustable parameter in order to fit the theoretical spectrum to the experimental one. The indicated value of H_i corresponds to the frequency of the uniform ferromagnetic resonance in a tangentially magnetized ferromagnetic film f_P equal to 5.66 GHz. This frequency is indicated in Fig. 2 by a vertical dashed line.

The calculations show that the values of the wavenumbers corresponding to the shown resonant frequencies lie in the range from $2.7 \cdot 10^4$ to $1.1 \cdot 10^5$ cm^{-1}. As far as these values are smaller than k_{max} all the corresponding resonant peaks must be seen in the spectrum. However, every resonant peak has a finite width, which is determined by the intrinsic magnetic losses in the magnetic material. For NiFe this width is larger than 170 MHz. As seen from Fig. 2, this width significantly exceeds the frequency separation between the peaks. As a result, the individual peaks merge one

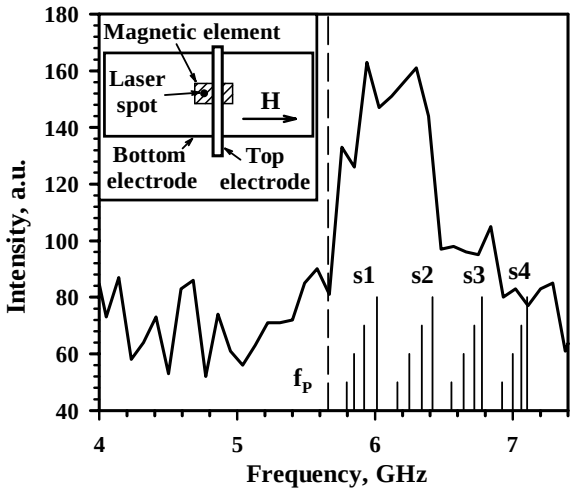

Fig. 2: Measured spectrum of thermal spin waves in the magnetic element (thick solid line) and the calculated resonance spectrum for the same element (thin vertical solid lines). Inset: Schematic view of the single, micrometer sized magnetic element.

with another and the spectrum turns out to be continuous.

It is important to note here that the thermal spectrum shown in Fig. 2 demonstrates approximately the same intensity for the first two sets of resonances, whereas the third and the fourth sets have significantly smaller intensities decreasing stepwise from one set to another. This fact confirms the above-made conclusion concerning the value of $k_c = 5 \cdot 10^4\,\mathrm{cm}^{-1}$. The first and the second sets of resonances are characterized by the wavenumber of the lowest-order resonance equal to $2.8 \cdot 10^4\,\mathrm{cm}^{-1}$ and $5.0 \cdot 10^4\,\mathrm{cm}^{-1}$, respectively. For the third and the fourth sets these values are $7.4 \cdot 10^4\,\mathrm{cm}^{-1}$ and $9.8 \cdot 10^4\,\mathrm{cm}^{-1}$. Consequently, all the light scattered by spin waves of the first two sets is collected by the objective, whereas a significant part of the light scattered by spin waves of the third and the fourth set is lost.

In conclusion, we have elaborated the micro-BLS setup allowing measurements of single micrometer sized magnetic elements. The size of the laser spot, which plays the role of a probe in the BLS measurements, was reduced down to 500 nm. Despite the serious reduction of the probing light power, a spectrum of thermal spin waves can easily be measured by means of the elaborated setup in reasonable time. It is found that the reduction of the probing spot leads to the loss of the resolution on wavenumber of spin waves. This fact limits one in the use of the micro-BLS technique for measurements of resonant spectra of spin waves in small magnetic elements. Nevertheless, this disadvantage does not hamper the use of the micro-BLS technique for a local probing of amplitudes of excited spin waves on the sub-micrometer scale like it was previously realized on the sub-millimeter scale.

This work was supported in part by the priority programme SPP1133 “Ultrafast magnetization phenomena” of the Deutsche Forschungsgemeinschaft, by the European Community under contract IST-2001-37334 “Low Power Magnetic Random Access Memory with Optimised Writing Time” (NEXT), and by the European Communities Human Potential programme under contract number HRPN-CT-2002-00318 ULTRASWITCH. Young Researcher M. Laufenberg acknowledges the financial support from the European Communities Human Potential Programme.

References

[1] S.O. Demokritov, B. Hillebrands, A.N. Slavin, Phys. Rep. **348**, 441 (2001).
[2] S.O. Demokritov, B. Hillebrands, A.N. Slavin, IEEE Trans. Magn. **38**, 2502 (2002).
[3] Y. Roussigne, S.M. Cherif, C. Dugautier, P. Moch, Phys. Rev. B **63**, 134429/1 (2001).
[4] M.G. Cottam, D.J. Lockwood, *Light scattering in magnetic solids*, Wiley, New York (1986).
[5] B. Hillebrands, Rev. Sci. Instr. **70**, 1589 (1999).
[6] M.J. Hurben, C.E. Patton, J Magn. Magn. Mater. **139**, 263 (1995).

6.3 Observation of collective spin-wave modes in an inhomogeneously magnetized stripe

C. Bayer and B. Hillebrands[1]

Soft magnetic materials such as permalloy often have a very simple magnetic microstructure which is not single domain. It is physically interesting to ask whether such systems have collective excitations, i.e. spin-wave modes. We have studied the dynamic properties of inhomogeneously magnetized 18 nm thick and 2.3 µm wide permalloy stripes using time-resolved Kerr microscopy [1]. If the magnetic field, which is applied along the short axis of the stripe, is close to the shape anisotropy field, we find a new class of modes at *higher* frequencies than that of the ordinary precessional mode at the center of the stripe. Although these modes are detected at the edges of the stripe, they are fundamentally different than the localized edge modes observed previously at higher fields [2–4]. The localized modes are confined in regions of inhomogeneous magnetic field at the edges of the stripe, and their eigenfrequencies are *lower* than the frequency of the center mode. In contrast, we will show that the new modes, which we call "cross-over" modes, span the entire stripe, but are, with the experimental setup used here, only detectable at the edges, where the magnetization rotates by 90 degrees. The width of the edge regions determines the effective wavevector near the edges of the stripe.

The detailed experimental procedure is described elsewhere [3, 5]. Here the applied field H_a was oriented along the width of the stripe while the Gaussian field pulse H_{pulse} with an amplitude of $\approx$5 Oe and a temporal width of 120 – 150 psec was directed along the length of the stripe. Data obtained in a magnetic field H_a = 80 Oe with the objective focused on the center of the stripe are shown in Fig. 1(a). The response observed corresponds to a nearly uniform precession of the magnetization about the effective field at the center of the stripe. As can be seen in the Fourier transform of the data shown in Fig. 1(b), the spectrum in this case is dominated by a single peak. As the observation point is moved away from the center, the spectrum changes as shown in Figs. 1(d) and (f), with additional peaks appearing at higher frequencies. A full spectral image of a scan

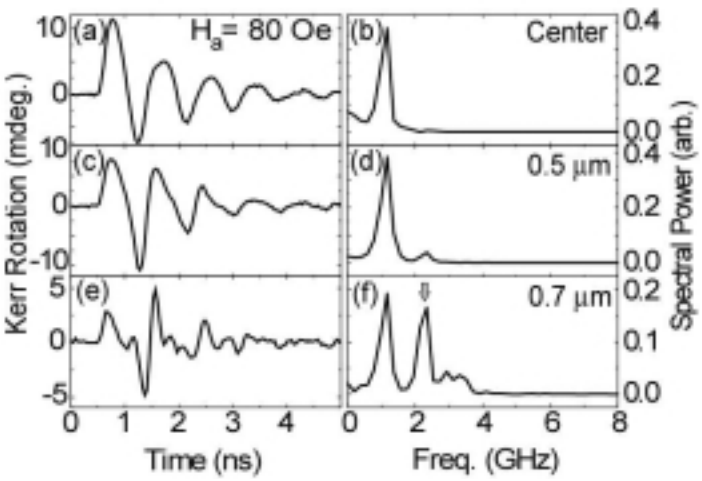

Fig. 1: Time and frequency response measured at different positions relative to the center of the stripe.

[1]The experimental part of his work was done at the School of Physics and Astronomy, University of Minnesota in collaboration with J.P. Park, H. Wang, M. Yan, C.E. Campbell, and P.A. Crowell, School of Physics and Astronomy, University of Minnesota, Minneapolis, Minnesota 55455, USA.

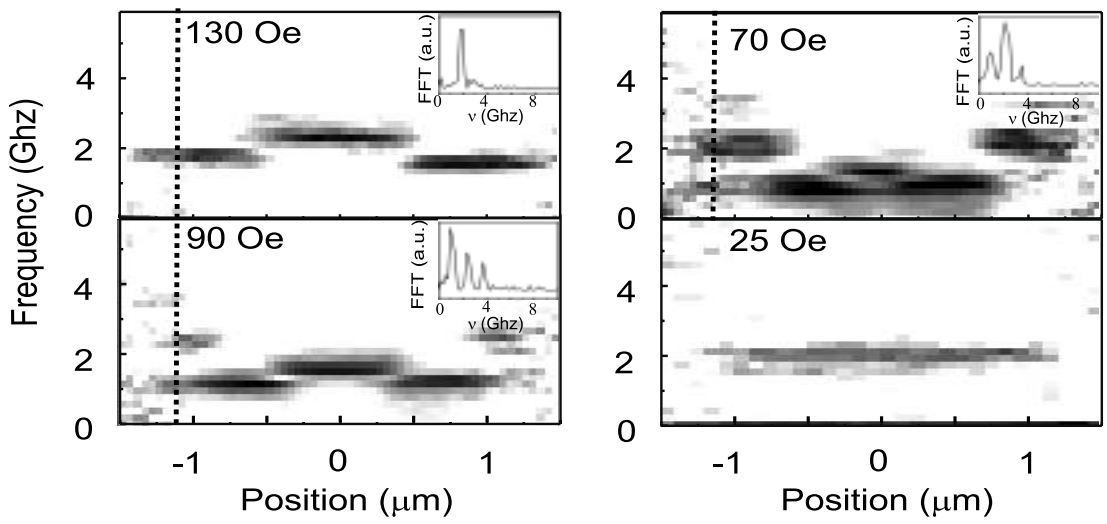

Fig. 2: Spectral images of cross section of a stripe in different applied fields. The insets show the spectra at the position indicated by the dotted line. Note that the width of the images is larger than the physical width of the stripe due to the diameter of the optical spot ($\approx$ 800nm).

across the stripe can be constructed by measuring the spectrum at each position and converting the spectral intensity to a gray-scale. The results for several fields from 25 Oe to 130 Oe are shown in Fig. 2. The spectral intensity has been normalized by the integrated power measured at each position. This procedure emphasizes the modes near the edges of the stripe, which are much weaker than the center mode in absolute intensity. The spectra at low and high fields are well understood. At 25 Oe, the magnetization is nearly parallel to the long axis of the stripe, and the observed response is a single precessing mode. At high fields (> 130 Oe), the response consists of a precessional mode spanning most of the stripe and a lower frequency mode localized at each edge [2–4]. As discussed previously, the high-field mode structure can be understood in a model in which the internal field is non-uniform but the magnetization is essentially uniform. Here we focus on the field range of $60-130$ Oe, in which clear modes are observed near the edges but at higher frequencies than the center mode. This separate set of modes can be seen in Fig. 2 at 70 Oe and 90 Oe. The insets of the top three panels of Fig. 2 show spectra obtained with the objective positioned 1.2 μm from the center of the stripe, corresponding to the position indicated by the dotted line.

All of the mode frequencies observed at different positions on the stripe are shown in Fig. 3(a) as a function of the applied magnetic field. The frequencies shown are those of peaks with an amplitude at least 5 times the background noise level. The solid curve is the frequency of the ordinary FMR mode of the stripe, which was calculated under the assumption that the magnetization is uniform and that it undergoes coherent rotation. The shape anisotropy energy was determined by approximating the stripe as an ellipsoid with demagnetizing factors: $N_x = H_d/M_s$, $N_y = 0$, and $N_z = 4\pi - H_d/M_s$, where the demagnetizing field H_d =60 Oe was taken from the location of the experimental minimum in the FMR frequency. The points along the dashed curve at high fields are the localized modes discussed above. The points at higher frequencies from $60-120$ Oe are due to the cross-over modes that appear near the edges of the stripe in Fig. 2.

The key observation about the field regime, in which the additional edge modes are observed in Fig. 2, is that, unlike at higher fields (> 130 Oe), the magnetization of the stripe is strongly nonuniform. The local magnetization direction is determined by a competition between the shape

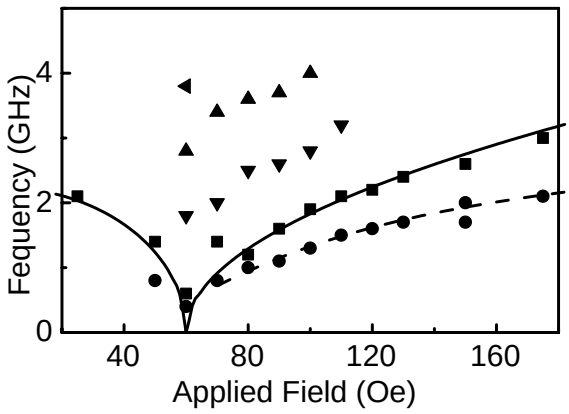

Fig. 3: Measured frequencies as a function of the applied field. The solid curve is the frequency of the ordinary FMR mode calculated as described in the text. The points along the dashed curve are the localized modes.

anisotropy field, which favors a magnetization parallel to the edges of the stripe, and the applied field. Fig. 4(a) shows the two components of the magnetization of a 2.3 µm wide stripe calculated micromagnetically for an applied field of 90 Oe. The magnetization at the center is aligned parallel to the applied field while it is nearly parallel to the stripe at the edges. Between these two extremes the magnetization rotates smoothly over a length of 0.5 µm. Fig. 4(b) shows the corresponding effective field H_{eff}, including the applied, demagnetizing, and exchange fields. H_{eff} is non-zero only in the region where the magnetization is parallel to the applied field.

In addition to the experiment, simulations of the full Landau-Lifshitz-Gilbert equation were conducted using the object-oriented micromagnetic framework (OOMMF) [6] using a realistic pulse profile. The results of the simulations are compared with the experiment in Fig. 5 at fields of 90 and 125 Oe. Panels (a) and (c) show experimental spectral images. Panels (b) and (d) show spectral images obtained from the time-domain simulations, which were processed in the same manner as the experimental data. The simulations show some of the important qualitative features of the experiment, but there are several discrepancies, the most important one is the apparent shift in field scale. The mode structure near the edges of the stripe is qualitatively similar in both cases, with the weight moving closer to the edges with higher mode index as noted above. The structure in the center of the stripe seen in the simulations cannot be observed in the experiment. As the nodes of the dynamic magnetization are closer together in the center of the stripe than at the edges the

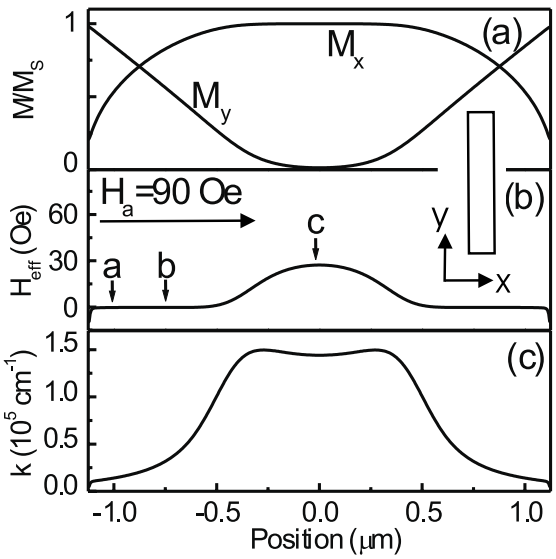

Fig. 4: (a) The two components of the static equilibrium magnetization are shown as a function of the position x in an applied field of 90 Oe. (b) The corresponding effective field H_{eff}. (c) The wavevector, evaluated from the dispersion relation as described in the text, is shown as a function of position. The inset shows the coordinate system.

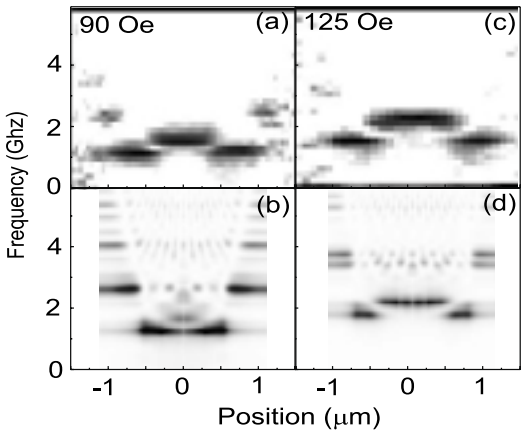

Fig. 5: The upper panels (a) and (c) show experimental spectral images of the cross-section of the stripe at fields of 90 and 125 Oe. The lower panels (b) and (d) show simulated images obtained as described in the text. The spectra are normalized by the integrated power at each position.

effective wavevector of the spin wave must be smaller there. As the diameter of the optical spot ($\approx$800 nm) used in the experiment is larger than the effective wave length in the center of the stripe the Kerr signal averages out. For higher modes, the distance from the edge of the stripe to the first internal node decreases, which is why the spectral weight observed in the experiment moves further towards the edges of the stripe as the frequency increases.

A detailed picture of the features of spin wave in the region of inhomogeneous magnetization can be obtained by considering the dispersion relation at each position in the stripe. This is the same philosophy applied in the WKB argument used previously to described localized spin-waves [2, 3], except that in the current case both the internal field and the dipole-dipole matrix element vary with position. The dynamic torque in our experiment couples only to wavevectors along the short axis of the stripe. For a given orientation of **M**, the dispersion relation for spin-waves propagating along the short axis can be calculated following Kalinikos and Slavin [7]. The dispersion relation at three positions across the stripe in a field of 90 Oe is shown in Fig. 6. These positions are also indicated by the labels *a*, *b*, and *c* in Fig. 4.

At the edge of the stripe, the magnetization is nearly perpendicular to the wavevector **k**, and the corresponding dispersion relation, indicated (a) in Fig. 6, is that of the usual Damon-Eshbach modes. In the center of the stripe, $\mathbf{M}||\mathbf{k}$, and the dispersion relation (c) is that of the magnetostatic backward volume wave (MSBVW) modes [7]. The frequencies of the three lowest modes found in simulations are shown as the dashed lines in Fig. 6. Near the edge of the stripe there is a minimum wavevector determined by the intercept of the dashed curve with the Damon-Eshbach dispersion relation (a). The wavevector determined as a function of position over the entire width of the stripe is shown for the first cross-over mode in Fig. 4(c), in which the wavevector at the center of the stripe is about 10 times larger than at the edge. The cross-over modes are thus characterized by two different regimes: a dipolar region near the edge of the stripe and an exchange-dominated regime of large wavevector near the center of the stripe. In contrast to the two higher modes, the lowest frequency mode does not intercept the dispersion relation (c) at the center of the stripe. This is a signature of the incipient spin-wave localization and becomes more pronounced as the MSBVW dispersion relation at the center of the stripe shifts upward with increasing applied field. Unlike the cross-over modes, the localized modes do not propagate in the center of the stripe. This is the important distinction between the two types of modes, even though they are both observed at the edges.

As in the spin-wave localization problem, it is not obvious *a priori* that the usual adiabatic condition for a WKB theory is satisfied [8]. In the edge regions, the dispersion relation changes on a scale

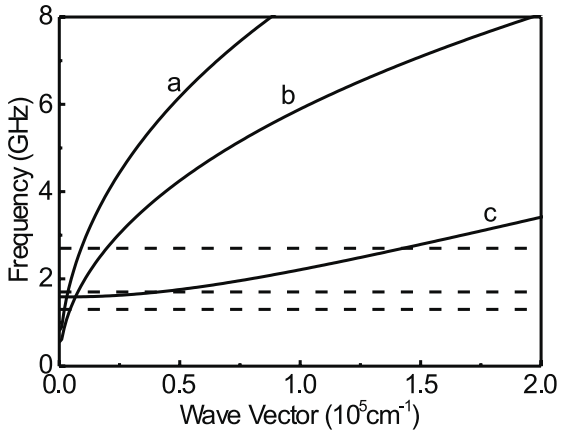

Fig. 6: The dispersion relation calculated at three points along a cross-section of the stripe of width 2.3 µm in an applied field of 90 Oe. *a*, *b*, and *c* indicate positions 1.0, 0.75, and 0 µm from the center of the stripe. The three dashed lines indicate the frequencies of the lowest modes found in simulations.

comparable to the wavelength, and the boundary conditions are not known exactly. Nonetheless, for a given frequency it is straightforward to calculate the wavevector of each mode as a function of position using the magnetization profile shown in Fig. 4. The Bohr-Sommerfeld integral

$$\phi(n) = \int_{-w/2}^{w/2} k_n(x)dx, \tag{1}$$

can then be calculated, where w is the width of the stripe and n is the number of nodes. We have calculated ϕ for the modes at 90 Oe with 2 - 16 nodes, finding $\phi(n) = \phi_0 + n\pi$, with $\phi_0 = (0.83 \pm 0.02)\pi$. The phase difference $\phi(n) - \phi(n-1)$ differs from π by at most 5%. The relative success of the WKB approach for the cross-over modes suggests that it is meaningful to think of a local dispersion relation, even in cases of a strongly inhomogeneous magnetization.

A full report has been submitted to Physical Review B [1].

C.B. acknowledges support by the University of Minnesota MRSEC NSF (DMR 0212032) during his stay in Minneapolis and by the Studienstiftung des deutschen Volkes. This work was also supported by NSF DMR-9983777.

References

[1] C. Bayer, J.P. Park, H. Wang, M. Yan, C.E. Campbell, P.A. Crowell, submitted to Phys. Rev. B.
[2] J. Jorzick, S.O. Demokritov, B. Hillebrands, D. Berkov, N.L. Gorn, K. Guslienko, A.N. Slavin, Phys. Rev. Lett. **88**, 047204 (2002).
[3] J.P. Park, P. Eames, D.M. Engebretson, J. Berezovsky, P.A. Crowell, Phys. Rev. Lett. **89**, 277201 (2002).
[4] C. Bayer, S.O. Demokritov, B. Hillebrands, A.N. Slavin, Appl. Phys. Lett. **82**, 607 (2003).
[5] J.P. Park, P. Eames, D.M. Engebretson, J. Berezovsky, P.A. Crowell, Phys. Rev. B **67**, 020403R (2003).
[6] M.J. Donahue, D.G. Porter, *OOMMF Users Guide, Version 1.0*, in Interagency Report No. NISTIR 6376, National Institute of Standards and Technology, Gaithersburg, Maryland, 1999.
[7] B.A. Kalinikos, A.N. Slavin, J. Phys. C **19**, 7013 (1986).
[8] L.D. Landau, E.M. Lifshitz *Quantum Mechanics: Non-Relativistic Theory*, 3rd ed. (Pergamon, Oxford, 1977).

B. Nonlinear Wave Effects

6.4 Experimental observation of symmetry-breaking nonlinear modes in an active ring

S.O. Demokritov, A.A. Serga, V.E. Demidov, and B. Hillebrands[1]

Solitons are large-amplitude, spatially confined wave packets in nonlinear media. They occur in a wide range of physical systems, such as water surfaces, optical fibres, plasmas, Bose-Einstein condensates and magnetically ordered media [1, 2]. A distinguishing feature of soliton behavior, that is common to all systems, is that they propagate without a change in shape owing to the stabilizing effect of the particular nonlinearity involved [1,3]. When the propagation path is closed, modes consisting of one or several solitons may rotate around the ring, the topology of which imposes additional constraints on their allowed frequencies and phases [4, 5]. Here we measure the mode spectrum of spin-wave solitons in a nonlinear active ring constructed from a magnetic ferrite film. Several unusual symmetry-breaking soliton-like modes are found, such as "Möbius" solitons, which break the fundamental symmetry of 2π-periodicity in the phase change acquired per loop: a Möbius soliton needs to travel twice around the ring to meet the initial phase condition.

Despite the numerous publications on nonlinear wave propagation [1–3, 6, 7], multi-soliton modes in confined nonlinear systems have received very little attention to date. Very recently Carr et al. have analyzed multi-soliton modes in a box with infinitely high walls and, equivalently, a ring [4, 5], and they find that the symmetry of these modes can differ from that of linear modes of the system. The linear modes of a box are sinusoidal standing waves enumerated by the number of half-wavelengths that satisfy the box size. There is a direct connection between the mode number of a linear mode and its mirror symmetry with respect to the center of the box: odd and even modes are symmetric and antisymmetric, respectively. It was shown [5] for the case of a so-called

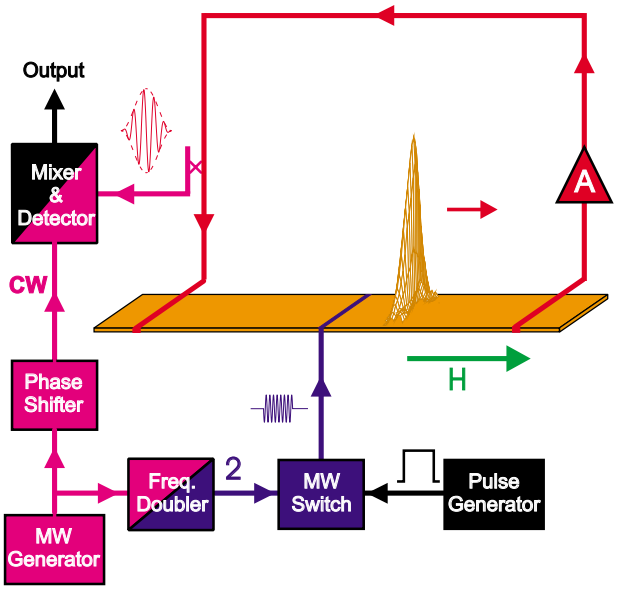

Fig. 1: Schematic layout of the active ring based on an yttrium iron garnet film as the nonlinear medium for spin-wave propagation and the experimental arrangement for observation of nonlinear modes in the ring. The ring consists of the film waveguide, two antennae, and the linear microwave amplifier (A). Nonlinear modes of the ring are filtered using parametric pumping at double frequency at the position of the center antenna as described in the text. The directional coupler, the phase-shifter and the mixer with detector are used for phase sensitive detection of the modes by mixing them with a c.w. reference signal.

[1] In collaboration with M.P. Kostylev and B.A. Kalinikos, St. Petersburg Electrotechnical University, 197376 St. Petersburg, Russia.

attractive nonlinearity necessary for solitons to form that nonlinear modes can be classified by the number of solitons comprising a particular mode. However, there is no general connection between the symmetry properties of a mode and the number of solitons. For example, two modes consisting of two solitons are reported: one mode is antisymmetric and the other is symmetric with respect to the box center. The symmetry of the former mode corresponds to the symmetry of the linear mode with two half-wavelengths, while the latter mode has no linear counterpart and was therefore termed a "symmetry-breaking mode".

As a model system, we constructed an active nonlinear ring based on spin-wave propagation in a magnetic low-loss film with longitudinally applied field. This system exhibits the attractive nonlinearity necessary for soliton formation, and thus the nonlinear eigenmode spectrum consists of sets of soliton-like wavepackets. (We use the term "soliton-like mode" because the excitations found are not true solitons owing to the residual lossy character of the ring outside the location of amplification. The difference between soliton-like modes and true solitons has been discussed extensively, see refs [8, 9] for example.) The solitons are envelope solitons, that is, the envelope function of a wavepacket has a soliton shape.

The experimental arrangement is shown schematically in Fig. 1. We studied spin-wave wavepackets travelling in a single-crystalline (111)-oriented yttrium iron garnet (YIG) film of 7 µm thickness, 1.5 mm width, and 40 mm length, forming a waveguide. Two short-circuited microstrip antennae (length 2.5 mm, width 0.05 mm) for the excitation and detection of spin waves are attached to the film at a distance $l = 8$ mm apart from each other. To compensate for the damping of the waves and to maintain uni-directionality of the ring, a linear electronic amplifier connects the output and input antenna. Its gain is chosen such that the system is below the self-generation threshold for chaotic behavior when the phase-sensitive amplifier discussed below is disabled. An external magnetic field of 1870 Oe is applied along the propagation direction, thus allowing for the propagation of packets of "backward volume" spin waves.

In the linear regime, that is, for low excitation amplitudes, the ring shows a series of resonant eigenmodes with frequencies in the interval $7.25 - 7.30$ GHz, spaced by $\Delta\nu = 3.2$ MHz, and wavevectors $k < 100 - 150\,\mathrm{cm}^{-1}$. The exact frequencies of the modes are determined by the phase-quantization condition over the entire ring: $k \cdot l = 2\pi n$, with integer n. An estimation shows that the phase shift accumulated in the electronic components of the ring is negligibly small. The time for a full circuit around the ring is $T_0 = 310$ ns.

It is necessary to have a selection mechanism to individually address each eigenmode of a nonlinear ring. One widely employed method is the use of a critical threshold mechanism: only the mode with the largest amplification gain is generated, at the expense of all others. This is commonly employed in, for example, a ring laser system. Other reported methods are the use of frequency filters or time gate filters (active mode locking) [10–13]. As a very versatile approach for mode selection, we propose and demonstrate the use of a phase-selective amplifier. This amplifier only allows modes to exist on the active ring, which have a well-defined preset phase at the position of the amplifier in the ring. In conjunction with a simple time-gating filter and phase-sensitive mode detection, this approach provides an elegant way to study the nonlinear eigenmodes in the active ring.

To achieve phase-selective amplification we use the technique of parametric parallel pumping. A sufficiently strong microwave field with frequency 2ν can parametrically amplify a spin-wave packet of frequency ν [14, 15]. The pumping microwave field is sent to a microstrip resonator attached to the film centered between the two antennae as shown in Fig. 1. The width of the resonator, which determines the area of pumping, is $d = 0.05$ mm. Since $k \cdot d \ll 2\pi$, non-adiabatic

pumping is achieved and results in a phase-sensitive amplification coefficient: waves having phases $\pi/4 + n\pi$ with respect to the pumping field are amplified most efficiently (see ref. [16] for details).

To provide a useful definition of the phase of a soliton-like wavepacket, we refer to the case of a one-dimensional spin-wave wavepacket propagating in an unconfined magnetic medium. The dynamic magnetization $m(x,t)$ describing the packet can be written as $m(x,t) = f(x - v_g t)\exp(i\varphi(x,t))$ with $\varphi(x,t) = 2\pi\nu t - kx - \varphi_a(x)$, where f is the envelope function, v_g is the group velocity, ν and k are the carrier frequency and wavevector, respectively, and $\varphi_a(x)$ is an additional phase chirp due to nonlinear effects. It is known [1, 17] that for a soliton, $\varphi_a(x)$ is almost constant across the soliton peak. Therefore, one can characterize a propagating soliton by its phase as a whole, for example, at the maximum point of the envelope function: $\varphi(t) = \varphi(x,t)$ for $x = v_g t$. This phase can be detected by mixing the soliton pulse with a continuous-wave (c.w.) reference signal, as is shown in Fig. 1. Note that as the group velocity of the waves under consideration differs considerably from the phase velocity $v_{ph} = 2\pi\nu/k$ the defined phase φ is time-dependent, that is, it changes constantly while the soliton is propagating.

Without pumping in the parametric amplifier, no nonlinear modes are observed. Pumping is applied as a sequence of microwave pulses with a duration $t = 15 - 35$ ns and period T_p. It was found that stable excitations can be observed if T_p is commensurate with T_0: a deviation of only a few nanoseconds destroys the mode. For brevity, the following representative results are presented and discussed for $T_p = T_0$, $T_0/2$, and $T_0/3$.

We begin with the simplest case of one wavepacket in the loop, that is $T_p = T_0$. Figure 2(left panels) illustrates the waveforms of the detected eigenmodes, with curve (a) showing the waveform of the pumping field as a reference. By sweeping the frequency (or, equivalently, the applied magnetic field) in a narrow interval of 20 MHz (8 Oe), several nonlinear eigenmodes are subsequently observed. Without phase analysis all modes detected at different frequencies are indistinguishable and consist of a series of soliton-like pulses spaced in time by T_0 (curve (b)). The phase detection technique reveals two possible types of one-soliton modes.

First, we find solitons all having the same phase, as displayed in curve (c). We label them "N" for "normal" solitons. Second, we find a second set of modes with the phase difference between two consecutive solitons of π, as displayed in curve (d). These modes need to travel twice about the ring to meet the initial condition. Because of their similarity to the Möbius strip, we label them "M" for "Möbius" mode. The detected waveform of the M-mode can be reversed by changing the c.w. reference phase by π (curve (e)). Both modes are observed alternatively at different carrier frequencies ν_N and ν_M with $\nu_N - \nu_M = 1.6$ MHz, that is, $\Delta\nu/2$.

The physical nature of the N-modes is easily understood: a soliton is propagating about the ring with the closed-loop phase shift of $2\pi n$. This set of modes, each mode characterized by n, is the nonlinear counterpart of linear excitations. The M-mode, however, has no analogue in the linear case: after completing a single loop, the phase accumulation of the soliton is $2\pi(n + 1/2)$, and the soliton needs to travel a second loop to achieve the initial state. We point out that the possible existence of Möbius modes, that is eigenmodes with a phase shift per loop that differs from an integer multiple of 2π, was not considered by Carr et al. [4, 5].

We also find eigenmodes consisting of several soliton-like wave-packets per loop. This happens when the pumping period is smaller than T_0. Figure 2(middle panels) displays the case of $T_p = T_0/2$, that is, a system with two equally spaced wavepackets per loop. In a manner similar to Fig. 2(left panels), the top curve (curve (a)) demonstrates the pumping waveform, while the other curves are the measured waveforms of the different modes detected by phase analysis. The

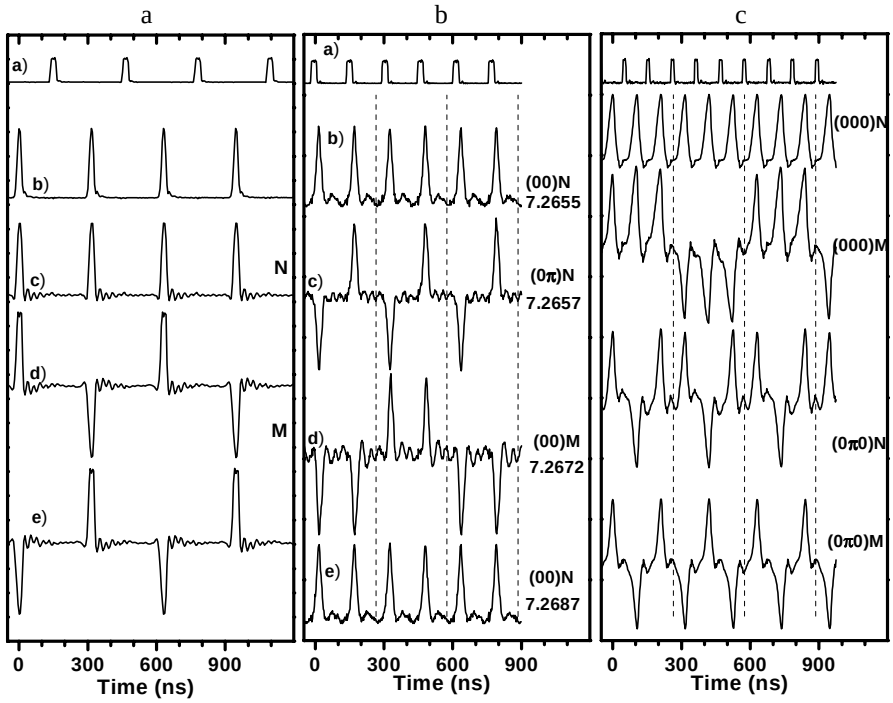

Fig. 2: Waveforms of the modes observed in the ring. Left panels: $T_p = T_0$, one-soliton modes. Curve (a): waveform of the pumping field; curve (b): waveform of a nonlinear mode obtained without phase-sensitive detection; curves (c) and (d): waveforms of two different modes detected using phase-sensitive detection; curve (e): the same as curve (d) with the phase of the c.w. shifted by π. Middle panels: $T_p = T_0/2$, two-soliton modes. Curve (a): waveform of the pumping field; curves (b) - (e): waveforms of different modes with the numbers being the frequency of each mode in units of GHz. Right panels: $T_p = T_0/3$, three-soliton modes; waveforms of the pumping field and of the observed modes. The mode nomenclature is explained in the text.

numbers adjacent to each curve indicate the corresponding values of the mode frequencies in units of GHz. The three vertical dashed lines indicate the time interval T_0 that each of the soliton packets needs to complete the loop.

As for the one-soliton case discussed above, these modes can be divided into normal and Möbius modes. We observe two normal modes (curves (b) and (c)) and one Möbius mode (curve (d)). Although the two normal modes are not completely degenerate, their frequency separation is much smaller than $\Delta\nu$. As found for the one-soliton case, the difference between the Möbius mode and both the normal modes is $\nu_N - \nu_M \cong 1.6\,\mathrm{MHz} = \Delta\nu/2$. By sweeping the frequency, alternating normal and Möbius modes appear, as demonstrated by curve (e), which (with respect to the observed signal) is identical to curve (b), but separated in frequency by the amount $\Delta\nu$.

As a further illustration, in Fig. 2(right panels), we demonstrate the case of three equally spaced soliton-like pulses in the ring with a temporal separation, that is, pumping period of $T_0/3$. Two normal modes and two Möbius modes are found. Again, normal and Möbius modes are observed to alternate with the same frequency interval.

Thus the phase sensitivity of the parametric pumping process constitutes a phase selection rule for the allowed eigenmodes of the ring. Owing to localized parallel pumping with frequency 2ν, the pumping gain is at maximum for phases πn, allowing for modes with a phase shift per loop of $2\pi n$ and $2\pi(n+1/2)$. The former values correspond to normal modes and the latter to Möbius modes.

To classify the multi-soliton modes found, we quote the soliton phase relative to the phase of an arbitrary chosen soliton, which we set to zero without loss of generality. A soliton having the same

phase will be indicated by “0”, and one with a phase difference of π by “π”. For $T_p = T_0$ only two one-soliton modes exist, a normal mode, (0)N, and a Möbius mode, (0)M. For the case of two-soliton modes we find, using combinatorics, four possible combinations: (00)N, (0π)N, (00)M, and (0π)M. However, the last two modes are physically identical, as they can be transferred into each other by shifting the origin of the timescale by $T_0/2$.

Some of the N-eigenmodes are expected to have broken symmetry, since they cannot evolve monotonously from their linear counterparts. We find that the (00)N mode has a linear counterpart, while the (0π)N mode has the predicted broken symmetry. This is experimental verification of a symmetry-breaking eigenmode, as predicted [4, 5]. A similar analysis for $T_p = T_0/3$ predicts the existence of four non-equivalent three-soliton modes: (000)N, $(0\pi0)$N, (000)M, and $(0\pi0)$M. All these modes are observed in the experiment, as demonstrated in Fig. 2.

To good approximation, the multi-soliton eigenmodes can be viewed as a set of soliton-like wave-packets with weak interaction in the case of a small overlap. We conclude by briefly reporting an experiment that unambiguously demonstrates this interaction. Using appropriate time gating we prepared a mode consisting of two solitons with a variable time separation, which travel about the ring. For simplicity, the pumping frequency is chosen in such a way that both solitons correspond to normal modes, that is their closed-loop phase shift is $2\pi n$. The relative phase of the first soliton is set to zero. Owing to phase selection imposed by the parametric pumping process, the phase of the second soliton can either be 0 or π. By reducing the time delay ΔT between the solitons one can investigate their interaction. It was experimentally found that independently of the initial phase difference between the solitons at large ΔT the phase difference between them for small delays is always π. This fact provides clear evidence of a phase-dependent interaction between the two solitons. The origin of the observed interaction is not clear so far and represents a challenge for future studies.

A full report will be published in Nature [18].

Support by the Deutsche Forschungsgemeinschaft is gratefully acknowledged.

References

[1] M. Remoissenet, *Waves Called Solitons: Concepts and Experiments* (Springer-Verlag, Berlin, 1966).
[2] L. Khaykovich et al., Science **296**, 1290 (2002).
[3] G. P. Agrawal, *Nonlinear Fiber Optics* (Academic, San Diego, 1995).
[4] L.D. Carr, C.W. Clark, W.P. Reinhardt, Phys. Rev. A **62**, 063610 (2000).
[5] L.D. Carr, C.W. Clark, W.P. Reinhardt, Phys. Rev. A **62**, 063611 (2000).
[6] X. Liu, K.J. Qian, F.W. Wise, Phys. Rev. Lett. **82**, 4631 (1999).
[7] M. Bauer et al., Phys. Rev. Lett. **81**, 3769 (1998).
[8] Yu.S. Kivshar, B.A. Malomed, Rev. Mod. Phys. **61**, 763 (1989).
[9] Z. Li, L. Li, H. Tian, G. Zhou, K.H. Spatschek, Phys. Rev. Lett. **89**, 263901 (2002).
[10] B.A. Kalinikos, M.M. Scott, C.E. Patton, Phys. Rev. Lett. **84**, 4697 (2000).
[11] B.A. Kalinikos, N.G. Kovshikov, M.P. Kostylev, H. Benner, JETP Lett. **76**, 310 (2002).
[12] B.A. Kalinikos, N.G. Kovshikov, C.E. Patton, Phys. Rev. Lett. **80**, 4301 (1998).
[13] G. Steinmeyer, D.H. Sutter, L. Gallmann, N. Matuschek, U. Keller, Science **286**, 1507 (1999).
[14] A.V. Bagada, G.A. Melkov, A.A. Serga, A.N. Slavin, Phys. Rev. Lett. **79**, 2137 (1997).
[15] P.A. Kolodin et al., Phys. Rev. Lett. **80**, 1976 (1998).
[16] G.A. Melkov et al., Phys. Rev. E **63**, 066607 (2001).
[17] J.M. Nash, P. Kabos, R. Staudinger, C.E. Patton, J. Appl. Phys. **83**, 2689 (1998).
[18] S.O. Demokritov, A.A. Serga, V.E. Demidov, B. Hillebrands, M.P. Kostylev and B.A. Kalinikos, Nature **426**, 159 (2003).

6.5 Black soliton formation from phase-adjusted spin wave packets

A.A. Serga, A. Andre, S.O. Demokritov, and B. Hillebrands[1]

An envelope dark soliton can be understood as a stable propagating dip in a carrier wave of otherwise constant amplitude in a nonlinear medium. The characteristic feature of such a dark soliton is a nonzero jump in the phase of its carrier wave as one crosses the dip [1, 2]. In the case of a black soliton, when the maximum depth of its dip is equal to the amplitude of the carrier wave, this phase shift is exactly equal to 180°.

The number of the formed dark solitons, as well as their amplitude and phase characteristics, strongly depend on the initial conditions, i.e., on the amplitude and phase modulation of the carrier wave before it enters the nonlinear medium. In a magnetic system, as studied here, so-called microwave magnetic envelope (MME) dark solitons evolve from an initial gap created in the carrier spin wave *without any special phase modulation* [3,4]. In this case only *multiple* solitons should be formed, so the phase jumps in successive solitons are compensated, and the net phase shift across the entire output signal is equal to an integer multiple of 360°. However the process of soliton formation can be strongly modified by the diffrent nonlinear phenomena.

Here we report on a new approach to create single dark and black MME solitons as well as on the first experimental observation of a so-called excitation-induced nonlinear phase shift. This phase shift is created by the gradual entrance of a relatively slow spin wave into the nonlinear magnetic medium and is proportional to the duration of the input dark pulse and to the power of its carrier wave (see Eqs. (2), (3) in Ref. [5]). A spin wave pulse of duration t_0 will accumulate a phase shift since its leading edge propagates for the time t_0 longer in the nonlinear medium than its trailing edge. We show that the pre-compensation of this phase shift is a necessary condition for the formation of a single black MME soliton with a 180° phase jump.

Figure 1 shows a schematic diagram of the experimental setup. Its main part is a spin-wave waveguide, which consists of a strip of a single-crystal yttrium-iron-garnet (YIG) film on a gadolinium gallium garnet substrate and a pair of short-circuited microstrip antennae. The YIG film shown by

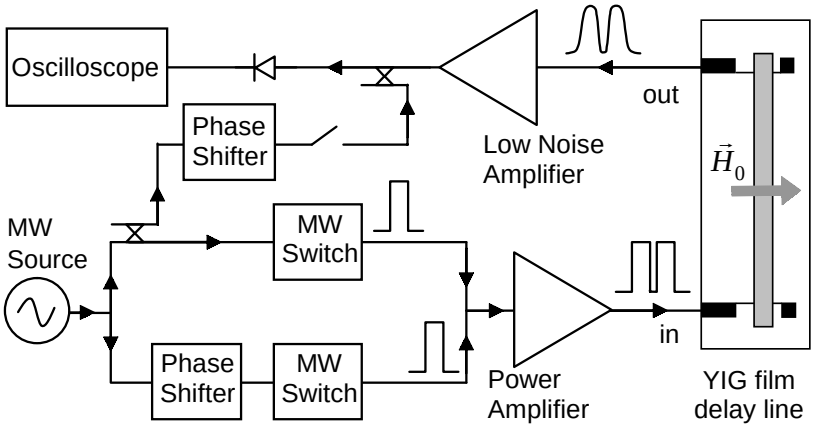

Fig. 1: Schematic diagram of the microwave (MW) experimental setup.

[1] In collaboration with A.N. Slavin, Department of Physics, Oakland University, Rochester, Michigan, USA.

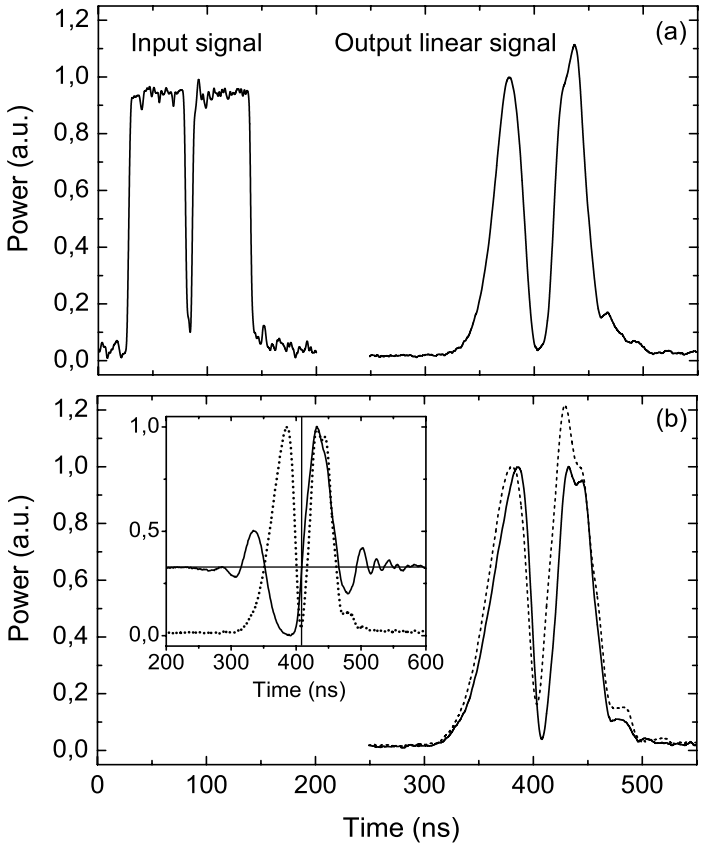

Fig. 2: Normalized output signals formed from the input pulses with 6 ns gap. Frames (a) and (b) correspond to the input power of 0.2 mW (linear case) and 28 mW (nonlinear case). In (b) the dashed line shows the profile of a dark soliton obtained by using the parameters as in (a) apart from the larger input power. The solid-line profile corresponds to the black soliton obtained after phase adjustment by 50°, as described in the text. The inset in (b) shows the interference signal resulting from interference of the output black soliton signal with a monochromatic reference signal (solid line) together with the black soliton (dotted line). The 180°phase jump coincides with the position of the soliton dip.

a shaded rectangular in Fig. 2 has the following parameters: length, width, thickness are 18 mm, 1 mm, and 5 µm, respectively; saturation magnetization: $4\pi M_s = 1750$ G. The 10 GHz ferromagnetic resonance linewidth $2\Delta H$ is 0.55 Oe. The film has unpinned surface spins.

The antennae are situated transversely to the long side of the YIG sample and are separated by 8 mm. One of the antennae is used for the excitation of spin waves and the other for their detection after travelling the distance between the antennae. The antennae's width and length are 50 µm and 2.5 mm, respectively.

The sample was magnetized by a static magnetic field of $H_0 = 1745$ Oe applied in the film plane and transversely to the long edge of the strip, see Fig. 1. The input SW signal was exited by an electromagnetic wave with a carrier frequency of $\omega_s = 2\pi \cdot 6.950$ GHz. In this case, the input antenna excites magnetostatic surface waves (MSSW) with carrier wave number $k_s = 85\,\mathrm{rad/cm}$. For unpinned films these MSSW have a monotonic dispersion curve $\omega(k)$ with both negative dispersion, $D = \partial^2\omega/\partial k^2$, and negative nonlinearity, $N = \partial^2\omega/\partial|u|^2$, where u is the amplitude of the wave. As the positive product $ND > 0$ allows for dark type solitons [1–3, 5], the MSSW are able to form dark envelope solitons while travelling between the antennae.

In order to vary the initial phase shift over the gap in the carrier wave, the input signal was composed of two coherent electromagnetic microwave pulses with controlled phase shift between them in the range $(0, 2\pi)$ (see Fig. 1 and Fig. 2a). The initial gap duration T was varied in the range from 5 ns to 15 ns by changing the delay time between the pulses. The aggregate signal was amplified by a power amplifier with controlled gain and sent to the input antenna of the spin wave delay line (1). The input peak power P_{in} was varied in the range from 0.2 mW up to 50 mW. The total duration of the aggregate input signal was restricted to 100 ns to avoid additional nonlinear processes. For example, a further increase of P_{in} and/or the pulse duration leads to a pronounced suppression and

distortion of the pulses due to four-magnon decay into exchange dominated short-wavelength spin waves.

To analyze the phase jump inside the output signal we measured the signal obtained by interference of the output signal with a phase adjusted reference signal from the microwave source (Fig. 1).

First, we discuss the linear case, i.e., $P_{in} = 0.2\,\mathrm{mW}$. The shape of the output signal is shown in Fig. 2a. Due to the distortions created by the limited frequency band of the delay line and by the spin wave dispersion in the film, the two pulses forming the output signal have bell-like profiles and the initially rectangular $T = 6\,\mathrm{ns}$ wide gap spreads up to 28 ns (measured at half-depth level). As a result of a slight dispersion-induced phase modulation of the carrier wave the lowest amplitude in the dip was found to be non-zero. A proper adjustment of the phase shift in the input pulse sequence brings the two delayed pulses back to the case of destructive interference in the region of their overlap. Thus, the amplitude in the dip becomes almost exactly equal to zero. The actual value of this adjustment of the initial phase depends on the gap width T.

An increase of the input power P_{in} results in the crossover from the linear to the nonlinear regime of spin wave propagation. The nonlinear regime causes two simultaneous changes in the shape of the output signal: the central dip of it becomes narrower and the minimum amplitude in the dip increases as shown by the dashed curve in Fig. 2b. This narrowing provides a clear evidence of the dark soliton formation [3]. The threshold power of this process is about 7 mW. We note, that the two maxima surrounding the dip in the output pulse demonstrate a slight broadening with increasing P_{in}, because the nonlinear distortions add to the dispersion spreading of pulsed signals in the case of $ND > 0$

The detected reduction in the depth of the dark soliton dip is a consequence of the nonlinearity-induced spatial phase modulation of the carrier MSSW. If some phase shift of opposite sign is introduced into the two pulses comprising the input signal, the depth of the dip tends to become zero, while the phase jump over the dip in the output pulse tends to equal the initial 180° value. Thus, the measurement of the value of the compensating phase shift introduced by the external phase shifter (Fig. 1) provides us with information about the intrinsic excitation-induced nonlinear phase modulation.

Figure 3 shows the dependence of the measured induced phase shift on the input power P_{in} for two gap widths $T_1 = 6\,\mathrm{ns}$ and $T_2 = 15\,\mathrm{ns}$, respectively. In accordance with theoretical predictions [5] the induced phase shift $\phi(u) \propto C/T + |u|^2 NT$ (see Eq. (2) in Ref. [5]) increases with increasing power ($\propto |u|^2$) of the excited spin waves, while the dependence on T is more complicated. This behavior is clearly seen for the values of the input power above the threshold of dark soliton formation ($P_{in} > 7\,\mathrm{mW}$). For the smaller values of the input power (i.e. in the linear region) the accuracy of our phase measurements is rather low, which prevents us from making a quantitative comparison of our experimental data with the results of the theory [5] in this linear region.

If the input power exceeds 35 mW for $T = 15\,\mathrm{ns}$ the phase shift starts to saturate. This is accompanied by the appearance of distortions in the shape of the output pulse caused by the above mentioned process of parametric excitation of short exchange-dominated spin waves.

The above described phase adjustment technique enables us to observe the formation of a single black spin wave envelope soliton under well-determined circumstances. For example, adjusting the phase shift in the input pulse sequence we were able to maximize the depth of the initially created dark soliton in such a way that the amplitude at the dip minimum is almost exactly zero (see Fig. 2), and a pronounced single black soliton state was achieved for $P_{in} = 28\,\mathrm{mW}$ and $T_1 = 6\,\mathrm{ns}$. The width of the obtained black soliton is comparable with the width of the originally formed dark soliton

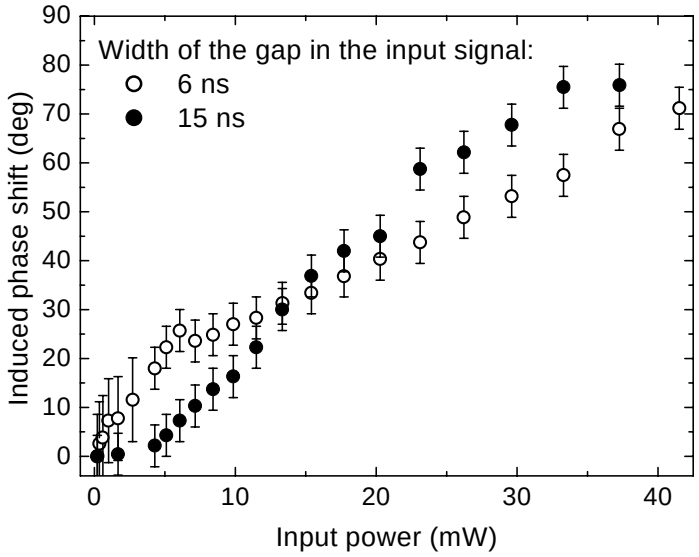

Fig. 3: Excitation-induced nonlinear phase shift across the dip in the carrier spin wave as a function of the input power.

having non-zero amplitude at the minimum of its dip.

The inset in Fig. 2b shows the interference of the output pulse, corresponding to this black soliton, and the monochromatic reference signal. The transition from destructive to constructive interference marks the pronounced 180° phase jump inside of the black soliton. When P_{in} is increased above 28 mW the soliton appearance becomes even more pronounced: the dip becomes narrower and steeper. However, in this strongly nonlinear regime it is difficult to separate the influences of the different nonlinear processes (formation of a soliton and excitation of exchange-dominated spin waves), and the picture becomes less clear.

To summarize, the formation of a single dark spin wave envelope soliton was experimentally realized for long-wavelength surface magnetostatic spin wave using as an input signal a sequence of two microwave radio-pulses with controlled gap and phase shift between them. The variation of the depth of the generated dark soliton and the creation of the fundamental black soliton state were achieved via manipulating the phase shift between the pulses in the input sequence. The excitation-induced nonlinear phase shift in the output dark pulse (soliton) was experimentally observed. The artificial pre-compensation of the nonlinear phase shift enables us to observe the generation of a single fundamental black spin wave envelope soliton having a 180° phase jump.

This work was partially supported by the Deutsche Forschungsgemeinschaft, by the National Science Foundation, Grant No. DMR-0072017, and by the Oakland University Foundation.

References

[1] M. Remoissenet, *Waves Called Solitons: Concepts and Experiments* (Springer-Verlag, Berlin, 1966).
[2] A.N. Slavin, IEEE Trans. Magn. **31**, 3479 (1995).
[3] M. Chen, M.A. Tsankov, J.M. Nash, C.E. Patton, Phys. Rev. Lett. **70**, 1707 (1993).
[4] J.M. Nash, P. Kabos, C.E. Patton, R. Staudinger, J. Appl. Phys. **79**, 5367 (1996).
[5] A.N. Slavin, Yu.S. Kivshar, E.A. Ostrovskaya, H. Benner, Phys. Rev. Lett. **82**, 2583 (1999).

6.6 Parametric generation of forward and phase-conjugated spin-wave bullets in a magnetic film

A.A. Serga, S.O. Demokritov, and B. Hillebrands[1]

Although predicted for light [1], wave bullets – stable two-dimensional nonlinear wave packets self-focused in space and time – were first experimentally observed in the system of spin waves in yttrium-iron garnet (YIG) films [2]. The experimental investigation of wave bullets in magnetic films has the advantage of direct two-dimensional access to the medium and of the possibility to follow the bullet formation and propagation in real time due to its relatively low speed (compared to the speed of light) using the space- and time-resolved Brillouin light scattering technique [3]. An additional advantage is the fact that in garnet films it is possible to realize an effective parametric interaction of a propagating spin-wave packet with non-stationary (pulsed) electromagnetic pumping [4].

Here, in contrast with the traditional method of spin-wave bullet formation from an initially nonlinear input spin wave packet directly excited using a microwave antenna, we report the experimental generation of two-dimensional spin wave bullets in both amplified and phase conjugated reversed wave packets formed as a result of parametric interaction of an initial spin wave packet with electromagnetic pumping of double frequency.

The experiment utilized a spin-wave waveguide situated on top of a microstrip structure as shown in Fig. 1, which was designed for transformation of an electromagnetic signal into spin waves and vice versa. Two microstrip antennae of 25 µm width and 2 mm length spaced 8 mm apart were lifted 100 µm up above the surface of the structure to avoid the direct contact of the YIG film with the other parts of the circuit and, as a result, to eliminate any undesirable excitation of parasitic spin waves by the microstrip feeders. One of the antennae was used for excitation of spin waves, while the second was used for real time monitoring of the propagated spin wave signal.

The wide ($4.1 \times 30\,\mathrm{mm}^2$) spin-wave waveguide was cut out from a single crystal YIG(111) film with thickness of 5 µm, grown on a gallium-gadolinium garnet substrate. The film's saturation mag-

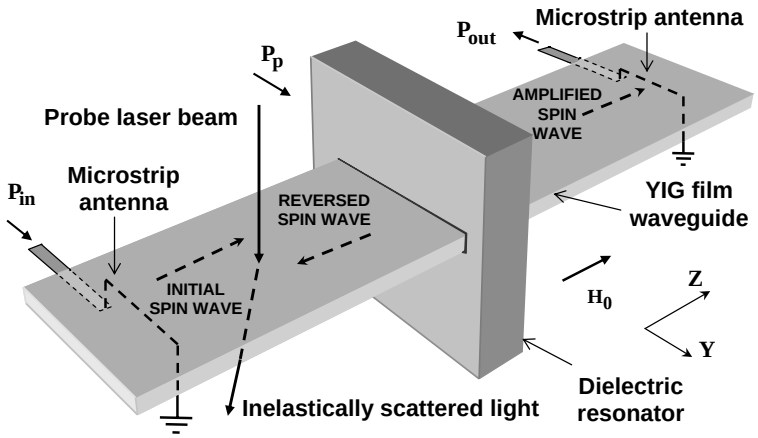

Fig. 1: Experimental setup.

[1] In collaboration with A.N. Slavin and P. Wierzbicki, Department of Physics, Oakland University, Rochester, Michigan, USA, as well as with V. Vasyuchka, O. Dzyapko, and A. Chumak, Department of Radiophysics, Taras Shevchenko National University of Kiev, Kiev, Ukraine.

netization is $4\pi M_s = 1750\,\mathrm{G}$ and the full linewidth of ferromagnetic resonance is $2\Delta H = 0.6\,\mathrm{Oe}$. The sizes of the waveguide were chosen to be larger than the sizes of the antennae, the distance between them, and the characteristic length of non-linear packet formation [5, 6].

A rectangular dielectric resonator of a special shape was developed to create a pumping magnetic field inside the YIG film. The resonator sizes are $1 \times 9.45 \times 5.85\,\mathrm{mm}^3$. The waveguide was mounted in a thin (0.8 mm) slot in the center of the resonator, where the intensity of the rf magnetic field of the used resonator mode $\mathrm{TE}_{11\delta}$ has its maximum. In this case the pumping magnetic field is applied along the long side of the waveguide and parallel to the direction of spin wave propagation. The resonance frequency and loaded quality factor were equal to $f_p = 7.932\,\mathrm{GHz}$ and 184, respectively.

The bias magnetic field H_0 was applied along the z axis (see Fig. 1), i.e., in the plane of the film and perpendicular to the antennae. Thus, as the thin microstrip antenna excites efficiently only dipolar dominated spin waves propagating perpendicularly to the antenna's axis, the geometry of the experiment corresponds to magnetostatic backward volume waves (MSBVW). These waves are able to form envelope bullets. Note here that in this geometry the rf pumping magnetic field coincides with the direction of the bias field, and thus the case of a parallel pumping is realized [7].

The MSBVW packets were excited by the rectangular electromagnetic pulses of duration 30 ns with carrier frequency $f_s = 3.966\,\mathrm{GHz}$ and varying power P_{in}. For the applied bias field $H_0 = 800\,\mathrm{Oe}$ the excited MSBVW packets have a carrier wave number of $k_z = 95\,\mathrm{rad/cm}$.

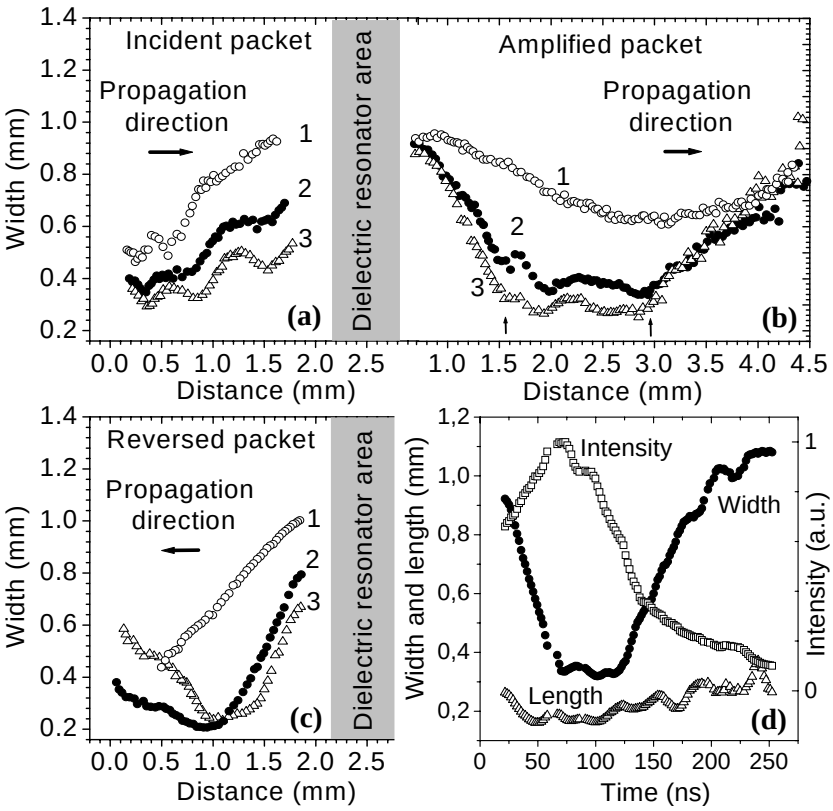

Fig. 2: Changes of spin-wave packet characteristics with propagation distance z and time t. Evolutions of the transversal width L_y of the incident, amplified and reversed spin wave packets are shown in Frames (a), (b), and (c) respectively. Curves (1), (2), and (3) correspond to the input powers P_{in} of 22 mW, 146 mW, and 226 mW, respectively. Frame (d) displays the time evolutions of the width L_y and length L_z, as well as of the pulse's amplitude for the amplified spin wave pulse with $P_{in} = 226\,\mathrm{mW}$.

Using the space- and time-resolved BLS technique [3] two-dimensional maps of the spin wave intensity $I(y,z)$, each sampled over a time interval of 1.7 ns, were recorded. Using these maps the mean packet position $(z_0(t), y_0(t))$ and the transverse packet width L_y as well the longitudinal length L_z can be easily determined as functions of the propagation time and distance [8].

The pumping pulse with duration of 39 ns and peak power 30 W was applied when the spin-wave packet passes through the dielectric resonator. As a result the maximum amplification of the delayed pulse observed on the output antenna reached 27 dB. Simultaneously with the amplification of the input spin-wave packet the reversed spin wave packet propagated in backward direction with respect to the initial packet was formed by strongly amplified thermal spin waves. The amplitude of these packets depends both on the power P_{in} of the input pulse and the pumping power. To avoid overheating of the sample around the resonator as well as other uncontrolled effects the pumping power and duration were fixed and the amplitudes of the amplified and reversed pulses were controlled only by the variations of P_{in} in the range from 2.2 mW to 700 mW.

First, let us consider spin-wave bullet formation from a spin wave packet on the way to the resonator. The evolution of the incident packet as a function of the input power $2.2 \leq P_{in} \leq 22$ mW is characterized by a monotonic widening of the packet (see curve 1 in Fig. 2a). A further increase of the input power up to 226 mW leads to a pronounced nonlinear compensation of the transversal widening of the packet followed by spin-wave bullet formation. Increasing P_{in} above 500 mW results in strong transversal compression of the spin wave packet followed by its fast collapse and destruction. A systematic oscillatory behavior of L_y shown in Fig. 2a is caused by the interference of a few spin-wave width-modes in the YIG waveguide [9].

As a result of the parametric interaction with the microwave magnetic field in the region of the dielectric resonator the propagating spin wave packet increases its length and width. Just behind the resonator (as it is seen in Fig. 2b) the widths L_y both of the previously linear (curve 1) and of the nonlinear (curves 2-3) spin wave packets are practically identical. However, the further behavior of the amplified spin wave packet depends on the power. At the same time the main features of the packets' evolution are common for all input powers P_{in}, as seen in Fig. 2b. First, the amplified packet is essentially transversally compressed. Second, the compressed packet keeps its width for a long propagation path. For example, in the case of $P_{in} = 226$ mW the propagation distance, where the packet width L_y is practically constant, is about 1.5 mm (marked with two vertical arrows in Fig. 2b).

As it is seen in Fig. 2d the described process of the transversal narrowing is accompanied by a simultaneous decrease of the spin-wave packet length L_x and increase of the packet intensity, which is due to the strong spatial concentration of the spin wave energy.

Thus, the process of spin-wave packet compression has a two-dimensional character and leads to the formation of the stable two-dimensional nonlinear spin wave excitation, the spin wave bullet.

As the input power P_{in} increases the compression process develops faster and the compression degree rises (Fig. 2b). An increase of P_{in} above 300 mW results in a wave collapse and breaking of the packet into parts.

The behavior of the reversed spin wave packet is even more intriguing. Due to two-dimensional phase-conjugation by means of parametric interaction, a distinct transmission narrowing is observed even for quasi-linear packets (see curve 1 in Fig. 2c). Comparing the slopes of the curves 1 in Fig. 2a and Fig. 2c one can conclude, that the above effect is the counterpart of the diffraction broadening of the initial spin wave packet. An increase of P_{in} involves an additional nonlinear self-focusing of the spin wave packet in the process. It is remarkable that not only the compression

develops faster, but, as it is shown in Fig. 2, the strongly compressed reversed spin wave packet moves as a solitary stable two-dimensional excitation. The broadening of this nonlinear reversed spin wave packet (see curve 2 in Fig. 2c) is much slighter in comparison with its previous compression and is caused by the diffraction which plays a more and more important role with dissipation of the spin-wave packet energy and the diminishing influence of the nonlinearity. Thus, Fig. 2c clearly demonstrates that there are profound regions of propagation distances (or times) where the transverse sizes of the reversed wave packets are almost constant, i.e., where propagation of self-generated bullets is observed.

Thus, for the first time we have observed bullet formation both by parametrically amplified spin wave packets and by the phase conjugated spin waves parametrically generated from the thermal level.

As the characteristic behavior of the observed bullets does not relay on the method of the initial excitation of the waves packets they can be classified as a two-dimensional natural excitation of a nonlinear medium with dispersion, diffraction and dissipation.

This work was supported by the Deutsche Forschungsgemeinschaft, by the U.S.A. National Science Foundation (Grants No. DMR-0072017 and INT-0128823).

References

[1] Y. Silberberg, Opt. Lett. **15**, 1282 (1990)
[2] M. Bauer, O. Büttner, S.O. Demokritov, B. Hillebrands, V. Grimalsky, Yu. Rapoport, A.N. Slavin, Phys. Rev. Lett. **81**, 3769 (1998).
[3] S.O. Demokritov, B. Hillebrands, A.N. Slavin, Phys. Reports **348**, 441 (2001).
[4] G.A. Melkov, A.A. Serga, A.N. Slavin, V.S. Tiberkevich, A.N. Olejnik, A.V. Bagada, JETP **89**, 1189 (1999).
[5] O. Büttner, M. Bauer, S.O. Demokritov, B. Hillebrands, Yuri S. Kivshar, V. Grimalsky, Yu. Rapoport, A.N. Slavin, Phys. Rev. B **61**, 11576 (2000).
[6] R.A. Staudiner, P. Kabos, H. Xia, B.T. Faber, C.E. Patton, IEEE Transactions on Magnetics **34**, 2334 (1998).
[7] A.G. Gurevich G.A. Melkov, *Magnetic Oscillations and Waves* (CRC, New York, 1996).
[8] A.A. Serga, S.O. Demokritov, B. Hillebrands, A.N. Slavin, J. Appl. Phys. **93**, 8758 (2003).
[9] O. Büttner, M. Bauer, C. Mathieu, S.O. Demokritov, B. Hillebrands, P.A. Kolodin, M.P. Kostylev, S. Sure, H. Dötsch, V. Grimalsky, Yu. Rapoport and A.N. Slavin, IEEE Trans. Magn. **34**, 1381 (1998).

C. Magnetic Films and Double Layers

6.7 Surface smoothing and reduction of Néel "orange peel" coupling for magnetic tunnel junctions using low energy argon ions

P.A. Beck, B.F.P. Roos. S.O. Demokritov, and B. Hillebands

There is great interest in improved preparation methods for ultrathin metallic films driven by applications such as giant magneto-resistance (GMR) elements and magnetic tunnel junctions (MTJ) [1]. MTJs consist typically of a sandwich structure with a pinned ferromagnetic layer (typically Co or CoFe) and a free ferromagnetic layer (typically permalloy, NiFe) separated by an insulating layer. For usage in applications such as magnetic random access memory (MRAM) or read heads in hard disk drives, a small and reproducible switching field for the free layer is strongly desired. The morphology of the interface has a great influence on the switching field. It was Néel who first considered magnetic dipole coupling between the two layers due to rough interfaces, so-called "orange peel coupling" [2]. Schrag et al. have shown that magnetostatic and Néel coupling are responsible for the coupling between the pinned and free magnetic layer in MTJs [3, 4].

Not only the amplitude of the roughness but also its lateral scale determine the strength of the Néel coupling. If a coherent sinusoidal roughness profile with amplitude h and wavelength λ is assumed, the coupling field H_N acting on the free layer in a "pinned layer/barrier/free layer" stack is given by

$$H_N = \frac{\pi^2}{\sqrt{2}} \frac{h^2}{\lambda t_f} M_s \exp\left(\frac{-2\pi\sqrt{2}\, t_b}{\lambda}\right) \quad , \tag{1}$$

where t_f is the thickness of the free layer, t_b that of the barrier, and M_s the magnetization of the pinned layer. At given h the coupling field increases with increasing wavelength λ, reaches its maximum at $\lambda_{max} = 2\pi\sqrt{2}\, t_b$, and then it exponentially decreases. Thus the Fourier components of the interface roughness near λ_{max}, which is about 10 nm for a typical MTJ, are of largest importance for the Néel coupling mechanism.

The as-grown interface roughness is determined by the thermodynamics and kinetics of the growth process and the deposition technique, and it cannot be reduced beyond certain limits. Here we report the realization of a successful post-fabrication smoothing process based on low energy argon ions. In agreement with theoretical models the coupling field measured on MTJs is largely reduced.

The stacks are prepared at room temperature in a multi-chamber molecular beam epitaxy system with a base pressure of $< 10^{-10}$ mbar using a five-pocket electron beam evaporator. The surface morphology is studied by *in-situ* scanning tunneling microscopy (STM). For the magnetic studies *ex-situ* magneto-optic Kerr effect (MOKE) magnetometry is used. All samples are prepared on thermally oxidized Si(100) substrates with an 100 nm thick SiO_2 layer. For the STM studies a single 15 nm thick Py layer was used. The magnetic properties are determined for full MTJs made by depositing 2.6 nm Al_2O_3/3 nm CoFe/2 nm Cr onto the Py layer. The Al_2O_3 barrier layer is prepared by plasma oxidation of a metallic Al film [5] using the same plasma source as for surface smoothing. The surface smoothing process has been performed in normal incidence in a separate reactor chamber with base pressure $< 10^{-9}$ mbar, with sample transfer without breaking

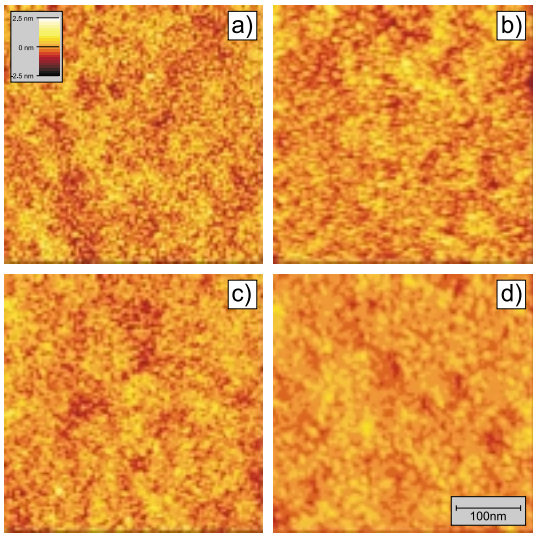

Fig. 1: STM images of the surface morphology of a 15 nm thick $Ni_{19}Fe_{81}$ film on a SiO_2 substrate: a) before ion bombardment and b-d) after irradiation with argon ions with an ion dose of $8 \cdot 10^{16}$ ions/cm^2. The ion energy is b) 30 eV, c) 50 eV and d) 70 eV.

the vacuum. The chamber is equipped with an inductively coupled radio frequency (13.56 MHz) plasma beam source providing a quasi-neutral Ar^+ plasma beam. The ion energy can be chosen in the range of $20-90$ eV with a dispersion of less than ± 5 eV. The current density is typically $50-70\,\mu$A/cm^2.

The surface roughness of a thin film can be roughly characterized by characteristic height and lateral structure parameters. As roughness-height parameters the so-called peak-to-valley roughness (r_{pv}) and the root-mean-square roughness (r_{rms}) are commonly used. They are directly obtained from the analysis of the STM images. Additionally a lateral correlation length ξ can be determined from the height-height correlation function [6]. Figure 1a shows a typical STM image of an as-grown 15 nm thick Py film. Characteristic are small grains with an average size in the order of 10 nm. From the analysis of the images the following values are derived: $r_{rms} = 0.45$ nm, $\xi = 45$ nm. Figure 1b-d shows the Py surface after irradiation by Ar ions of different energies but with the same ion flux of $8 \cdot 10^{16}$ ions/cm^2. It illustrates the change in the surface morphology by the irradiation process. The derived parameters are summarized in Fig. 2, which shows that both r_{pv} and r_{rms} are drastically decreased by the irradiation process. For 70 eV the value of r_{rms} drops below 0.3 nm. On the contrary the irradiation causes an essential increase of ξ by a factor of more than 100%. Thus, the presented experimental data indicate a significant surface smoothing effect

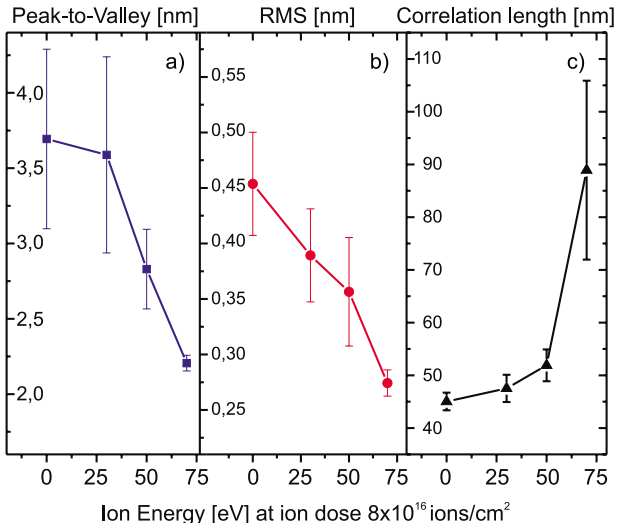

Fig. 2: Ion energy dependence of the surface properties of a 15 nm thick $Ni_{19}Fe_{81}$ film on a SiO_2 substrate: a) Peak-to-Valley roughness , b) root mean square roughness, c) correlation length.

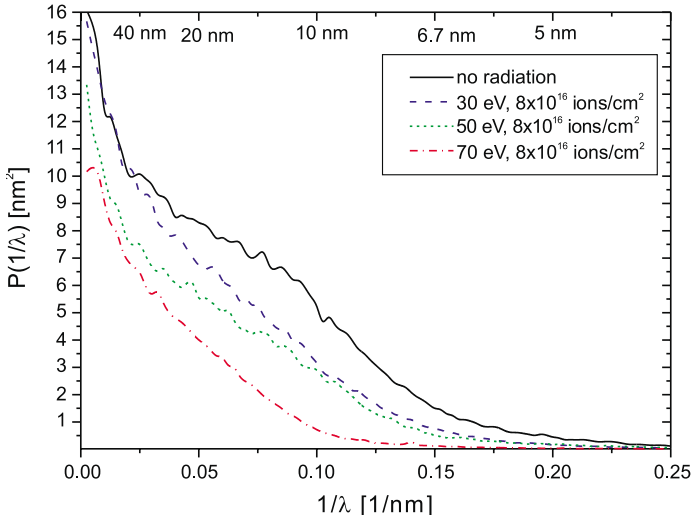

Fig. 3: Power spectra of the surface morphology of a 15 nm thick $Ni_{81}Fe_{19}$ film on SiO_2 obtained by a Fourier analysis of the STM images.

by the irradiation with low energy argon ions.

For a more detailed characterization of the surface smoothing effect the Fourier power spectra of the STM images are analyzed. Figure 3 shows Fourier power spectra of several STM images. For each image the spectrum was calculated for a single line with a following average over all parallel lines of the image. The shown Fourier spectra clearly demonstrate the smoothing effect for different lateral scales. The smoothing is observed for all values of the analyzed lateral scales, but is most pronounced for $\lambda = 5 - 40$ nm, which is in agreement with the data shown in Fig. 2c.

As it is discussed above, $5 - 50$ nm is the interval of the lateral length components of the roughness, which mainly contribute to the Néel interlayer coupling for typical barrier widths of $0.5 - 2$ nm. As seen in Fig. 3, even 30 eV ions significantly reduce the roughness with a lateral characteristic length of $5 - 40$ nm. It is more pronounced for 50 eV ions. The strongest effect is observed for 70 eV ions, which provide a smoothing in a broad range from 5 nm to 100 nm. One can conclude that structures in the roughness with a characteristic lateral length scale below 10 nm are almost completely suppressed.

Unfortunately, smoothing using ions with an energy exceeding a certain threshold, which typically is 50 eV, may cause also undesirable effects, such as the creation of defects. To study this, the impact of surface smoothing on magnetic interlayer coupling is investigated by studying the magnetization loops of full MTJs. Figure 4 shows the magnetization loops for 15 nm NiFe/2.6 nm Al_2O_3/ 3 nm CoFe/2 nm Cr MTJs, based on Py films with different surface roughness prepared by applying the smoothing process. The magnetization loop of a single 3 nm CoFe/2 nm Cr layer is also presented in Fig. 4 for comparison. One can clearly see the switching of the two magnetic layers in different fields. Due to a smaller coercive field of NiFe it is switched first in a weak field. After this the ferromagnetic “orange peel” coupling between the NiFe and CoFe layers trends to shift the switching field of the CoFe layer to weaker fields with respect to that of a single CoFe layer. Thus, increasing the switching field of the CoFe layer in MTJs based on the smoothed NiFe layers can be considered as the experimental confirmation of the reduced coupling. The reduced coupling, as it is also seen in Fig. 4, causes an increase of the switching field of the NiFe layer. The effect is not so strong as it is for the CoFe film due to the much larger thickness of the NiFe layer, but it demonstrates the symmetry of the coupling. In agreement with the STM data, Fig. 4a and 4b

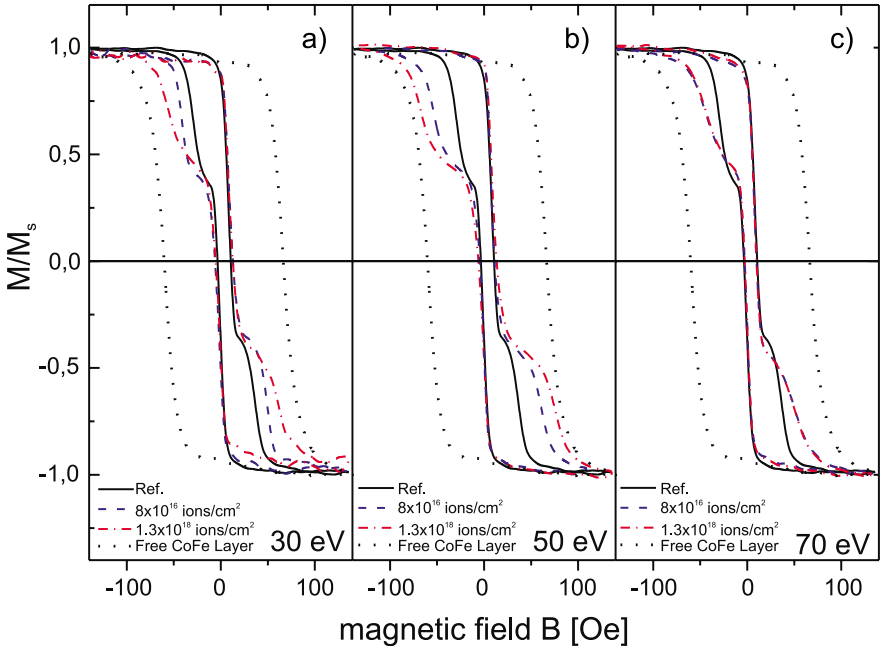

Fig. 4: Magnetization reversal loops measured with MOKE magnetometry for two different ion doses and for a) 30 eV, b) 50 eV, and c) 70 eV ion energies for Si/SiO_2/15 nm $Ni_{81}Fe_{19}$/2 nm Al_2O_3/3 nm $Co_{90}Fe_{10}$/2 nm Cr. For reference, loops of a as-grown sample and of a single free 3 nm $Co_{90}Fe_{10}$/2 nm Cr stack on SiO_2 is shown in all graphs.

show that irradiation with 50 eV ions causes a stronger reduction of the coupling, as it is detected for 30 eV ions. However, a further increase of the ion energy up to 70 eV does not decrease the coupling. Instead, the remagnetization loop of CoFe layer looses its squareness. The origin of this effect is not clear up to now, although defect generation is likely.

In conclusion, we have found that irradiation with 50 eV argon ions of relatively low fluences of $10^{16} - 10^{17}$ ions/cm^2 causes an essential smoothing effect for NiFe layers, the roughness on a typical length scale of $5 - 40$ nm being mostly reduced. The reduced roughness clearly manifests itself in a reduced Néel “orange peel” coupling, measured on realistic MTJ structures, prepared on the smoothed NeFe layers.

Financial support by the BMBF is gratefully acknowledged.

References

[1] J.S. Moodera, L.R. Kinder, T.M. Wong, R. Meservey, Phys. Rev. Lett. **74**, 3273 (1995).
[2] L. Néel, Comptes Rendus Acad. Sci. **255**, 1676 (1962).
[3] B.D. Schrag, A. Anguelouch, S. Ingvarsson, G. Xiao, Y. Lu, P.L. Trouilloud, A. Gupta, R.A. Wanner, W.J. Gallagher, P.M. Rice, S.S.P. Parkin Appl. Phys. Lett. **77**, 2373 (2000).
[4] B.D. Schrag, A. Anguelouch, G. Xiao, P.L. Trouilloud, Y. Lu, W.J. Gallagher, S.S.P. Parkin, J. Appl. Phys. **87**, 4682 (2000).
[5] B.F.P. Roos, P.A. Beck, S.O. Demokritov, B. Hillebrands, J. Appl. Phys. **89**, 6656 (2001).
[6] H.N. Yang, Y.P. Zhao, A. Chan, T.M. Lu, G.C. Wang, Phys. Rev. B **56**, 4224 (1997).

6.8 High resolution magnetic patterning of exchange coupled multilayers

V.E. Demidov, D.I. Kholin, S.O. Demokritov, and B. Hillebrands[1]

The antiferromagnetic interlayer exchange coupling between two ferromagnetic layers separated by a thin nonmagnetic spacer was discovered in 1986 by Grünberg et al. [1]. Since then this phenomenon has been intensively studied (for a recent review see [2]) because of its potential for the creation of antiferromagnetically coupled media for high-density magnetic recording [3, 4] and artificial antiferromagnets that are used as hard magnetic electrodes for magnetic memory elements [5, 6] and magnetoresistive sensors [7].

Recently it was shown [8], that the type of the interlayer exchange coupling between two iron layers separated by a chromium spacer can be easily modified by ion irradiation. This modification is a result of the atomic intermixing at the Fe/Cr interface caused by the dissipation of energy of ions due to their collisions within the crystalline lattice. The intermixing at the Fe/Cr interface leads to the appearance of microscopic "magnetic bridges" that connect the two iron films and provide strong direct local ferromagnetic coupling between them. With increase of the irradiation fluence the quantity of magnetic bridges increases and the type of interlayer coupling changes to the ferromagnetic one. Since the direct coupling through a bridge is about hundred times stronger than that via the spacer the density of bridges and, consequently, the ion fluences necessary to change the type of coupling is very small [8]. It is obvious that the modification of the exchange interlayer coupling by means of ion irradiation provides a very convenient tool for local modification of magnetic properties of antiferromagnetically coupled layers. Due to the possibility to focus the ion beam down to very few tens of nanometers the proposed technique opens the way for the creation of novel artificial magnetic media such as thin-film structures containing nano-scaled areas having different magnetic susceptibility. Moreover, due to the moderate ion penetration depth into standard photoresist, which usually does not exceed $50-100\,\mathrm{nm}$, one can realize ion nano-patterning using standard resist mask technology.

In this paper we present first experimental results on the laterally resolved ion beam modification of the interlayer exchange coupling in Fe/Cr/Fe trilayers.

For the experimental investigation samples were prepared consisting of two 10 nm thick Fe(001) films separated by a 0.7 nm thick Cr spacer. The chosen thickness of the Cr spacer corresponds to a strong antiferromagnetic coupling between the Fe layers. Using an ultra high vacuum molecular-beam epitaxy system the Fe/Cr/Fe(001) trilayers were epitaxialy grown on a MgO (001) substrate with a 80 nm thick Cr buffer and covered by 3 nm of Cr in order to avoid corrosion. Finally the samples were irradiated using a focused ion beam lithography machine. Irradiation with a fluence of $6.25\cdot10^{15}\,\mathrm{ions/cm^2}$ was performed with 50 keV Ga^+ ions without applied external magnetic field with the samples being kept at room temperature. The ion beam focused down to approximately 100 nm was scanned along the surface of the sample forming square shaped irradiated areas with dimensions of $200\times200\,\mu\mathrm{m}^2$ separated by 150 µm wide non-irradiated space [9]. The diagonals of the irradiated squares were aligned along the easy magnetic axes of the four-fold magnetic anisotropy of the Fe(001) films.

The samples as prepared were studied using Magneto-Optical Kerr-Effect (MOKE) magnetometry. The hysteresis loops were measured at different points of the samples. A magnetic field of up to

[1] In collaboration with F. Wegelin and J. Marien, IBM Mainz Materials Laboratory, Mainz, Germany.

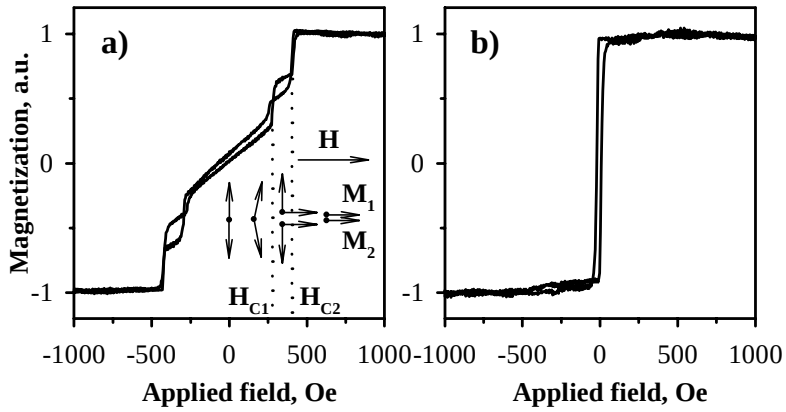

Fig. 1: Hysteresis loops for a non-irradiated (a) and an irradiated (b) area.

1.5 kOe was applied parallel to the easy magnetic axis. Typical results of the MOKE-measurements are presented in Fig. 1, where the two hysteresis loops shown correspond to a non-irradiated and an irradiated area, respectively. In order to illustrate the rotation of magnetization in the sample the vector diagram is added to Fig. 1a showing the relative orientation of the magnetic moments M_1 and M_2 of the two Fe layers for different values of the external magnetic field H. As seen from Fig. 1a, the non-irradiated trilayer structure exhibits typical antiferromagnetic magnetization curves in the range of the external magnetic field of ± 250 Oe. In this range the application of a magnetic field leads to a weak deviation of the magnetic moments M_1 and M_2 from their original antiparallel state, which results in the total magnetization of the trilayer to increase slowly with the increase of the field strength. As soon as the strength of the magnetic field reaches the critical value $H_{C1} = 250$ Oe, the total magnetization of the trilayer starts to increase stepwise. Such a behavior can be explained by a weak 90° interlayer exchange coupling [10] coexisting in the samples with the strong antiferromagnetic one. As a result, the orientation of the magnetic moments of the layers almost at 90° with respect to each other becomes favorable in the range of magnetic fields from 250 to 450 Oe and M_1 and M_2 orient close to the directions of magnetic easy axes (see the vector diagram in Fig. 1a). Finally, if the strength of the external magnetic field exceeds $H_{C2} = 450$ Oe the trilayer becomes completely saturated. In contrast to the complicated magnetic behavior of the non-irradiated Fe/Cr/Fe trilayer the irradiated trilayer simply exhibits a typical ferromagnetic hysteresis loop (see Fig. 1b) with the coercive field equal to 20 Oe.

Next, Magnetic Force Microscopy (MFM) measurements were performed in the regions situated close to the boundary between the irradiated and non-irradiated areas. For this purpose a multi-functional scanning probe microscope was used (Solver AFM-MFM produced by NT-MDT Co.). The microscope contains a built-in electromagnet, which allows one to investigate the domain structure of samples placed in an external magnetic field.

Figure 2 presents the MFM images of the corner of the irradiated area obtained in weak external magnetic fields, comparable to the coercive field of the irradiated area. The four panels a – d of Fig. 2 correspond to the strength of applied magnetic field H equal to -30, 0, 5, and 30 Oe, respectively. The magnetic field was applied along one of the magnetic easy axes, which are shown in the figure by black arrows. As seen from Fig. 2a, in the magnetic field of -30 Oe the boundary between the irradiated and non-irradiated areas provides very strong magnetic contrast, whereas the remaining surface is magnetically uniform. Such a behavior is understood by the strong difference in magnetizations of the irradiated and non-irradiated areas. The completely saturated irradiated area produces strong magnetic stray fields at its edges if surrounded by the non-irradiated trilayer with small net magnetization. As the external magnetic field decreases to zero (see Fig. 2b) the

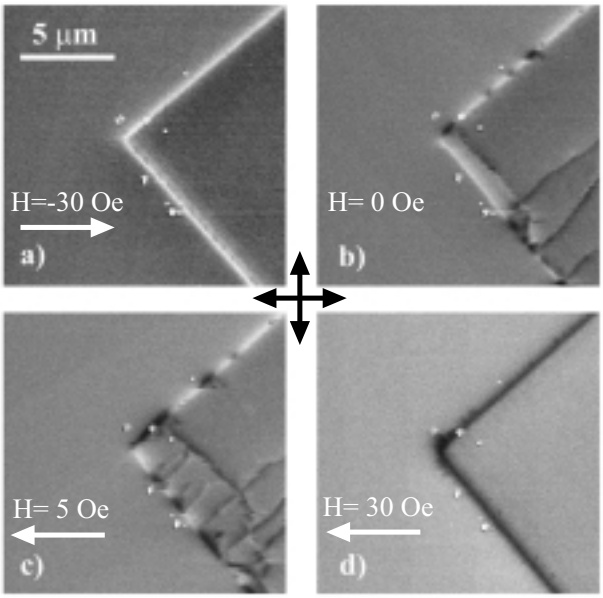

Fig. 2: Magnetic images of a corner of the irradiated area obtained in weak external magnetic fields: −30 Oe (a), 0 Oe (b), 5 Oe (c), 30 Oe (d). The black arrows indicate the easy axes of the four-fold magnetic anisotropy of the Fe(001) films.

irradiated area breaks up into domains, whereas the non-irradiated area remains uniform. As the magnetic field changes its direction and its strength increases again (see Fig. 2c and 2d) the domain structure in the irradiated area changes and finally disappears in a field exceeding 20 Oe, whereas the non-irradiated area does not demonstrate any visible change.

It is important to note here that for the whole range of magnetic fields between −30 and 30 Oe the magnetic boundary between the irradiated and non-irradiated areas is seen very sharply. This indicates that the strong magnetic moment of the irradiated ferromagnetic area does not have any considerable influence on the magnetization of the non-irradiated antiferromagnetic area in the boundary regions and, as a result, the change of magnetic properties at the boundaries between the irradiated and non-irradiated areas occurs very abruptly. As the upper estimate for the length, on which the change of magnetic properties occurs, the length of localization of the magnetic stray field can be taken. From measurements a value of about 200 nm is estimated. Consequently, one can conclude that ion irradiation provides a useful method for magnetic patterning of Fe/Cr/Fe trilayers with a lateral resolution, which is in any case not worse than 200 nm.

Of particular interest is the change in the properties of the boundaries between the irradiated and non-irradiated areas as a function of the external magnetic field. The MFM measurements show that the magnetic boundaries remain well defined in magnetic fields of up to about ±200 Oe. As the field strength approaches H_{C1} (see Fig. 1a) the magnetic images of the boundary regions start to demonstrate qualitative changes. This fact is illustrated by Fig. 3 where the MFM images are shown measured for the strength of the magnetic field equal to 210 Oe (a) and 250 Oe (b).

Unfortunately, in strong external magnetic fields the domain structure of the sample cannot unambiguously be derived from the MFM measurements due to the rotation of magnetization of the MFM tip out of its axis. However, it is clearly seen from Fig. 3 that in the boundary region the magnetization of the non-irradiated trilayer experiences a strong influence of the irradiated area. This phenomenon is caused by an instability of the magnetization in an antiferromagnetically coupled non-irradiated trilayer in magnetic fields lying close to H_{C1}. Due to the presence of the 90° coupling the alignment of the magnetic moments of the two Fe layers at 90° becomes favorable in the range of magnetic field between H_{C1} and H_{C2}. The strong magnetic stray field of the irradiated area stimulates the nucleation of the 90° phase in the non-irradiated area close to the boundary. As

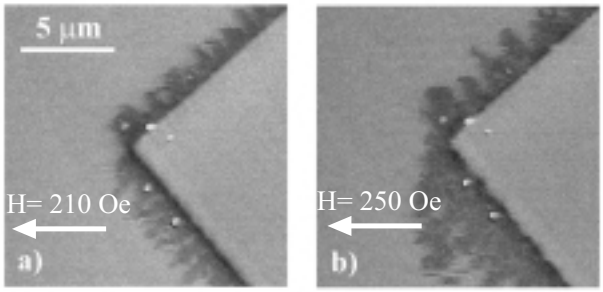

Fig. 3: Magnetic images of a corner of the irradiated area obtained in strong external magnetic fields: 210 Oe (a), 250 Oe (b).

a result the magnetic boundary between the irradiated and non-irradiated areas becomes wide.

In conclusion, we have demonstrated that local ion beam modification of the antiferromagnetic interlayer exchange coupling in Fe/Cr/Fe trilayers can be successfully used for magnetic patterning on the submicrometer scale. Such patterning provides a unique mean to create antiferromagnetic thin-film structures containing micrometer-size ferromagnetic areas with a very abrupt change of magnetic properties at their boundaries. The performed investigation shows that the well-defined magnetic boundary between irradiated and non-irradiated areas exists in a large range of the external magnetic field.

A full report has been submitted to Applied Physics Letters [11].

The work is supported in part by the European Communities Human Potential Programme (contract number HPRN-CT-2002-00296 NEXBIAS) and by the Deutsche Forschungsgemeinschaft through the Priority Programme 1133 “Ultrafast Magnetization Processes”.

References

[1] P. Grünberg, R. Schreiber, Y. Pang, M.B. Brodsky, H. Sowers, Phys. Rev. Lett. **57**, 2442 (1986).
[2] D.E. Bürgler, S.O. Demokritov, P. Grünberg, M.T. Johnson, Handbook of Magnetic Materials, vol. 13, Ed. K.J. H. Buschow, Elsevier, Amsterdam (2001).
[3] E.E. Fullerton, D.T. Margulies, M.E. Schabes, M. Carey, B. Gurney, A. Moser, M. Best, G. Zeltzer, K. Rubin, H. Rosen, M. Doerner, Appl. Phys. Lett. **77**, 3806 (2000).
[4] K. Tang, M. Doerner, Q.-F. Xiao, L. Tang, M. Mercado, J. He, R. Prichard, P. Rice, J. Appl. Phys. **93**, 7402 (2003).
[5] J. Schmalhorst, H. Brueckl, G. Reiss, R. Kinder, G. Gieres, J. Wecker, Appl. Phys. Lett. **77**, 3456 (2000).
[6] H. Brueckl, J. Schmalhorst, H. Boeve, G. Gieres, J. Wecker, J Appl. Phys. **91**, 7029 (2002).
[7] K. Bal, H.A.M. van den Berg, D. Deck, Th. Rasing, J Appl. Phys. **90**, 5228 (2001).
[8] S.O. Demokritov, C. Bayer, S. Poppe, M. Rickart, J. Fassbender, B. Hillebrands, D.I. Kholin, N.M. Kreines, O.M. Liedke, Phys. Rev. Lett. **90**, 97201-1 (2003).
[9] The relatively large size of the irradiated squares was chosen in order to allow local magnetooptical measurements of hysteresis loops in different areas.
[10] S.O. Demokritov, J. Phys. D **31**, 925 (1998).
[11] V.E. Demodov, D.I. Kholin, S.O. Demokritov, B. Hillebrands, submitted to Appl. Phys. Lett.

6.9 Measurement of the three magnetization vector components of a $Ni_{81}Fe_{19}$ film

H. Nembach, M.C. Weber, J. Fassbender, and B. Hillebrands

The magnetization dynamics in thin magnetic films can be investigated in the frequency domain with Brillouin light scattering (BLS) and ferromagnetic resonance (FMR), and in the time domain with inductive, resistive and optic techniques. One main advantage of the optic techniques in the time domain is that they allow one to measure all three components of the magnetization vector. This is important for studies on precessional dynamics where large-angle excitations are considered. The knowledge of the experimentally determined trajectory allows for a comparison with numerical simulations. The importance of spin wave propagation effects for the damping process can also be evaluated. If, for example, the magnitude of the magnetization vector is conserved, the generation of spin waves is an unlikely contribution to the damping mechanism.

The *calibrated* method for the determination of all three magnetization vector components in time and space presented here goes back to Ding et al. [1], who employed this procedure for the measurement of the spin reorientation transition in Co/Au(111). For the measurements a typical magneto-optic Kerr effect setup in longitudinal geometry is used. The light is s-polarized and the rotation of the polarization upon reflection at the sample surface is given by:

$$\theta_{Kerr} = \theta_L \cdot m_L + \theta_P \cdot m_P \tag{1}$$

with θ_{Kerr} the measured Kerr rotation, θ_L the longitudinal magneto-optical constant, θ_P the polar magneto-optical constant, m_L the longitudinal and m_P the polar magnetization component. The polarization of the incident light is not sensitive to the transversal magnetization component. The knowledge of the two magneto-optical constants θ_L and θ_P is essential to determine the magnetization vector components. In order to determine these two constants an in-plane and an out-of plane hysteresis curve is measured. The following procedure is employed to measure all three magnetization components, see Fig. 1.

The static and the dynamic magnetic field are both in the film plane and oriented perpendicular to each other. The frame of reference is fixed with the sample. After each measurement the sample together with the dynamic and static magnetic field is rotated counterclockwise by 90°. The three

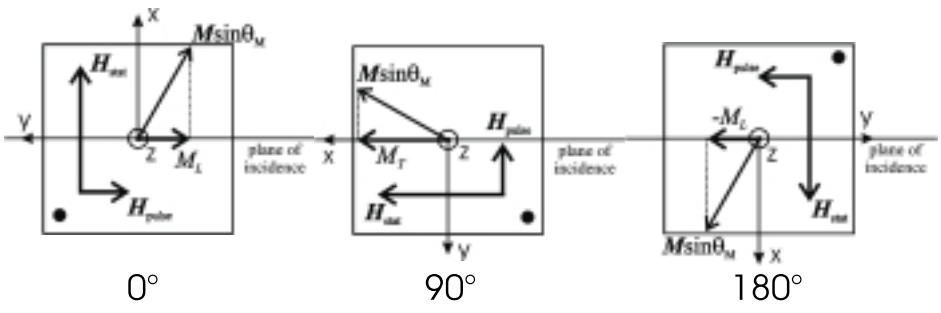

Fig. 1: The three different orientation of the setup which are used to determine all three components of the magnetization vector [2].

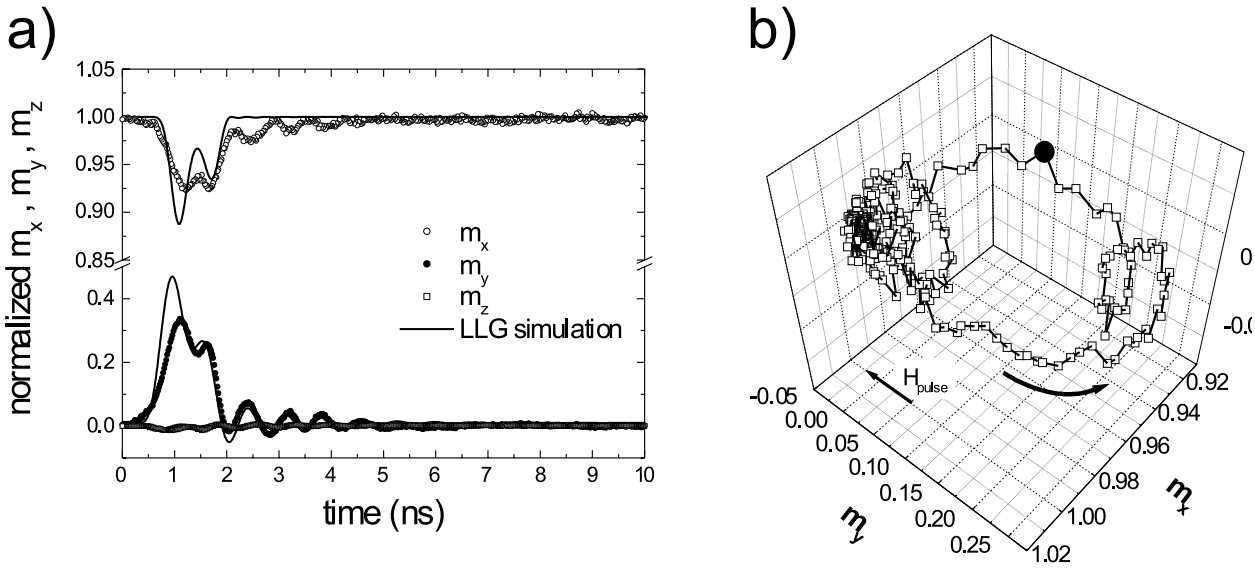

Fig. 2: a) The time evolution of the three calibrated and normalized magnetization components m_x, m_y and m_z are shown by open and filled circles and by squares, respectively. The lines show the results of a simulation based on the Landau-Lifshitz-Gilbert equation assuming a pulse with linear slopes. b) Trajectory of the magnetization vector after application of the magnetic field pulse. The equilibrium position is $[1,0,0]$. The termination of the field pulse is indicated by the black dot. The arrow marks the direction of the applied field pulse.

magnetization components m_x, m_y and m_z can then be determined in the following way:

$$m_z = \frac{1}{2\theta_P} \cdot (\theta_{Kerr}(0^\circ) + \theta_{Kerr}(180^\circ)) \tag{2-a}$$

$$m_y = \frac{1}{2\theta_L} \cdot (\theta_{Kerr}(0^\circ) - \theta_{Kerr}(180^\circ)) \tag{2-b}$$

$$m_x = \frac{1}{\theta_L} \cdot (\theta_{Kerr}(90^\circ) - \theta_P m_z) \tag{2-c}$$

$\theta_{Kerr}(0^\circ)$, $\theta_{Kerr}(90^\circ)$ and $\theta_{Kerr}(180^\circ)$ are the measured Kerr rotation angles in the respective configurations.

In order to demonstrate this procedure the magnetization trajectory is determined for a 20 nm thick $Ni_{81}Fe_{19}$ film. The film has been sputter deposited in an Edwards ESM 100 system with a base pressure of $3.6 \cdot 10^{-6}$ mbar on a $10 \times 10\,mm^2$ MgO substrate. It is (001)-oriented and has a thickness of 100 µm. The static bias field and the dynamic field pulse are 1440 A/m (18 Oe) and 800 A/m (10 Oe), respectively. The pulse length is 750 ps and its rise and fall times are estimated to be 600 ps and 900 ps respectively. The estimations are based on measurements with a high bandwidth oscilloscope on an un-shortened stripline with similar dimensions. These rather large rise and fall times are due to the impedance mismatch of the stripline with the connecting cables. The magneto-optical constants for the $Ni_{81}Fe_{19}$ film are determined to be $\theta_L = 0.038$ mdeg/G and $\theta_P = 0.36$ mdeg/G. The time-resolved measurements of the magnetization dynamics have been performed in all three measurement geometries. The time evolution of the magnetization components m_x (open circles), m_y (close circles) and m_z (squares) is shown in Fig. 2a.

The precessional frequency $\nu = 1.4$ GHz and the damping constant $\alpha = 0.008$ are determined from a comparison to a simulation based on the Landau-Lifshitz-Gilbert equation (solid line). The

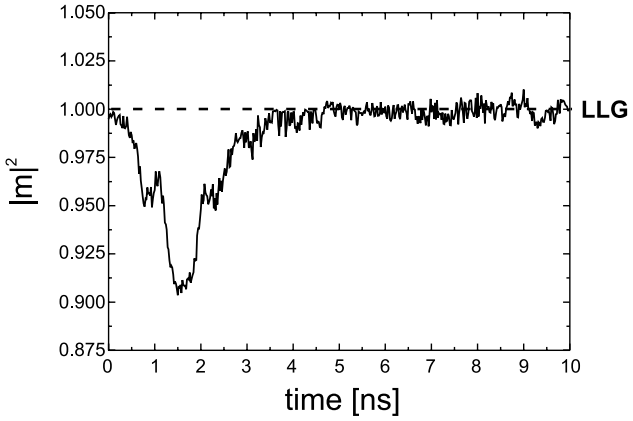

Fig. 3: Temporal evolution of the square of the magnetization vector. The magnitude of the magnetization vector is reduced by about 10%. The dashed line is the result from the Landau-Lifshitz-Gilbert equation in macrospin approximation, with the magnetization vector magnitude conserved.

magnetization trajectory is plotted in Fig. 2b. The equilibrium position of the magnetization vector is $[1,0,0]$ and the field pulse is applied in the $[0,\overline{1},0]$ direction. The termination of the field pulse is indicated with the black dot.

Figure 3 shows the temporal evolution of the square of the magnetization. A reduction of 10% is observed. This indicates the generation of spin waves. These spin waves can be either directly excited by the stripline or by multi-magnon processes. Due to our limited lateral resolution we cannot distinguish between these two origins.

In summary, a method for the determination of the magnetization trajectory is demonstrated. A reduction of the magnetization magnitude is observed. This is attributed to the generation of spin waves.

We like to thank R. Lopusnik for stimulating and helpful discussions and M. Thornton for providing the $Ni_{81}Fe_{19}$ sample.

A full report has been submitted to Journal of Applied Physics [3].

References

[1] H. Ding, S. Pütter, H. Oepen, J. Kirschner Phys. Rev. B **63**, 134425 (2001).
[2] R. Lopusnik, Dissertation, Universität Kaiserslautern (2001).
[3] H. Nembach, M. Weber, J. Fassbender, B. Hillebrands, submitted to J. Appl. Phys.

D. Exchange Bias Effect

6.10 Optical control of the magnetization in exchange biased NiFe/FeMn bilayers on the picosecond timescale

M.C. Weber, H. Nembach, J. Fassbender

Active research is focussed towards a deeper understanding of the origin of unidirectional anisotropy in bilayer systems consisting of a ferromagnetic (F) and an adjacent antiferromagnetic (AF) layer, both for fundamental and technological reasons. This unidirectional anisotropy is found for instance if the F-AF-bilayer system is cooled below the blocking temperature of the AF layer in an applied magnetic field. It is of large interest to investigate the exchange bias effect on short time scales, in particular in view of fast memory applications such as magnetic random access memory (MRAM) and media for hard disk and magneto-optical data storage [1–3].

Considerable insight has been gained from quasi-static magnetization reversal studies and theoretical micromagnetic modelling, indicating that the microstructure of the hetero-interface plays a key role in such systems [4–6]. For the dynamical properties two major effects must be considered here: First, using ultrashort laser pulses with durations in the range of several femtoseconds, the interplay between the spin-system and the electronic and phononic systems is time dependent. This has been studied by Ju et al. [7] who examined the NiFe/NiO exchange bias system by means of all-optical femtosecond pump-probe experiments. Second, and studied here, thermal heating of the interface is achived using picosecond laser pulses, and the temporal evolution is largely governed by the dynamics of heat flow. In both cases, precessional effects will also contribute, if the length of the laser pulse is shorter than the characteristic precession time.

The polycrystalline exchange bias samples have been prepared by UHV e-beam evaporation. As a growth template a 15 nm thick Cu buffer layer on top of a thermally oxidized Si substrate has been used. The exchange bias system itself consists of a 5 nm thick $Ni_{81}Fe_{19}$ (F) layer and a 10 nm thick $Fe_{50}Mn_{50}$ (AF) layer. Finally the sample is covered by a 2 nm Cr cap layer to protect it from oxidation. In order to initialize the exchange bias effect the sample was field cooled from above the blocking temperature (155 °C) after deposition. For further details see [8].

The time resolved experiments have been performed using a pump-probe technique in the following way (see also Chapter 6.17). A 9 ps short laser pulse is generated by a mode-locked diode pumped Nd:YVO_4 laser oscillator running with a repetition rate of 80 MHz and a wavelength of 1064 nm. The laser beam is inserted into a second-harmonic unit which maintains the pulse duration and delivers laser pulses of 532 nm wavelength. The linear polarization of the outgoing beam is defined by a combination of a retarding wave plate and a Glan-Laser polarizer. The polarized beam is then divided into an intense pump and a weak probe laser pulse by a beamsplitter. The 7 nJ pump pulse is directed nearly normal to the sample surface and focused to a spot diameter of 25 µm. The probe pulse is time delayed by a translation stage covering a time interval from a negative delay of -400 ps up to about 6 ns. The probe beam is used to sense the pump induced changes of the magnetization of the NiFe layer by means of the longitudinal magneto-optic Kerr effect (spot diameter: 20 µm). The sample has been patterned into $100 \times 100\,\mu m^2$ squares by means of optical lithography and wet chemical etching. The pump and probe spots are adjusted to the center of a square by maximizing the observed reflected light intensity and reducing stray reflections. Thus

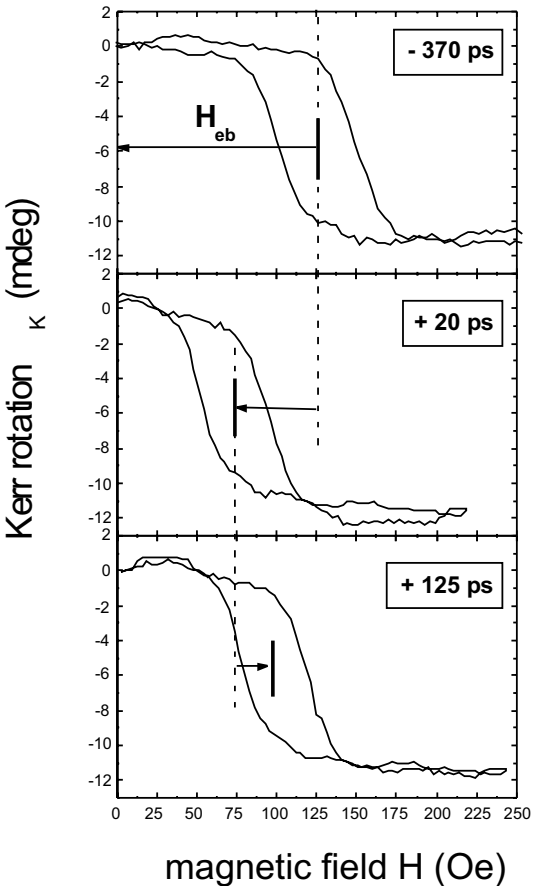

Fig. 1: Easy axis magnetization reversal loop for three different pump-probe delay times as indicated in the figure. The initial exchange bias field H_{eb} is indicated by a black arrow and the dashed lines are guides to the eye.

a good spatial overlap of both beams was achieved. In order to investigate the optical control of the magnetization in the time domain a quasi-static hysteresis loop is sensed by a probe pulse with a fixed time delay to the laser excitation pulse. The quasi-static hysteresis loop then reflects the magnetic parameters present for a given time delay.

First, the quasi-static hysteresis loop along the easy magnetization direction is investigated (see top graph in Fig. 1). This measurement has been performed using a negative time delay of 370 ps between pump and probe pulse, i. e., the probe pulse arrives 12.13 ns after the pump pulse. Within this time range all time-dependent effects are relaxed already (see Fig. 2). An exchange bias field of $H_{\mathrm{eb}} = 123\,\mathrm{Oe}$ and a coercive field of $H_{\mathrm{C}} = 24\,\mathrm{Oe}$ are observed. For a positive delay time of 20 ps a maximum reduction of the exchange bias field to a value $H_{\mathrm{eb}} = 67\,\mathrm{Oe}$ is observed. The coercive field is also reduced correspondingly. For a time delay of 125 ps a partial recovery of the exchange bias field is already observed. In order to analyze in more detail the hysteresis loops with a fixed time delay to the pump pulse the exchange bias field values for time delays in the range between $-400\,\mathrm{ps}$ and 3000 ps are plotted as a function of delay time in Fig. 2. Within the first 20 ps a fast reduction of the exchange bias field of about 45 percent can clearly be observed, followed by a slower recovery to the initial bias field value. The open dots in Fig. 2 represent the exchange bias field values extracted from the three loops presented in Fig. 1. The data have been fitted to a phenomenological model introduced by Ju et al. [7]. This model describes the process of photomodulation by a time dependent single exponential driving term,

$$H_{\mathrm{eb}} = H_{eb,init}\,(1 - m \cdot \exp\,(-t/\tau)) \qquad (1)$$

where $H_{eb,init}$ describes the initial bias field value, m is the so called modulation depth, e.g., the strength of the photomodulation and τ represents the time constant of the recovery of the exchange

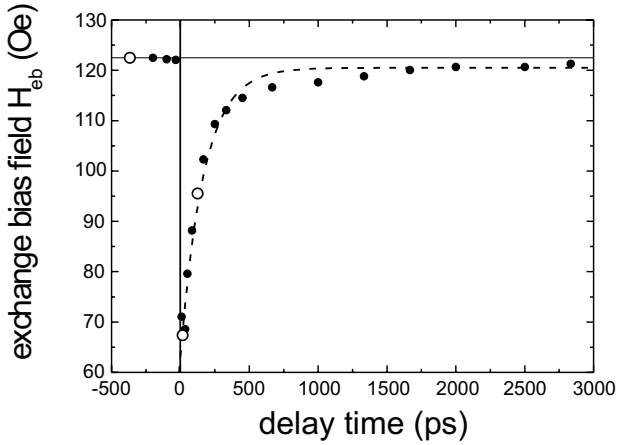

Fig. 2: Time dependance of the exchange bias field $H_{eb}(t)$ of an easy axis magnetization reversal loop. The open dots correspond to the hysteresis curves shown in Fig. 1. A fit of Eq. (1) with the parameters $m = 0.45$ and $\tau = 170\,\text{ps}$ is shown by a dashed line.

bias shift field. The best fit to our experimental values is shown as a dashed line in Fig. 2 with $m = 0.45$ and $\tau = 170\,\text{ps}$.

Next the zero field susceptibility of the hard axis magnetization reversal loops is investigated. It is addressed, whether the time dependence matches the one of the exchange coupling modulation found in the easy axis case. The quasi-static magnetization reversal loops taken at a negative delay time (not shown) show the expected hard axis behavior for exchange bias systems. Shortly after the arrival of the excitation pulse a dramatic change in the hard axis loop shape is observed. 20 ps after the heating pulse the loop shape resembles the shape of a NiFe easy axis loop. For larger delay times the hard axis behavior is starting to be restored. In order to analyze these data more quantitatively the zero field susceptibility has been extracted from the magnetization reversal curves by performing a linear fit to the data close to zero applied field. The slope corresponds to the zero field susceptibility χ, which is plotted in Fig. 3 as a function of the pump-probe delay time. Within the first 20 ps a sharp increase of χ is observed indicating a transition of hard magnetic magnetization reversal behavior to a nearly pure easy axis magnetization reversal hysteresis curve of NiFe. For larger delay times the susceptibility again reaches its initial value. Again the time constant involved is extracted by a fit to Eq. (1) with a modulation depth m^* and a recovery time τ^*. The best fit is achieved with the values of $\tau^* = 160\,\text{ps}$ and $m^* = 13.75\,\text{ps}$ (dashed line in Fig. 3). The time constants for easy and hard axis magnetization reversal are in good agreement indicating that both time dependencies rely on the mechanism of fast unpinning and recovery of the interfacial exchange coupling.

The experimental observation of both, the fast reduction of the exchange bias field and the strong increase of the susceptibility on a 20 ps timescale, can be understood in terms of a fast thermal unpinning of the exchange coupling at the F/AF hetero-interface upon arrival of the pump laser pulse. Within the laser pulse duration the temperature of the lattice system is elevated close to the blocking temperature of the exchange bias system. The exchange coupling is thus reduced and a nearly isotropic easy axis magnetization reversal behavior is observed. The relaxation time for the slow recovery process of both the exchange bias field and the susceptibility can be understood in terms of energy dissipation. The lattice system is cooled by heat flow from the metallic bilayer to the substrate or to a region outside the laser spot, setting the ultimate limit for the speed of recovery.

Currently the reduction of the exchange bias field is limited to about 45 percent of the initial value because for larger pump pulse energies irreversible processes start to occur, which obstruct the stroboscopic measurement scheme used here. Since the samples are polycrystalline, a distribution

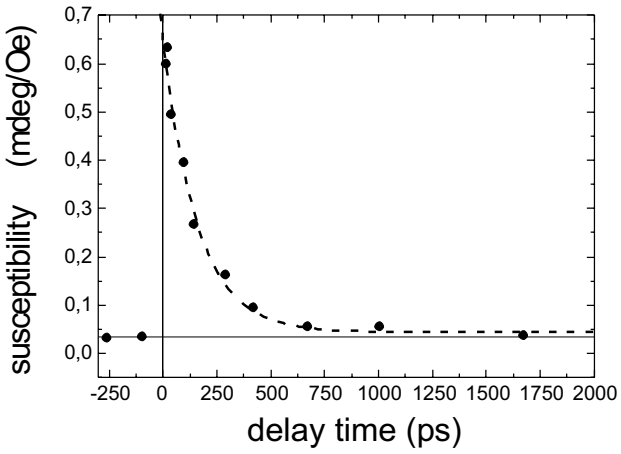

Fig. 3: Time dependance of the zero field susceptibility χ(t) of a hard axis magnetization reversal loop. The dashed line represents a fit to a modified version of Eq. 1 with a time constant of $\tau^* = 160\,\mathrm{ps}$.

of different AF grain sizes is present. According to Takano et al. [9] large AF grains at the interface of an exchange bias system exhibit a smaller exchange coupling to the F spins across the interface. Upon laser excitation these grains might already switch completely and will not relax to the original magnetization direction. In order to minimize the distribution width of the exchange-bias field values, measurements of epitaxial exchange bias systems are planned. Due to the different magnetization reversal processes in these epitaxial systems for easy and hard axis magnetization reversal also different time constants are expected. From the applications point of view it should be possible to optically trigger a coherent magnetization rotation which for instance can be used for fast thermo-magnetic writing and precessional dynamics of the F layer in an exchange bias layer system on a picosecond time scale.

This research was actively supported by Lumera Lasers GmbH in setting up and developing the laser equipment (see Chapter 6.17). The authors would like to thank S. Poppe for the sample preparation, H. Fouckhardt for the optical lithography support and B. Hillebrands for valuable discussions. M. Weber would like to acknowledge support by the Graduiertenkolleg “Nichtlineare Optik und Ultrakurzzeitphysik” of the DFG. The work is supported in part by the European Communities Human Potential programme under contract number HRPN-CT-2002-00318 ULTRASWITCH.

A full report has been submitted to Journal of Applied Physics [10].

References

[1] J. Nogués, I.K. Schuller, J. Magn. Magn. Mater. **192**, 203 (1999).
[2] R.L. Stamps, J. Phys. D: Appl. Phys. **33**, R247 (2000).
[3] A.E. Berkowitz, K. Takano, J. Magn. Magn. Mater. **200**, 555 (1999).
[4] A.P. Malozemoff, Phys. Rev. B **37**, 7673 (1988).
[5] T.C. Schulthess, W.H Butler, J. Appl. Phys. **85**, 5510 (1999).
[6] H. Ohldag, A. Scholl, F. Nolting, E. Arenholz, S. Maat, A.T. Young, M. Carey, J. Stöhr, Phys. Rev. Lett. **91**, 017203-1 (2003).
[7] G. Ju, A.V. Nurmikko, R.F.C Farrow, R.F. Marks, M.J. Carey, B.A. Gurney, Phys. Rev. Lett. **82**, 3705 (1999).
[8] A. Mougin, T. Mewes, M. Jung, D. Engel, A. Ehresmann, H. Schoranzer, J. Fassbender, B. Hillebrands, Phys. Rev. B **63**, 060409(R) (2001).
[9] K. Takano, R.H. Kodama, A.E. Berkowitz, W. Cao, G. Thomas, J. Appl. Phys. **83**, 6888 (1998).
[10] M.C. Weber, H. Nembach, J. Fassbender, submitted to J. Appl. Phys.

6.11 Investigation of the polycrystalline $Fe_{19}Ni_{81}/Fe_{50}Mn_{50}$ exchange bias system with varying Cu spacer layer for partial decoupling

M.O. Liedke, H. Nembach, J. Fassbender, and B. Hillebrands

The exchange coupling across an interface between a ferromagnetic and an antiferromagnetic layer may result in the so-called exchange bias effect evidenced by a shift of the hysteresis loop along the magnetic field axis. To study the role of the exchange interaction at and near the interface, $Fe_{19}Ni_{81}/Fe_{50}Mn_{50}$ bilayers have been studied, which have an intervening Cu layer of varying thickness and position in the antiferromagnetic $Fe_{50}Mn_{50}$ layer. The role of the intervening Cu layer is to generate partial exchange decoupling.

We have prepared and investigated a polycrystalline $Fe_{19}Ni_{81}/Fe_{50}Mn_{50}$ bilayer with an intervening wedge-shaped ($0-0.7$ nm) Cu layer. As the growth template a Si(111) wafer with a 15 nm thick Cu buffer layer was used. The thickness of the ferromagnetic $Fe_{19}Ni_{81}$ layer is 5 nm. On the top a wedge ($0-10$ nm) of the antiferromagnetic material $Fe_{50}Mn_{50}$ was grown. Next, the Cu spacer wedge was grown with the wedge direction perpendicular to the wedge direction of the $Fe_{50}Mn_{50}$ film. Finally, a wedge of $Fe_{50}Mn_{50}$ was grown on top with the opposite wedge direction compared to the first $Fe_{50}Mn_{50}$ layer resulting in a constant sum of the thicknesses of both $Fe_{50}Mn_{50}$ layers (see the sketches in Fig. 1). For protection a 2 nm thick Cr layer was deposited. As a result, a sample was obtained, where in one direction the position of the intervening Cu layer varies from the interface to the top surface of the $Fe_{50}Mn_{50}$ layer at constant Cu thickness, and in the other direction the Cu thickness varies. To initialize the exchange bias effect the sample was annealed above the Néel temperature and cooled in an applied field back to room temperature.

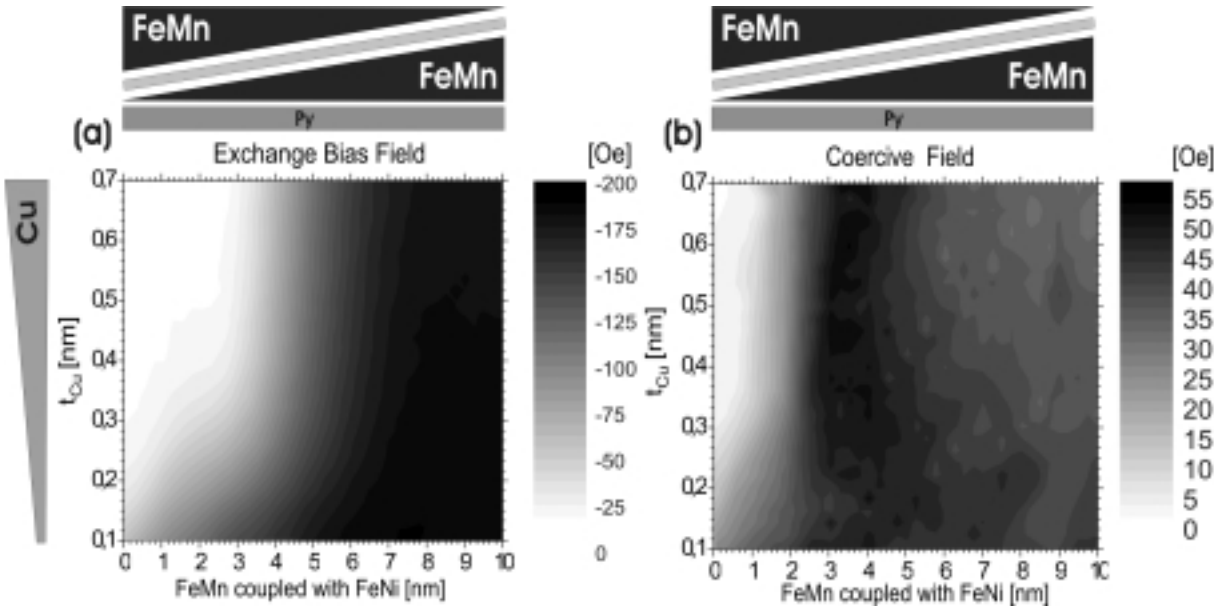

Fig. 1: Two dimensional scans of the sample: (a) exchange bias field H_{eb} and (b) coercive field H_c as function of the Cu spacer layer t_{Cu} (vertical direction) and the thickness t_{FeMn} of the lower $Fe_{50}Mn_{50}$ layer, which is directly exchange coupled to the $Fe_{19}Ni_{81}$ layer (horizontal direction).

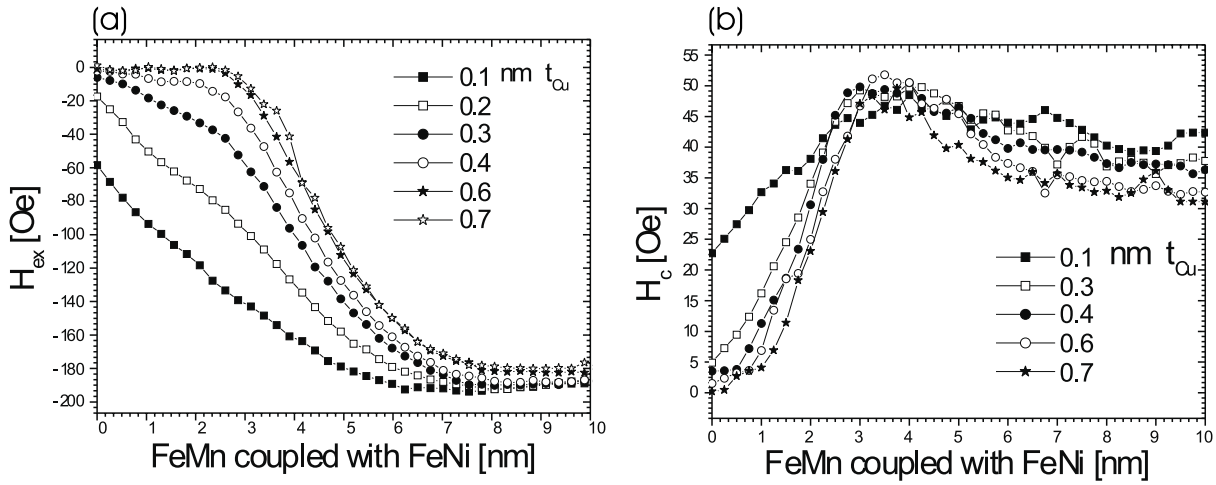

Fig. 2: (a) Exchange bias field H_{eb} and (b) coercive field H_c as a function of the Cu spacer layer t_{Cu} for different thicknesses t_{FeMn} of the $Fe_{50}Mn_{50}$ layer coupled with FeNi.

Hysteresis loops were measured as a function of position using magneto-optic Kerr effect magnetometry. From the loops the exchange bias field H_{eb} and the coercive field H_c were extracted as a function of the Cu spacer thickness, t_{Cu}, and the thickness t_{FeMn} of the lower $Fe_{50}Mn_{50}$ layer, which is directly exchange coupled to the $Fe_{19}Ni_{81}$ layer. The results are shown in Figs. 1, 2 and 3.

The obtained two-dimensional maps provide us easily with global information about the influence of the partial decoupling of the antiferromagnet as a function of t_{Cu} and t_{FeMn}. To obtain more quantitative information several line scans along the horizontal and vertical axes in Fig. 1 were evaluated. With increasing Cu thickness the absolute value of the exchange bias field H_{eb} decreases exponentially, see Fig. 2a. The coercive field H_c decreases rapidly for small values of t_{FeMn}, and it stays stable for $t_{FeMn} > 3\,\text{nm}$ achieving a maximum value of about 50 Oe, see Fig. 2. In case of $t_{FeMn} = 0$ the maximum value of the exchange bias field was not obtained for t_{Cu} approaching zero. This is likely due to the interrupted growth necessary for creating the intervening Cu layer. However a line scan along the Cu wedge for $t_{FeMn} = 0$ yields a dependence in good agreement with previous results [1].

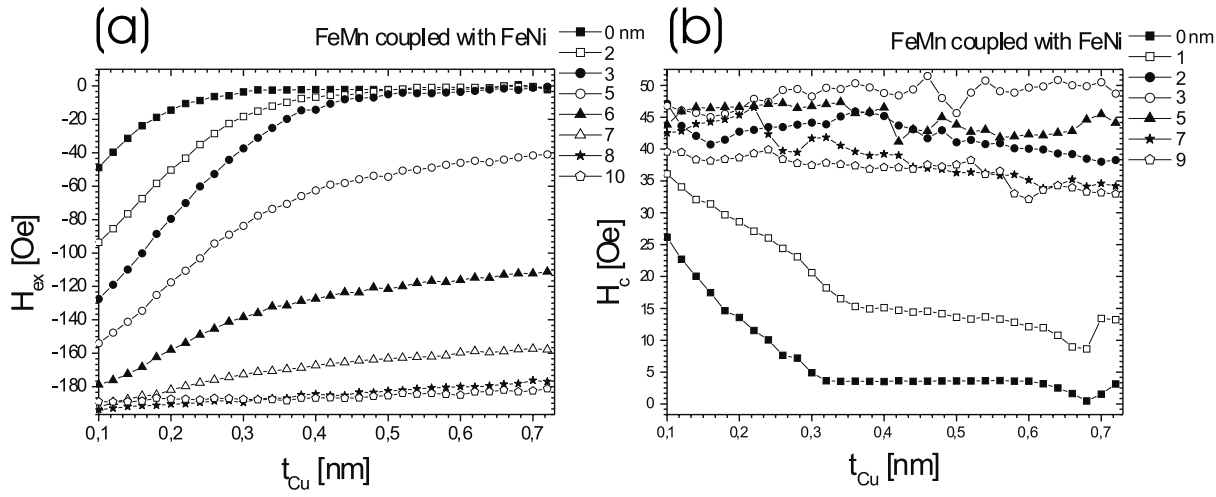

Fig. 3: (a) Exchange bias field H_{eb} and (b) coercive field H_c as a function of the thickness t_{FeMn} of the lower $Fe_{50}Mn_{50}$ layer coupled to FeNi for different thicknesses t_{Cu} of the Cu spacer layer.

In Fig. 3 the strong influence of the Cu spacer layer on the exchange bias field H_{eb} and the coercive field H_c as a function of its position in the stack, t_{FeMn}, is shown. Even for a 0.1 nm thick Cu spacer layer we observe a strong decrease of exchange bias value, which corresponds to a decrease of interfacial torques due to the partial decoupling, see Fig. 3a. On the other hand an influence of the upper wedge of $Fe_{50}Mn_{50}$ is observed, which is strong enough to maintain the unidirectional anisotropy. Considering Fig. 3b the coercive field exhibits a maximum for about $t_{FeMn} = 4$ nm. As a function of the Cu spacer thickness, t_{Cu}, the width of the maximum varies. However the position of the maximum in the coercive field does not follow the exchange bias field (Fig 3a) and stays stable for the same value of t_{FeMn}. This indicates that the coercive field is not directly connected to the origin of exchange bias coupling.

References

[1] T. Mewes, B. F. P. Roos, S. O. Demokritov, B. Hillebrands Appl. Phys. **87**, 5064 (2000).

6.12 Structural analysis of the $Ni_{81}Fe_{19}/Fe_{50}Mn_{50}$ exchange bias layer system

S. Blomeier, J. Fassbender, and B. Hillebrands[1]

The results presented here have been obtained during and following a stay of Steffen Blomeier in the group of Prof. J. Chapman at the University of Glasgow. For the structural analysis of the investigated layer system transmission electron microscopy studies were carried out there.

Recently it has been shown that the exchange bias effect in the polycrystalline $Ni_{81}Fe_{19}/Fe_{50}Mn_{50}$ exchange bias system, as well as in similar systems, can be modified by means of He^+-ion irradiation [1, 2], as shown in Fig. 1. Subject of this report is a careful search for irradiation induced structural changes using transmission electron microscopy (TEM).

If the irradiation is carried out without the application of an external field, an enhancement of the bias field for doses of up to $4 \cdot 10^{15}\,\mathrm{ions/cm^2}$ is found, whereas for larger doses a decrease of the bias field occurs. If the irradiation is carried out in a field, which is antiparallel to the field H_{prep}, applied during the field cooling procedure of the investigated sample, a change of the sign of the bias field can occur. In addition, an enhancement of the absolute value of the bias field is also found in this case, albeit the effect occurs at slightly higher doses and is less pronounced than in the case of a zero external field. For higher doses, a suppression of the bias field value is also found here. A model was proposed to understand the observed phenomena by attributing them to the creation of point defects [1, 3].

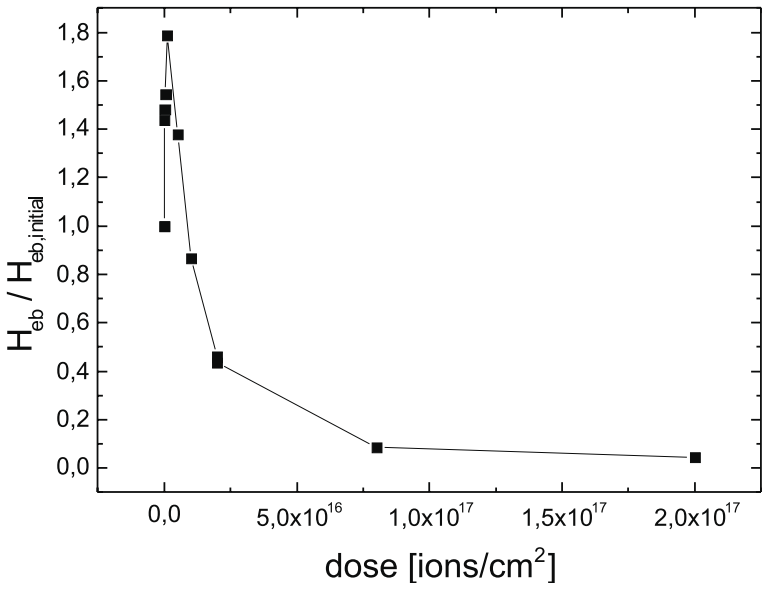

Fig. 1: Dependence of the exchange bias field of a polycrystalline $Ni_{81}Fe_{19}/Fe_{50}Mn_{50}$ system on the ion dose for an irradiation with 5 keV He^+-ions. The field axis is normalized to the initial bias field value for a non-irradiated sample.

[1] In collaboration with D. McGrouther, S. McVitie and J. Chapman, Department of Physics and Astronomy, University of Glasgow, Glasgow, United Kingdom.

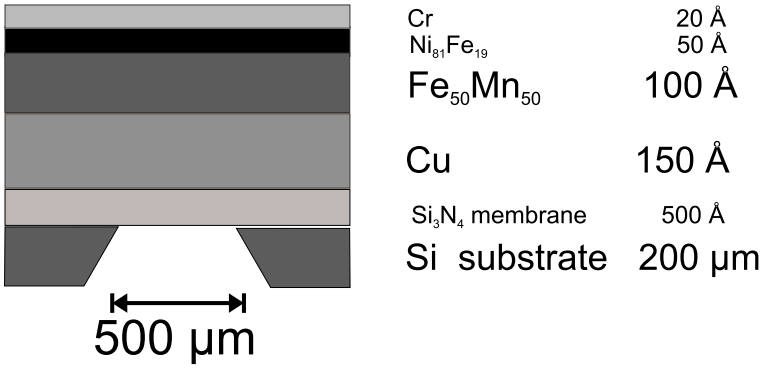

Fig. 2: Layer sequence of the investigated sample.

The structural analysis of a series of samples was carried out using the JEOL 2000FX electron microscope in Glasgow. To ensure the comparability of the obtained results, all samples were grown simultaneously in a UHV MBE system and subsequently irradiated with different doses of 5 keV He^+ ions. For the TEM studies samples are required to be electron-transparent, and they were thus grown on special window substrates, as shown in Fig. 2. These substrates consist of a 50 nm thick membrane of amorphous Si_3N_4, on top of which the layer system is deposited. The investigated layer system itself consisted of a 15 nm thick Cu buffer, followed by 10 nm of antiferromagnetic $Fe_{50}Mn_{50}$, 5 nm of ferromagnetic $Ni_{81}Fe_{19}$, and a chromium cap layer of 2 nm thickness.

Four samples irradiated with doses of 0, $2 \cdot 10^{15}$, $1 \cdot 10^{16}$, and $1 \cdot 10^{17}$ ions/cm^2 were investigated. Bright field images, dark field images and diffraction patterns were taken from each sample. The bright field and dark field images were used to determine the particle size distribution in the sample layers, while the diffraction patterns were used to determine their crystallographic structure, including lattice type, lattice constant and degree of texture. Figure 3 shows a typical result.

For the analysis of the bright field images a program written by T. Mewes was used, which allows one to determine the correlation length in a given greyscale image, which is taken as a measure for

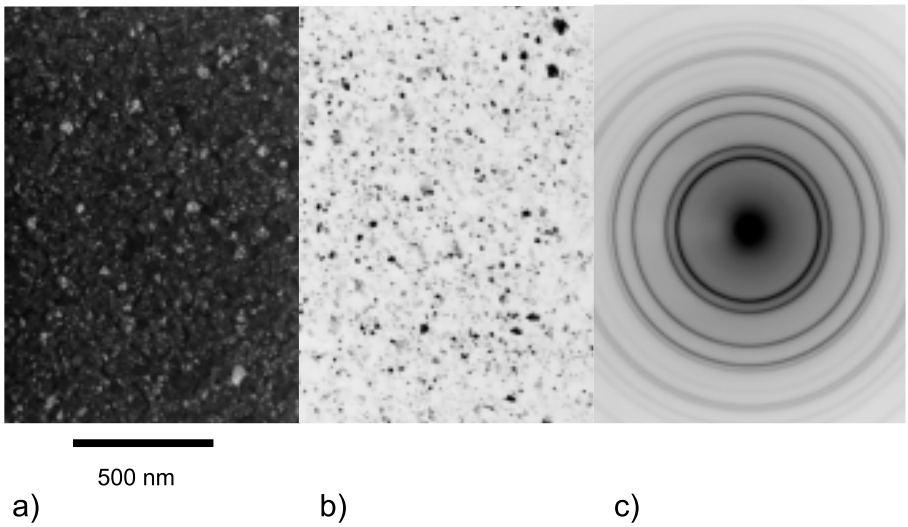

Fig. 3: (a): Bright field image of a sample irradiated with a dose of $1 \cdot 10^{17}$ ions/cm^2. (b): Dark field image from the same sample, on the same spot. (c): Diffraction pattern from the same sample.

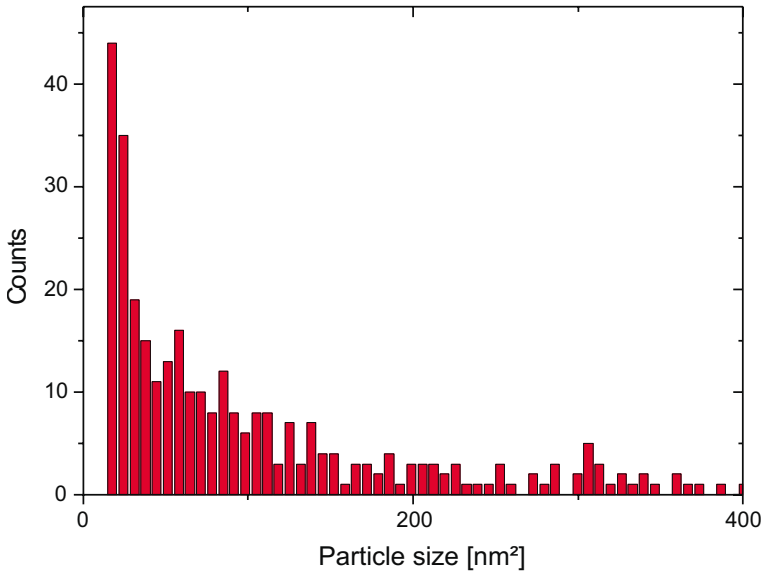

Fig. 4: Particle size distribution from the sample shown in Fig. 3. Particles are required to have an area of at least 20 nm^2, to exclude the effects of noise.

the average particle size [4]. For the analysis of the dark field images the software package ImageJ was used. A particle size distribution, as shown in Fig. 4, can be obtained directly by this method. From this size distribution, an average particle size can be derived, by taking the square root of the mean particle area as a measure for the average particle size.

An average particle size of 10.5 ± 2 nm is found. This size does not change within error bars for an increasing ion dose.

For the analysis of the diffraction patterns, a “trial-and-error”-method has been employed. This method starts with a reasonable guess of the crystallographic structure of the investigated sample. In this case, it was assumed that the sample has an fcc structure, because Cu, $Fe_{50}Mn_{50}$, and $Ni_{81}Fe_{19}$ all grow fcc as bulk materials with only slightly different lattice constants.

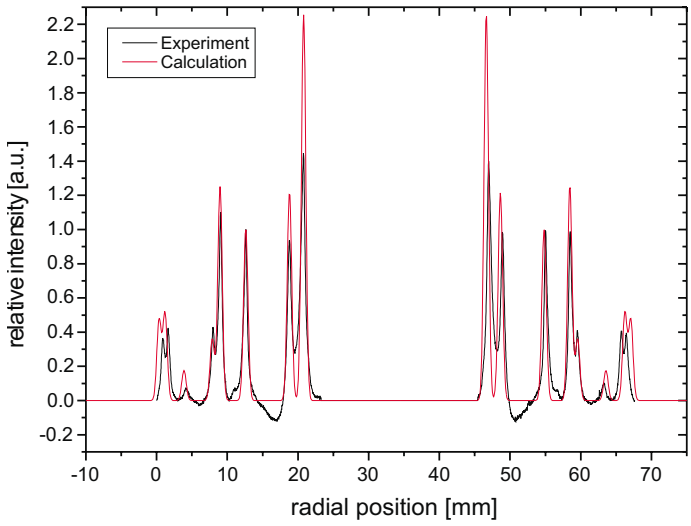

Fig. 5: Comparison between the calculation and the experimental data. The suspected fcc structure is fairly well reproduced.

A result is depicted in Fig. 5. The sample shows a fcc structure. The positions of the outermost peaks are slightly shifted, and these peaks are also slightly broadened and thus reduced in intensity. This can be explained as a result of the fact that there is no uniform lattice constant present within the investigated layer system but a distribution of lattice constants which are all of similar value. Moreover, the innermost peak is not well reproduced due to saturation effects of the recording film.

No experimental peak exceeds its theoretically predicted value, which means that there is no texture present in the investigated sample. This can be confirmed by tilting the sample within the electron microscope setup and thus scanning all possible spatial directions. It was found that the diffraction images do not change their properties with increasing tilt angles.

As the most important result it was found that irradiation with He^+ ions does not change the structure for the investigated dose regime within the sensitivity of the characterization.

References

[1] S. Poppe, Modifikation des Austausch-Verschiebungseffektes in Ferro-/Antiferromagnet-Bilagen durch lagenweise und ortsaufgelöste Ionenbestrahlung, Dissertation, TU Kaiserslautern (2003).
[2] A. Mougin, T. Mewes, M. Jung, D. Engel, A. Ehresmann, H. Schmoranzer, J. Fassbender, B. Hillebrands Phys. Rev. B **63**, 060409(R) (2001).
[3] J. Juraszek, J. Fassbender, S. Poppe, T. Mewes, B. Hillebrands, D. Engel, A. Kronenberger, A. Ehresmann, H. Schmoranzer J. Appl. Phys. **91**, 6896 (2002).
[4] T. Mewes, Systematik epitaktischer Austausch-Verschiebungsschichtsysteme, Dissertation, TU Kaiserslautern (2002).

6.13 Modification of the magnetic properties of the polycrystalline $Ni_{81}Fe_{19}/Fe_{50}Mn_{50}$ exchange bias bilayer system by Ga^+-ion irradiation

S. Blomeier, J. Fassbender, and B. Hillebrands[1]

The results presented here have been obtained during and following a stay of Steffen Blomeier in the group of Prof. J. Chapman at the University of Glasgow. For the analysis of the magnetic properties of the investigated layer system Lorentz microscopy studies were carried out there. Also access was provided to the local focused ion beam machine for Ga ion irradiation.

Recently it has been shown that the exchange bias effect in the polycrystalline $Ni_{81}Fe_{19}/Fe_{50}Mn_{50}$ exchange bias system, as well as in similar systems, can be modified by means of He^+-ion irradiation, as discussed in detail in [1, 2]. Both an enhancement of the exchange bias field as well as a reversal of the bias direction has been found. It is of large interest, whether such behavior can also be achieved by using ions of larger mass and kinetic energy. Subject of this study are irradiation experiments using 30 keV Ga^+-ions provided by a focused ion beam machine.

For $5-10$ keV He^+-ions the obtained dose dependence is well simulated by a model function [1,2]

$$\frac{H_{bias}(N)}{H_{bias,initial}} = (1 \pm aptN)(\exp(-bN)) \quad , \tag{1}$$

which attributes the observed phenomena to the creation of point defects in different regions of the layer system. Here, t describes the thickness of the antiferromagnet, p is an efficiency constant, describing the number of created defects per ion, N is the dose of the ions applied during irradiation, while a and b denote two efficiency parameters for the influence of such point defects on the bias field value. The first factor describes the observed enhancement effects, while the second factor models the decrease of the bias field. While the enhancement effect is attributed to the creation of point defects within the volume of the antiferromagnet, the decrease of the bias field is believed to be a result of the creation of defects at the interface between the ferromagnet and the antiferromagnet. The "+"("-") sign refers to parallel (antiparallel) alignment between the magnetic fields for initialization of the exchange bias effect and the field applied during ion irradiation.

Results on a different system, a sputtered FeCo/IrMn double layer irradiated by 30 keV Ga^+-ions, have been obtained by D. McGrouther at the University of Glasgow. Contrary to our previous results on NiFe/FeMn, he only found a decrease of the bias field strength.

The irradiation was carried out using an FEI Strata 200XP Focused Ion Beam system as a source for 30 keV Ga^+-ions. For this purpose, a special dose test pattern designed by D. McGrouther was applied to a sample which was then subsequently investigated by means of Lorentz microscopy. For this analysis, a Philips CM20 electron microscope with a modified objective lens was used in the Fresnel mode. For this purpose, a special electron-transparent window substrate was used and the deposition of the exchange bias system was carried out in a UHV MBE system (see Chapter 6.12).

[1] In collaboration with D. McGrouther, S. McVitie and J. Chapman, Department of Physics and Astronomy, University of Glasgow, Glasgow, United Kingdom.

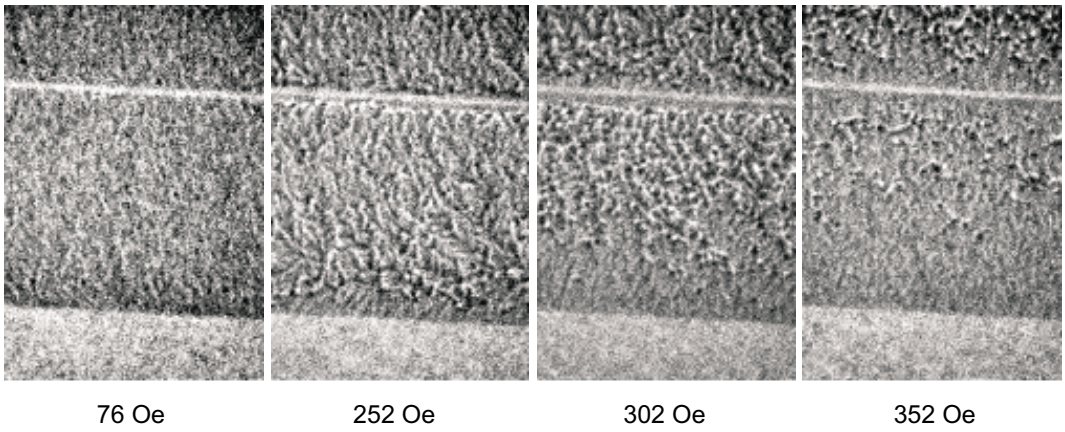

Fig. 1: Fresnel images from the non-irradiated rectangle of the dose test pattern at different values of the applied external field, showing a magnetic reversal process. The applied field is indicated.

The dose test pattern mentioned above consists of nine adjacent rectangles that are $10 \times 400\,\mu m^2$ in size. Each rectangular region was irradiated with a different ion dose in the range $(0-5) \cdot 10^{15}\,ions/cm^2$. The rectangles are separated by thin lines which were irradiated by a dose of $1.25 \cdot 10^{16}\,ions/cm^2$.

Fresnel images were taken from each of those rectangles that still exhibited a magnetic contrast after irradiation. For each such region, a complete hysteresis loop in steps of $25-50\,Oe$ was recorded. Figure 1 shows a series of these Fresnel images from the non-irradiated region of the dose test pattern at different values of the applied external field.

From these images, values for H_c^{left} and H_c^{right}, the left and right coercive fields of each loop, were extracted, and from these values the respective bias fields and coercivity values were calculated. Figure 2 shows the dependence of the bias field and the coercivity of the ion dose, respectively. No enhancement for the bias-field is found for this layer system. The bias field value instead decays exponentially, as modelled by the second factor in Eq. (1).

An exponential fit of the data for the bias field dependency yielded a parameter value of $b = 6.0299 \cdot 10^{-15}\,cm^2$, while the parameter a was set to a value of zero. This value was used to plot the same exponential decay function into the diagram of the experimental data for the coercivity.

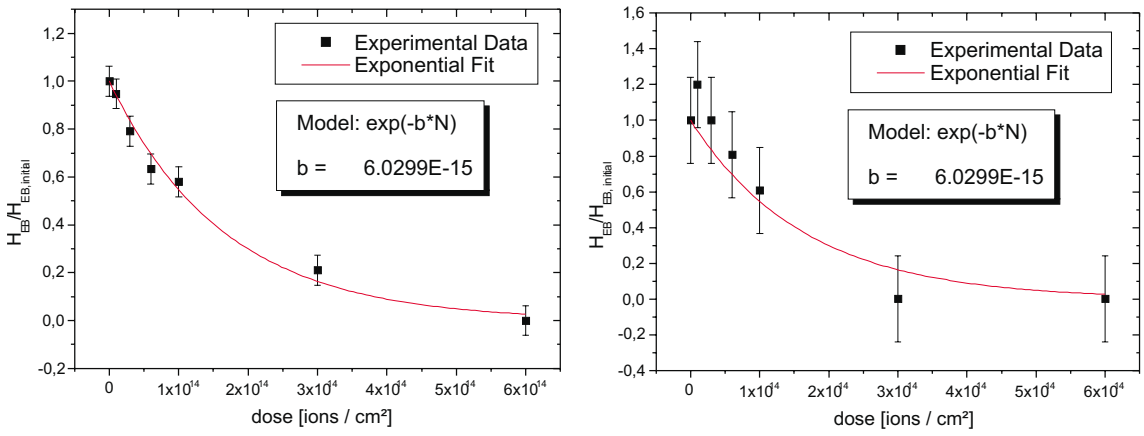

Fig. 2: Dependence of the bias field and the coercivity from the Ga^+-ion dose. The data of the bias field was fitted with a model function, which is plotted in both diagrams.

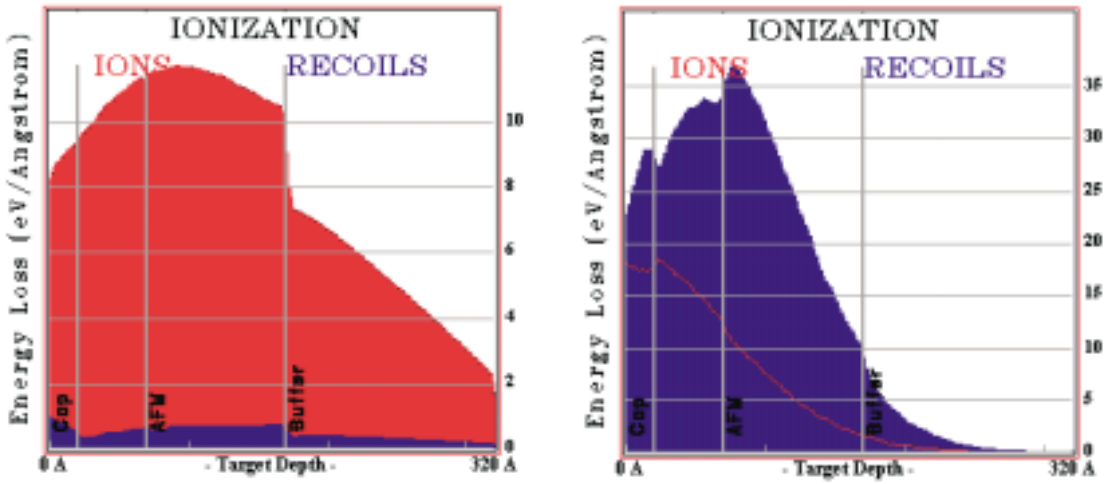

Fig. 3: Energy losses of the ions as a function of the penetration depth in units of Ångstrøm. The left diagram shows the energy losses for the 5 keV He^+-ions, while the right diagram shows them for the 30 keV Ga^+-ions.

It is obtained that the coercivity exhibits a behavior which is very similar to that of the bias field. Moreover, one can conclude from Fig. 2 that the enhancement of the bias field in this system for the irradiation with 5 keV He^+-ions is an ion-specific effect.

To investigate these phenomena further, TRIM-simulations have been performed, using a numerical simulation program written by Ziegler, Biersack and Littmark [3]. The irradiation of the investigated layer system with 5 keV He^+-ions and 30 keV Ga^+-ions was simulated. Figures 3 and 4 show some of the results of this simulation.

A notable difference between the two irradiation procedures is observed. In the case of He^+-ions the main channel for energy loss is the ionization of the target atoms, while in the case of Ga^+-ions most of the ion energy is lost due to dislocation of the target atoms. A plot of the defects created in the target material shows a maximum in the region of the ferromagnet-antiferromagnet interface in case of gallium, while for helium the creation of defects is more uniform. A special plot of this interface shows that the intermixing, i.e. the dislocation of Ni atoms into the antiferromagnet

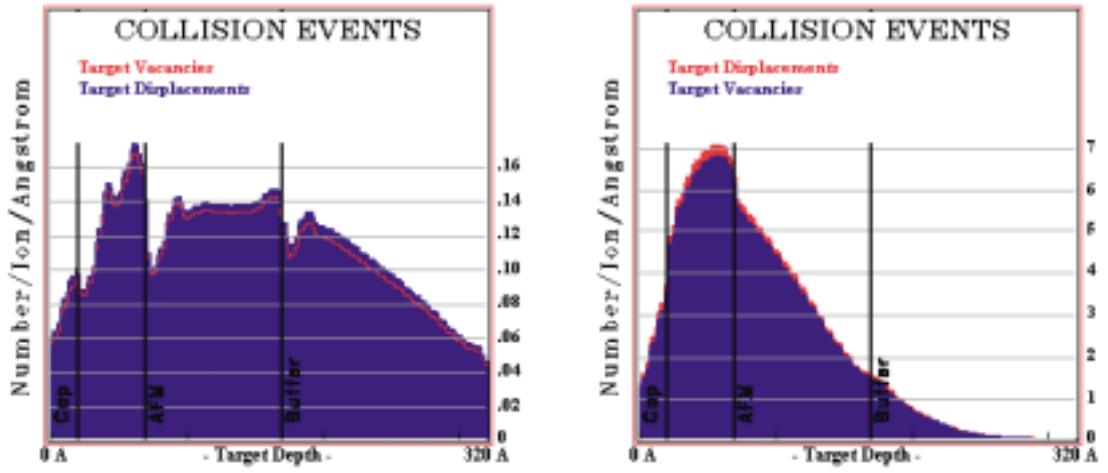

Fig. 4: Defects created during irradiation per ion as a function of the penetration depth in units of Ångstrøm. The left diagram shows the defects created by 5 keV He^+-ions, while the right diagram shows them for 30 keV Ga^+-ions.

and the dislocation of Mn atoms into the ferromagnet, is considerably higher for the same dose of gallium than for helium, approximately by a factor of 40. This is consistent with the result that a comparable decrease of the bias field for the irradiation with Ga^+-ions occurs at doses which are approximately 60 times lower than in the case of He^+-ion irradiation.

In summary, it is obtained that the irradiation with Ga^+-ions is much more efficient in the creation of defects than the irradiation with He^+-ions, and in the case of gallium those defects are primarily created in the interface region between ferromagnet and antiferromagnet. These results support the model outlined above, which attributes a reduction of the bias field to the creation of defects within this interface region.

References

[1] S. Poppe, Modifikation des Austausch-Verschiebungseffektes in Ferro-/Antiferromagnet-Bilagen durch lagenweise und ortsaufgelöste Ionenbestrahlung, Dissertation, TU Kaiserslautern (2003).
[2] J. Juraszek, J. Fassbender, S. Poppe, T. Mewes, B. Hillebrands, D. Engel, A. Kronenberger, A. Ehresmann, H. Schmoranzer J. Appl. Phys. **91**, 6896 (2002).
[3] J.F. Ziegler, J.F. Biersack, J.P. Littmark, The Stopping and Range of Ions in Solids: Pergamon, New York (1985).

E. Elastic Properties

6.14 Growth dynamics in sputtered BN films revealed by Brillouin light scattering

T. Wittkowski, K. Jung, and B. Hillebrands[1]

Boron nitride (BN) in its cubic crystallographic modification is superior to diamond in many aspects concerning electronic and wear protective applications. The understanding of the mechanisms, which lead to the growth of cubic BN thin films, is a worldwide subject of investigation [1]. For the deposition on almost all substrate materials the initially developing sp^2-bonded BN layer at the substrate interface, which may possess a thickness of a few tens of nanometers, plays a key role for the nucleation of the cubic phase and for the elastic properties of the layered film system as a whole. The aim of this project is to reveal the microstructure of specially prepared hexagonal boron nitride (h-BN) films by Brillouin light scattering (BLS) and HRTEM as analytical methods.

Films were deposited by r.f. magnetron sputtering of an h-BN target after sputter cleaning the Si(001) substrate. The substrate temperature was 350 °C. The 4" magnetron was operated at 13.56 MHz with an r.f. power of 800 W. The working gas pressure was 0.2 Pa with a gas flow ratio of $Ar/N_2 = 97/3$, leading to stoichiometric BN films [2]. The electric potential of the substrate was kept at 0 V during the deposition like the chamber walls. Films of different thicknesses were produced by variation of the deposition time in several deposition runs under identical conditions.

BLS investigations were carried out in 180 °-backscattering geometry in (p − ps)-polarization at room temperature [3]. The light power at the sample surface was 120 mW; a collecting lens of numeric aperture 1.7 was used. For surface excitations the relations for the parallel phonon wavevector and the energy are as in Sect. 6.15.

The propagation of acoustic waves in thin films is described within the framework of elastic continuum theory. For a single thin film on a substrate, acoustic modes are guided in the film material if

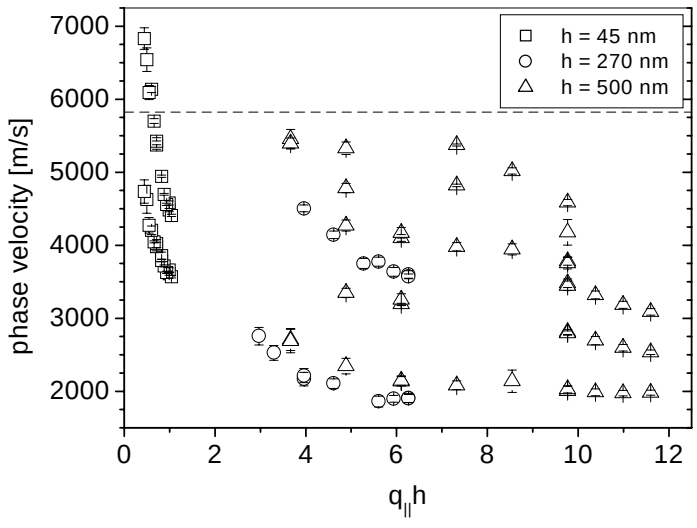

Fig. 1: Dispersion of the phase velocity of vertically polarized surface phonons, guided in the h-BN films. The diagram shows the combined experimental data of three films of different thickness h. The parallel phonon wavevector $q_{||}$ was varied by the angle of light incidence for each film. Pronounced discontinuities in the sound velocities of films of different thickness and identical mode order are observed. This effect is apparent for $q_{||} \cdot h \approx 6$. The dashed line indicates the cut-off velocity of the silicon substrate.

[1] In collaboration with T. Pfeifer, I. Hermann, and F. Richter, Institut für Physik, TU Chemnitz, Chemnitz, Germany, and T. Chudoba, ASMEC Advanced Surface Mechanics, Dresden, Germany.

their sound velocities are smaller than that of the substrate, as is the case for the investigated h-BN films. If the film thickness is in the range of the surface phonon wavelength or smaller, the phase velocity of the guided modes is dispersed. The velocities of the dispersion curves depend on the material parameters and on the dimensionless product of the surface phonon wavevector $q_{\|}$ and the film thickness h [4]. Film elastic properties are described by so-called effective elastic constants since in the measurement microscopic film properties, applying to each of the h-BN nanocrystallites, are averaged over a sufficiently large lateral extension of at least the phonon wavelength (varied from 0.27 to 0.8 µm). In order to describe film texture and possible growth structures by the effective elastic constants, it is necessary to assume a hexagonal symmetry of the film with the c-axis parallel to the film normal. Solutions of the equation of motion with vertical and longitudinal displacement components (Rayleigh mode and Sezawa modes) decouple from solutions with shear-horizontal components for such a film on a (001) substrate. In consequence the description of the vertically polarized modes requires only four independent components of the stiffness tensor, which are c_{11}, c_{13}, c_{33}, c_{55}, and the mass density [4].

Figure 1 shows the experimentally determined dispersion of three h-BN films of different thickness. As was pointed out above, the dispersion of surface acoustic modes should be plotted as continuous curves, these being functions of $q_{\|} \cdot h$. However, if the film material alters its microstructure as a function of the distance from the interface, the dispersion depends on $q_{\|}$ and h independently. This results in discontinuities in the velocity dispersion of films of different thickness for identical values of $q_{\|} \cdot h$. Such a behavior is evidenced by the experimental data shown in Fig. 1. In consequence it must be concluded that the investigated h-BN films change their microstructure with growing film thickness. These findings are corroborated by a HRTEM analysis from the film cross section. As can be seen in Fig. 2 the nanocrystalline material alters its crystallite orientation distribution function in dependence of the distance from the interface drastically. The film grows with a strict fibre texture up to thickness of a few 10 nm. In the further growth the texture becomes weaker until it is completely lost. Films of thickness 200 nm or more are essentially not textured, i.e. their crystallite orientation distribution function is a constant.

For this type of films, characterized by a texture gradient, it is impossible to specify a single set of elastic constants which describes properly the stiffness for all samples independent of their thickness [5]. Nevertheless the rich experimental data base can be evaluated quantitatively. For this purpose the measured dispersion is fitted by solving the equation of motion numerically with the stiffness constants of the film as free parameters. Figure 3 shows an enlarged clipping of Fig. 1 containing experimental data and calculated velocity dispersion curves which represent the least squares fitting result. Error bars of the individual measurements are taken into account by using weights in the computation of the χ^2-sum. The selected experimental velocities, which were used for the fit, correspond to the short-wavelength surface phonons and to the Rayleigh mode of the 500 nm thick film. Thus the obtained elastic constants describe the film stiffness at the surface rather than at the interface. The fitting result is $c_{11} = 37.1 \pm 3.2$ GPa, $c_{33} = 59.7 \pm 3.4$ GPa, and $c_{55} = 6.5 \pm 0.2$ GPa with $c_{13} = 24.0$ GPa and $\rho = 1.61\,\mathrm{g/cm^3}$. Since c_{13} is correlated with the other parameters, it was calculated from the other constants in each iterating step of the fit procedure using the relation $2c_{55}/(c_{11} - c_{13}) = 1$ (i.e. elastic isotropy). The χ^2-sum is little affected by the value of c_{13}. Fixing the constant c_{55} at the above value and fitting the mass density yields $\rho = 1.61 \pm 0.05\,\mathrm{g/cm^3}$ in agreement with the result of an independent determination by X-ray reflectometry. The χ^2-sum divided by the number of degrees of freedom is 1.60 thus documenting a fair reliability of the fit. However, systematic errors arising from uncertainties in the film thickness determination and from the finite aperture size of the collecting lens limit the accuracy of the deduced constants to ±5 %.

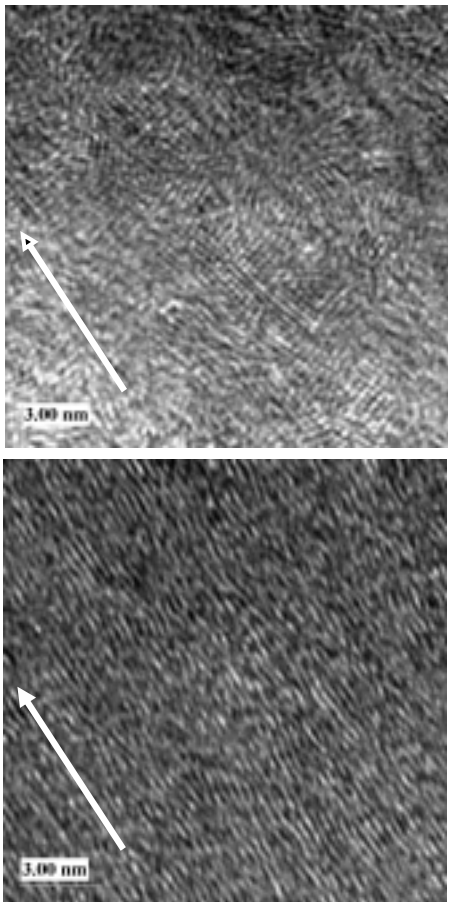

Fig. 2: HRTEM micrographs of the cross section of a thick h-BN film. The lower graph shows the microstructure at a distance of 50 nm from the interface. The pronounced fibre texture is characterized by the crystallite c-axes lying in the film plane. The upper graph shows the microstructure at a distance of 400 nm from the interface. The h-BN crystallites are a few nanometers in diameter and are randomly oriented. The arrows indicate the direction of the film normal.

In order to investigate the variation of film stiffness as a function of the distance from the interface quantitatively, the combined experimental data shown in Fig. 1 of all three films are fitted in order to obtain a set of elastic constants which describe the stiffness of these films as a whole. Data points for which the assignment to the correct mode order was ambiguous were omitted. The remaining data set consisting of 74 data points is still particularly large. It must be noted, however, that the reliability of this fit result is rather poor due to the failure of the model which treats the films as an effective medium for acoustic wave propagation, and thus assumes that the film properties, as a function of the distance from the interface, are constant. Transferring the constant $c_{13} = 24.0\,\mathrm{GPa}$ and $\rho = 1.61\,\mathrm{g/cm^3}$ from the afore obtained fit result, a reduction of c_{11} and c_{55} and an increase of c_{33} is obtained from the combined data of all samples. These results provide an indication of how the effective stiffness of this type of h-BN films changes with thickness.

Apparently the elastic anisotropy, which is expressed by the anisotropy factor $A = c_{11}/c_{33}$, is smaller than 1. The fit result of the 500 nm thick films yields $A = 0.62$, whereas for all three films combined the anisotropy is even more pronounced. In earlier studies it was shown that the anisotropy in this type of film is caused by the texture and has its origin in the enormous anisotropy of the h-BN single crystal [6]. The anisotropy weakening of the thickest sample is in full agreement with the thickness dependent variation of the microstructure as revealed by TEM in Fig. 2. It is concluded that the thicker these films are, the more justified is their treatment as elastically isotropic.

The Young's modulus E parallel to the film normal is calculated from the elastic constants. We set $c_{12} = c_{13}$ and regard that $c_{11} > |c_{12}|$. From the fit of the thickest sample it follows that $E = 41 \pm 5\,\mathrm{GPa}$. Using the combined data of all samples one obtains an even higher modulus.

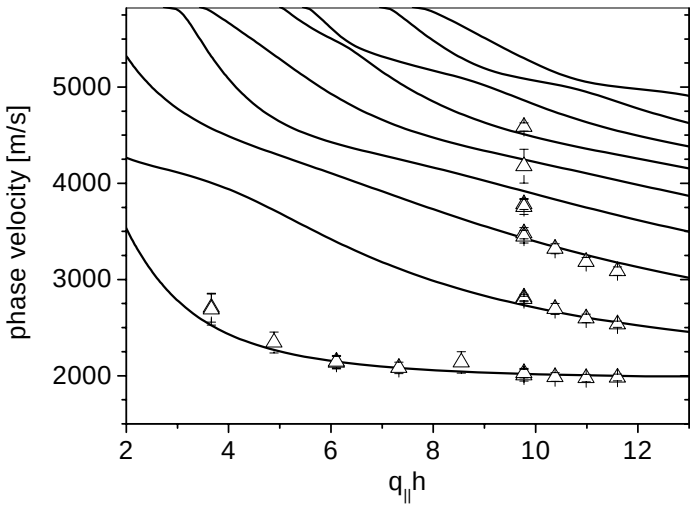

Fig. 3: Dispersion of the Rayleigh mode and the Sezawa modes of a 500 nm thick h-BN film in the discrete part of the mode spectrum. Experimental data (triangles) corresponding to surface phonons with wavevectors $q_{\parallel} > 1.95 \cdot 10^5\,\mathrm{cm}^{-1}$ and of the Rayleigh mode are used for a least squares fit of the film elastic constants. The lines show the best fit result.

In summary this study points out the high sensitivity of the phase velocity of guided acoustic modes on the microstructure of layered structures, measured by BLS. As was shown for h-BN films, small alterations, mainly in the film texture, clearly show up as discontinuities in the combined velocity dispersion curves of differently thick films. Thus BLS from surface phonons in the GHz frequency range allows for a quantitative insight into the effective elastic behavior of thin films as a function of the distance from the interface. These results are in agreement with those of an independent technique using a spherical indenter [7]. The combination with the findings of several other analytical techniques such as TEM and X-ray reflectivity yields a self-consistent description of elastic and microstructural film properties.

Support by the Deutsche Forschungsgemeinschaft is gratefully acknowledged.

References

[1] X.W. Zhang, H.G. Boyen, N. Deyneka, P. Ziemann, F. Banhart, M. Schreck, Nature Mat. Lett. **2**, 312 (2003).
[2] J. Hahn, F. Richter, R. Pintaske, M. Röder, E. Schneider, T. Welzel, Surf. Coat. Technol. **92**, 129 (1997).
[3] B. Hillebrands, Rev. Sci. Instrum. **70**, 1589 (1999).
[4] G.W. Farnell, E.L. Adler, in Physical Acoustics, Vol. **9**, edited by W.P. Mason and R.N. Thurston (Academic, New York, 1972), pp. 35-127.
[5] T. Wittkowski, V. Wiehn, J. Jorzick, K. Jung, B. Hillebrands, Thin Solid Films **368**, 216 (2000).
[6] T. Wittkowski, P. Cortina, J. Jorzick, K. Jung, B. Hillebrands, Diam. Rel. Mat. **9**, 1957 (2000).
[7] T. Chudoba, N. Schwarzer, F. Richter, Surf. Coat. Technol. **127**, 9 (2000).

6.15 Evidence of surface phonons in mesoscopic BN coated fibres

T. Wittkowski, K. Jung, and B. Hillebrands[1]

The reinforcement effects of fibres in metal or ceramic matrix composites are widely influenced by suitable coatings. The aim is to facilitate an optimized fibre/matrix adhesion as well as sliding of fibres in the matrix under mechanical load. Moreover such coatings might serve as a diffusion barrier protecting fibres against oxidation and other corrosion processes. In this report, a boron nitride coating is used as a promising alternative to pyrolytic carbon due to its graphite-like structure, allowing for good fibre/matrix sliding properties and excellent oxidation resistance.

The investigated fibres are of 5 microns in diameter and thus in a mesoscopic region of size. They are of dimensions which are between those of other objects of cylindrical symmetry studied so far by light scattering [1, 2]. The observation of surface acoustic excitations provides insight into their elastic properties, and, in particular, allows one to measure the thickness, the mass density and the elastic properties of thin film coatings deposited on bundles of fibres. The non-destructive measurement of such properties seemed to be impossible up to now. Here we report the successful elastic characterization of such structures.

Carbon fibres T 800 from "TORAYCA" were employed consisting of 6000 filaments - each 5 µm in diameter, density $1.81\,\mathrm{g/cm^3}$, tensile modulus 295 GPa. The fibres have been coated with BN in a continuous process via an isothermal chemical vapor deposition process in a vertical hot wall reactor at 1100 °C under atmospheric pressure [3]. The composition of the BN films deposited onto silicon wafers under analogous conditions was measured by wavelength dispersive X-ray spectroscopy (EPMA, CAMECA SX 100). The N/B ratio was found almost stoichiometric or somewhat greater than 1. The density of the deposits was measured in a mixture of 1,2-dibromethan and aceton using the sink-float method for both coating pieces cracked off the reactor wall and coated fibres compared with uncoated ones. The values spread in the range of $\rho^{film} = 1.88 \pm 0.02\,\mathrm{g/cm^3}$. In comparison to the specifications provided by the manufacturer the density of the uncoated fibres has also been measured yielding $\rho^{fibre} = 1.809 \pm 0.001\,\mathrm{g/cm^3}$. Transmission electron microscopy studies (HREM diffraction) were performed using a 200 kV HITACHI H-8100. HREM images of cross sections reveal the hexagonal turbostratic structure of the BN layer. The observed high structural perfection is limited to small volumes forming nanocrystals or cellular structures of only

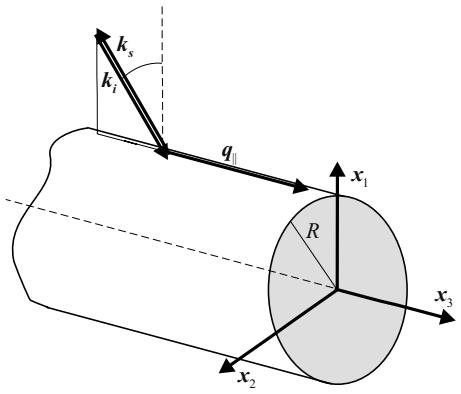

Fig. 1: Sample coordinate system and scheme of the scattering geometry. $\mathbf{k}_i$ and $\mathbf{k}_s$ are the wavevectors of the incident and the scattered light, $\mathbf{q}_\parallel$ is the parallel phonon wavevector in a Stokes process. The scattering plane is defined by the $\hat{x}_1$ and the $\hat{x}_3$-axis in the Cartesian sample coordinate system. The detected parallel phonon wavevector is selected by the angle of incidence θ. The fibre radius R is up to 10 times larger than the wavelength of the acoustic excitations.

[1] In collaboration with S. Stöckel, K. Weise, and G. Marx, Institut für Chemie, Physikalische Chemie, TU Chemnitz, Straße der Nationen 62, D-09107 Chemnitz.

some nanometers in diameter. These nanocrystals consisting of aligned (002) BN hexring sheets are commonly oriented more or less randomly, apart from the very first lattice planes at the carbon interface where the hexagonal planes are oriented parallel to the fibre surface. The TEM analysis also yielded the film thickness of some of the outermost fibres of the bundle. By additional determination of the mass difference of the coated and the uncoated fibres the film thickness on the outer bundle fibres was found to be $h = 80 \pm 15\,\mathrm{nm}$.

BLS experiments were performed with the fibre axes lying in the sagittal plane. A special sample holder was developed which guarantees that all fibres of a bundle were fixed parallel to each other. The achieved fibre alignment was accurate within a margin of $\pm 5^\circ$ for the uncoated carbon fibres and somewhat lower for the BN coated fibres. Figure 1 provides a schematic diagram of the scattering geometry. The scattering plane contains the $\hat{x}_1$- and the $\hat{x}_3$-axis in the sample coordinate system. The fibre length is infinite in comparison with the mean free phonon path which is in the order of a few microns. The fibre radius R is $2.5\,\mu\mathrm{m}$ so that $Rq_\parallel > 2\pi$; $q_\parallel$ denotes the phonon wavevector parallel to the fibre axis.

1. Results on carbon fibres

A strictly linear behavior of the phonon frequency as a function of $\sin\theta$ is observed which proves that the phonon wavevectors involved in the scattering process are parallel to the $\hat{x}_3$-axis. Since no elastic boundary conditions exist for the $\hat{x}_3$-direction, wavevector conservation is valid for the parallel component yielding

$$q_\parallel = 2k_i \sin\theta \quad . \tag{1}$$

With the energy conservation law of the Brillouin process the angular frequency of the associated acoustic excitation of phase velocity v writes

$$\Omega = v \cdot q_\parallel \quad . \tag{2}$$

In a least squares fit the measured phase velocity is determined to $v = 2840 \pm 10\,\mathrm{m/s}$ from the slope of the data points.

Since the fibre diameter is several times larger than the acoustic wavelength, the fibre geometry does not impose strict boundary conditions in the continuum mechanical description of phonon states. In addition the opacity of the graphitic material confines the interaction of light with phonons to a near-surface region of the fibres. Consequently the observed excitation is identified with the Rayleigh surface mode which is detected due to the corrugation of the fibre surface. Up to now the Rayleigh mode of graphite has been observed only for planar sample geometries [5–7].

In order to relate the measured phonon frequencies with the elastic properties, each fibre is treated as an effective medium possessing hexagonal symmetry concerning its acoustical properties; the $\hat{x}_3$-fibre axis is oriented parallel to the hexagonal c-axis. This provides for a different elastic behavior parallel and perpendicular to the fibre axis. Due to the production process it is expected that the stiffness in direction of the axis is much higher than in perpendicular directions. In order to obtain such properties, which also lead to a high tensile strength, fibres were strained and annealed in the final production steps. The hexagonal symmetry describes the elastic properties to be identical in all directions perpendicular to the fibre axis. It is noted that the measured effective hexagonal symmetry is not directly related to the orientation distribution function of graphitic crystallites possibly present in the fibres.

Results are discussed in the limit of a planar geometry where $Rq_\parallel \gg 2\pi$, so that the fibre material forms an infinite halfspace for the Rayleigh mode. For the sample frame of reference (see Fig. 1)

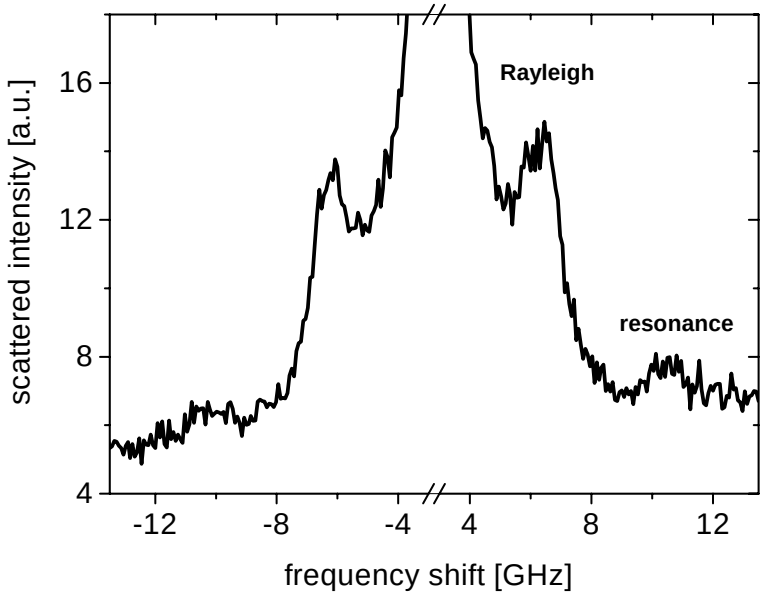

Fig. 2: Brillouin spectrum of carbon fibres coated with 80 nm h-BN. The angle of incidence is $\theta = 58.2^\circ$ with the scattering plane containing the fibre axis. A broad resonance in the continuous part of the spectrum shows up at ± 10.5 GHz. The Rayleigh mode is the dominant feature in all measured spectra. The central peak, which is due to elastically scattered light, has been removed for clarity.

the surface solution of the equation of motion under the elastic boundary conditions of the free surface is obtained from the solution propagating on the basal plane. The stiffness tensor, however, has to be rotated in order to account for the transformation from the sample into the laboratory frame of reference. The Rayleigh velocity v_R is obtained from the real positive root of an implicit cubic equation in v_R^2. It depends on the mass density as well as on the elastic constants c_{11}, c_{13}, c_{33}, and $c_{44} = c_{55}$ of the fibre material [4]. As is well known v_R is predominantly determined by the shear modulus c_{55}. This fact has been used in the past, e.g. to deduce the shear modulus of s.c. graphite [5, 6]. An exemplary computation using the known elastic constants of graphite [7, 8] shows that for propagation on a surface in direction of the $\hat{x}_3$-axis $c_{55}/c_R - 1 = 7.7 \cdot 10^{-4}$, with the Rayleigh velocity $v_R = \sqrt{c_R/\rho}$ and $v_{T_{1,2}} = \sqrt{c_{55}/\rho}$. The phase velocities $v_{T_{1,2}}$ of the two transverse bulk branches degenerate for this particular direction, ρ denotes the mass density.

With $v_R^{fibre} = 2840\,\mathrm{m/s}$ the Rayleigh velocity of the fibres is almost a factor of two higher than for a s.c. graphite material ($v_R^{graphite} = 1494\,\mathrm{m/s}$) with the same symmetry properties. Using the mass density of the fibres their shear modulus amounts to $c_{55}^{fibre} \simeq 14.60 \pm 0.11\,\mathrm{GPa}$. For comparison, the shear modulus of s.c. graphite is $c_{55}^{s.c.graphite} \simeq 5.05 \pm 0.35\,\mathrm{GPa}$ [7] and for high-ordered polycrystalline graphite (HOPG), $c_{55}^{HOPG} \simeq 3.25 \pm 0.15\,\mathrm{GPa}$ [6]. The above results reveal a fibre shear stiffness which is between the ones of graphite and those of partially hydrogen containing, amorphous sp^2 -bonded carbon films [9, 10]. It is remarkably lower than the shear moduli found for amorphous tetrahedrally bonded films (ta-C) [11].

2. Results on BN coated carbon fibres

In general the mass density and the stiffness tensor of a film material deposited onto a substrate differs from that of the substrate. As a consequence the velocities of surface acoustic modes show a characteristic dispersion, as long as the film thickness is smaller than the wavelength of the excitations. This is exactly what is observed in the BN coated fibres (Fig. 3). The phase velocity of the Rayleigh mode decreases distinctly with increasing value of $q_\parallel h$, the product of the parallel phonon wavevector and film thickness h. In the limit of $q_\parallel h \to 0$ the phase velocity is that of the Rayleigh velocity of the uncoated fibre, v_R^{fibre}, whereas in the limit of $q_\parallel h \to \infty$ it is the Rayleigh

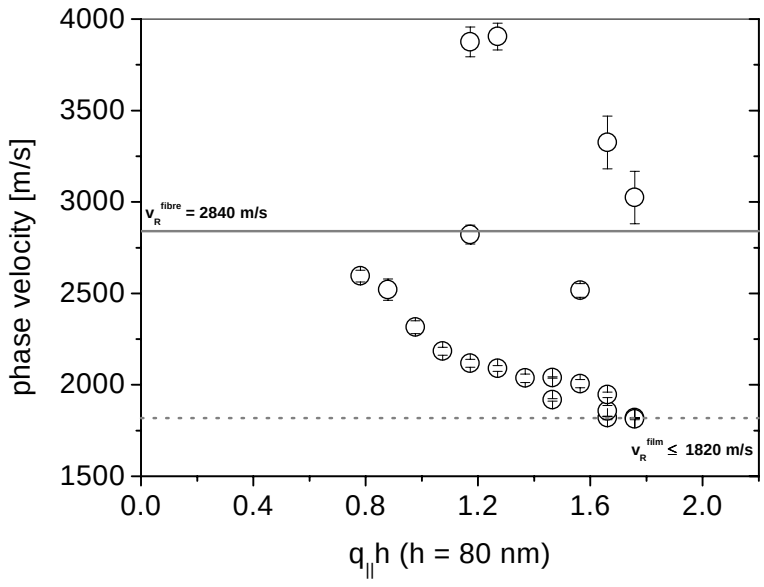

Fig. 3: Phase velocity of surface excitations in BN coated carbon fibres vs. the product of parallel phonon wavevector $q_{\|}$ and BN film thickness h (here $h = 80\,\mathrm{nm}$). The sound velocity of the film is lower than that of the substrate, $v_R^{fibre} = 2840\,\mathrm{m/s}$ (solid line). From the dispersion curve of the lowest mode, the Rayleigh mode, it is seen that $v_R^{film} \leq 1820\,\mathrm{m/s}$ can be used as an upper limit for the Rayleigh velocity of the film (dashed line).

velocity of the film material, v_R^{film}. The presence of an additional higher-order Rayleigh-like mode, a so-called Sezawa mode, is weakly indicated in two spectra. Surface resonances are observed in the continuum of excitations in a few of the experimental spectra, one of which is shown in Fig. 2. The corresponding sound velocities are also shown in the dispersion in Fig. 3. For a few values of $q_{\|}$ the measurement was repeated at different positions on the fibre bundle which gives rise to some scatter in the velocity data. This scatter is partially attributed to an uncertainty in the homogeneity of the fibre orientation during the measurement. It is however predominantly caused by a film thickness which varies for the different fibres in the bundle.

From Fig. 3 it is clear that the lowest measured velocities should make up an upper limit for the Rayleigh velocity of the BN film material. Thus $v_R^{film} \leq 1820\,\mathrm{m/s}$ and, following the discussion for the carbon fibres, $c_{55}^{film} \leq 6.23\,\mathrm{GPa}$ with the mass density of the film, $\rho^{film} = 1.88\,\mathrm{g/cm^3}$. Such a value of the BN shear modulus is in agreement with its s.c. elastic constants which are comparable with those of graphite [12–14]. These findings prove a reduction of the shear modulus in the near-surface region of the coated in comparison to the uncoated fibre by more than a factor of two. This is likely to improve the fibre properties significantly if they are in mechanical contact with each other and with the matrix material in fibre-reinforced composites. The damaging influence of shear stresses at the fibre-matrix interfaces should be reduced by the lubricating effect of the high-temperature resistant BN coating without any reduction of the fibre tensile strength. It is expected that the application of such coated fibre bundles leads to an increased fracture toughness of technically highly relevant composite materials at elevated temperatures.

This is the first time that the BLS technique is applied to analyze elastic properties of fibres which possess a few microns in diameter. These properties are difficult or even impossible to determine with other techniques. BLS does not modify material properties during the measurement and it is absolutely non-destructive. The alteration of near-surface mechanical properties due to the BN film is clearly evidenced and shows the potential of BLS for the characterization of elastic constants, mass density, and the film thickness. A full report is given in [15].

Support by the Deutsche Forschungsgemeinschaft is gratefully acknowledged.

References

[1] J.W. Palko, A. Sayir, S.V. Sinogeikin, W.M. Kriven, and J.D. Bass, J. Am. Ceram. Soc. **85**, 2005-12 (2002).
[2] C.E. Bottani, A. Li Bassi, M.G. Beghi, A. Podesta, P. Milani, A. Zakhidov, R. Baughman, D.A. Walters, and R. E. Smalley, Phys. Rev. B **67**, 155407 (2003).
[3] K. Weise, S. Stöckel, and G. Marx, in Werkstoffwoche; Vol. **98**, edited by W. Dimigen and W. Paatsch (Wiley-VCH, Weinheim, 1999), p. 121-6.
[4] M. J. P. Musgrave, Crystal Acoustics (Holden-Day, San Francisco, Cambridge, London, Amsterdam, 1970).
[5] M. Grimsditch, J. Phys. C (Solid State Physics) **16**, L143-4 (1983).
[6] S.A. Lee and S.M. Lindsay, Phys. Status Solidi (b) **157**, K83 (1990).
[7] M. Grimsditch, Phys. Status Solidi (b) **193**, K9 (1996).
[8] O.L. Blakslee, D.G. Proctor, E.J. Seldin, G.B. Spence, and T. Weng, J. Appl. Phys. **41**, 3373-82 (1970).
[9] T. Wittkowski, V. Wiehn, J. Jorzick, K. Jung, and B. Hillebrands, Thin Solid Films **368**, 216-21 (2000).
[10] X. Jiang, Phys. Rev. B **43**, 2372-7 (1991).
[11] A.C. Ferrari, J. Robertson, M.G. Beghi, C.E. Bottani, R. Ferulano, and R. Pastorelli, Appl. Phys. Lett. **75**, 1893-1895 (1999).
[12] J.F. Green, T.K. Bolland, and J.W. Bolland, J. Chem. Phys. **64**, 656 (1976).
[13] L. Duclaux, B. Nysten, J.-P. Issi, and A.W. Moore, Phys. Rev. B **46**, 3362 (1992).
[14] R.W. Lynch and H.G. Drickamer, J. Chem. Phys. **44**, 181 (1966).
[15] T. Wittkowski, K. Jung, B. Hillebrands, S. Stöckel, K. Weise, and G. Marx, submitted to Anal. Bioanal. Chem. (2003).

6.16 Monte Carlo method to analyze the dispersion of guided acoustic modes

T. Wittkowski, G. Distler, K. Jung, and B. Hillebrands

Surface acoustic waves are of high value for the characterization of elastic and microstructural properties of thin films. The evaluation of the dispersion of guided modes in thin films in the GHz frequency range, as accessible with Brillouin light scattering (BLS), allows for a detailed description of anisotropic film properties. Usually material constants are extracted from a fit procedure in which the elastic constants act as free parameters [1]. For this the sum of squares

$$\chi^2 = \sum_i w_i (v_i^{calculated} - v_i^{measured})^2 \qquad (1)$$

over i measured and calculated velocities, using the weights w_i, is mostly used as the merit function. It is minimized in consequent iteration steps by a deterministic procedure. This technique is well established, it works fast and reliably provided that the assignment to the correct acoustic mode order is clear. For convergence, these algorithms, the Levenberg-Marquardt method being a prominent example, usually need start values for the fit parameters not too far away from the solution corresponding to the minimum sum of squares, χ^2_{min}, without guarantee that the absolute minimum is found. The structure of the parameter space bears additional information about parameter correlation and uniqueness of the found solution. Commonly used deterministic fitting routines assume a normal distribution of the parameters. If this is not fulfilled – a situation which appears quite regularly – confidence limits on parameters computed by using such routines provide only an approximation. We thus adopted an alternative statistical Monte Carlo (MC) technique in order to address some of the above named issues.

The MC procedure shall be described briefly. Starting from the experimental data, new data sets consisting of the same number of data points were generated by a random variation of quintuplets of the free parameters, four independent constants of c_{ij} and ρ, within specified intervals. The number of parameters may be increased or reduced depending on the symmetry properties of the system to be described. Here we consider sagittal modes in a hexagonal symmetry film. The weighted χ^2-sum for each data set was computed according to Eq. (1). The velocities $v_i^{calculated}$ were obtained from the zeros of the boundary condition determinant which contains the components of the elastic tensors and the mass densities of both the film and the substrate, coupled by the

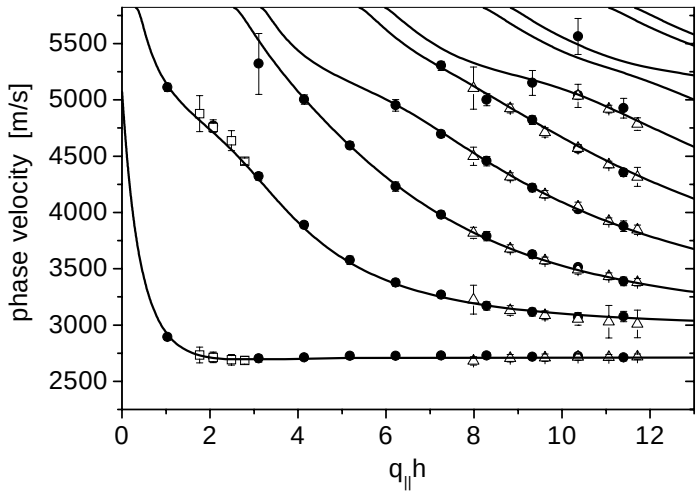

Fig. 1: Phase velocity dispersion curves for the discrete, sagittally polarized surface waves (Rayleigh and Sezawa) as a function of $q_{\|} \cdot h$. The filled circles represent measurements made with a constant $q_{\|}$ value of $17.27\,\mu m^{-1}$ over the complete range of film thickness. For two film steps of thickness 191 nm (open squares) and 595 nm (open triangles) the value of $q_{\|}$ was varied. The lines represent the computed best fit to the experimental data.

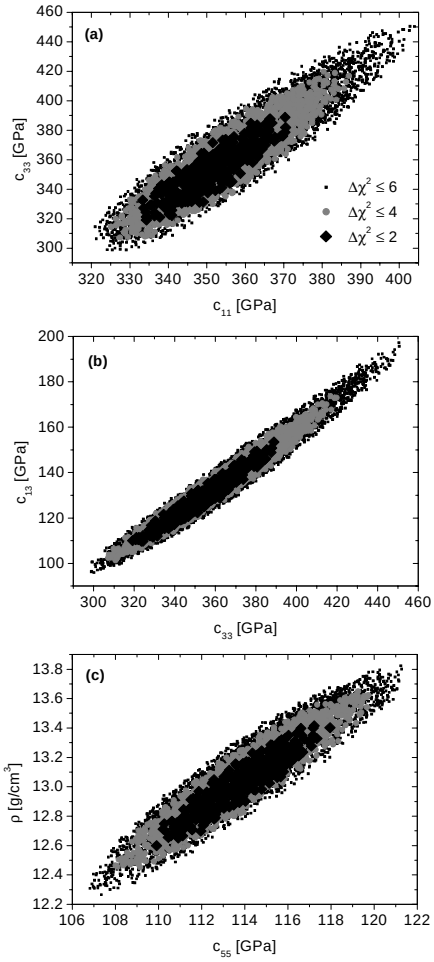

Fig. 2: Projections of the parameter space onto the (c_{11}, c_{33})-, the (c_{33}, c_{13})-, and the (c_{55}, ρ)-plane for the quintuplets of free parameters with χ^2 in the vicinity of χ^2_{min}. The three chosen planes represent the parameter pairs which are most strongly correlated. Projections of different sets of points show areas that are related to different values of $\Delta\chi^2$, where $\Delta\chi^2 = \chi^2 - \chi^2_{min}$. The constant c_{13}, which usually is difficult to determine due to its strong correlation with the other constants, is quantified with fair accuracy.

boundary conditions at the interface

$$\sigma_{3j}^{substrate} = \sigma_{3j}^{film}\Big|_{x_3=0} \qquad \text{and} \qquad u_3^{substrate} = u_3^{film}\Big|_{x_3=0} \tag{2-a}$$

and at the free surface [3]

$$\sigma_{3j}^{film}\Big|_{x_3=h} = 0 \quad . \tag{2-b}$$

The actual set of parameters is retained if the calculated dispersion curves fall – for 68 % of all points of the set in this example – within the error bars of the measured data points. Other parameter sets are discarded. This routine does not require any assignment to the mode order. The analysis was performed on the dispersion of surface acoustic modes in tungsten carbide films on silicon used as a model system [2]. In addition the large velocity dispersion data set allowed the determination of four independent stiffness constants as well as the mass density of the film material by a fitting routine. The measured dispersion is shown in combination with the result of the least squares fit in Fig. 1.

Since the deterministic fitting algorithm converged satisfactorily in determining the minimum in the χ^2-sum, we concentrated our statistical analysis on the parameter space surrounding of the absolute minimum χ^2_{min}. Figures 2 and 3 present the results of $7.5 \cdot 10^8$ randomly chosen and evaluated data sets. Computation time on a modern personal computer with a processing frequency

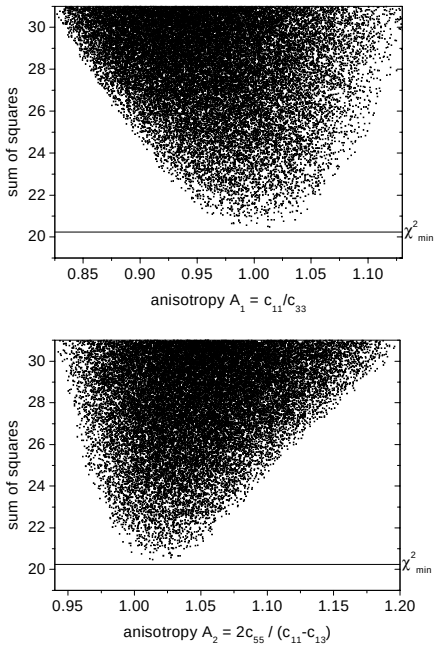

Fig. 3: MC results of the weighted sum of squares for the two anisotropy factors A_1 and A_2 of the film material. Starting from the hexagonal symmetry model, the smallest χ^2-sum clearly corresponds to nearly isotropic parameters for this type of film. The straight line in both diagrams indicates the minimum χ^2-sum that was obtained with the least squares fit.

of 1.8 GHz was approximately one week. The computation can be distributed on several CPUs to shorten this time.

Figure 2a-c shows projections of the parameter space onto the (c_{11}, c_{33})-, the (c_{33}, c_{13})-, and the (c_{55}, ρ)-plane for the free parameter quintuplets with χ^2 in the vicinity of χ^2_{min}. Among the 10 two-dimensional subspaces these three chosen planes represent the parameter pairs which are the most strongly correlated ones. Projections of different sets of points show areas that are related to different values of $\Delta\chi^2$, where $\Delta\chi^2 = \chi^2 - \chi^2_{min}$. These diagrams emphasize the parameter correlation and provide an insight into the structure of the parameter space. A detailed analysis of the probability distribution functions of the individual parameters shows that these are not normally distributed in general so that the results shown in Fig. 2 provide an appropriate presentation of the parameter space for chosen values of $\Delta\chi^2$. Figure 3 shows the MC results of the weighted sum of squares for the two anisotropy factors A_1 and A_2 of the film material. Starting from the hexagonal symmetry model, the smallest χ^2-sum clearly corresponds to nearly isotropic parameters.

In summary the least squares fitting and the MC approach yield self-consistent results on four independent components of the stiffness tensor and the mass density of the tungsten carbide film. Both techniques reveal a near isotropy of the film material by using a hexagonal model. The statistical MC method is well appropriate to determine the absolute and relative minima of a merit function yielding additional information about the often complex structure of a multi-dimensional parameter space. A full report is given in [2].

Support by the Deutsche Forschungsgemeinschaft is gratefully acknowledged.

References

[1] W.H. Press, S.A. Teukolsky, V.T. Vetterling, B.P. Flannery, Numerical recipes, 2nd ed., Cambridge University Press (1992).
[2] T. Wittkowski, G. Distler, K. Jung, B. Hillebrands, J.D. Comins, submitted to Phys. Rev. B (2003).
[3] G.W. Farnell, E.L. Adler, in Physical Acoustics, Vol. **9**, edited by W.P. Mason and R.N. Thurston (Academic, New York, 1972), pp. 35-127.

F. Transfer of Technology

6.17 Mode-locked ps-Nd:YVO_4- laser for time-resolved measurements at wavelengths of 1064 nm, 532 nm and 266 nm

M.C. Weber, H. Nembach, J. Fassbender[1]

In this report we describe our new picosecond laser setup which was developed in collaboration with Lumera Lasers GmbH [1].

Ultra-short laser pulses are a powerful tool for time resolved investigations of magnetic films. The benefits of this method have been demonstrated so far mostly with Ti:Sapphire lasers, which provide pulse durations shorter than hundred femtoseconds and enable the observation of ultrafast processes such as carrier interactions. However, such Ti:sapphire lasers are complex and expensive devices, which are limited in pulse energy. In contrast, picosecond lasers, based on Nd:YVO_4, offer the advantage of direct diode pumping and provide high efficiency and high average power from a robust system. The pulse duration of $\approx 10\,\mathrm{ps}$ provides the right time scale for many experiments, in which the minimum time scale is defined by the duration of magnetic field pulses generated by an electronic pulse generator of $\approx 100\,\mathrm{ps}$ used to excite the magnetic system.

The Nd:YVO_4 laser described here features high pulse energy in the infrared and a subsequent frequency conversion to green and ultraviolet (UV) radiation. Single pulses or pulse trains can be selected with a pulse repetition frequency from single pulses up to 1 MHz. The variety of wavelengths and repetition rates empowers the user to drive several experiments with one laser source. A special feature is the optical generation of trigger pulses with minimum timing jitter.

A scheme of the laser setup is shown in Fig. 1. Pulses are generated at a wavelength of 1064 nm by a passive mode-locked laser oscillator with a duration of 8.5 ps and a pulse repetition frequency (PRF) of 80 MHz. The pulse energy is $E_{laser} > 50\,\mathrm{nJ}$, the average output power is $P_{laser} = 4.3\,\mathrm{W}$. A double-pass amplifier (AMP) maintains a perfect beam quality ($M^2 < 1.1$) and increases the output power to $P_{IR} = 7.5\,\mathrm{W}$ ($E_{IR} = 90\,\mathrm{nJ}$). These pulses are focused into a nonlinear LBO crystal[2]

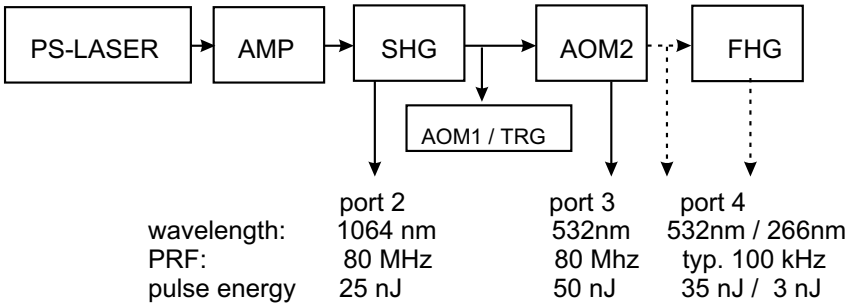

Fig. 1: Scheme of the Nd:YVO_4 laser setup for generation of picosecond pulses in the IR, green, and UV. For the nomenclature see the main text.

[1] in collaboration with R. Knappe, T. Herrmann, B. Henrich, A. Nebel, Lumera Lasers GmbH.

[2] SHG: Lithiumtriborat: LiB_3O_5 (LBO) $T = 150\,^{\circ}\mathrm{C}$, cut $\phi = 0\,^{\circ}$, $\theta = 90\,^{\circ}$.

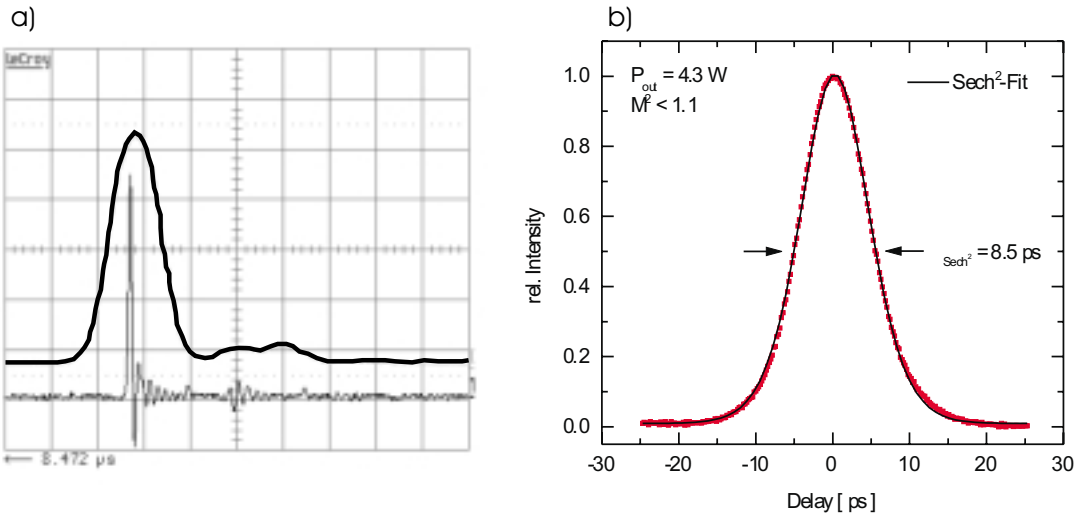

Fig. 2: a) Transmission window (upper line) for a selected laser pulse (lower line), b) Intensity autocorrelation of the IR laser pulses.

to generate the second harmonic (SHG) with a conversion efficiency > 50 percent ($P_{green} = 4\,\mathrm{W}$, $E_{green} = 50\,\mathrm{nJ}$). The residual IR is available with an output power of 2 W (25 nJ). A small portion of the green beam ($\approx 10\,\mathrm{mW}$) is split to generate the trigger signal (TRG). In both laser beams, acousto-optic modulators (AOM) are used as pulse pickers with a tunable pulse repetition frequency. The efficiency of the AOM is ≈ 70 percent and limits the energy of the selected green pulses to 35 nJ. These pulses are frequency-doubled again in a nonlinear crystal[3] and generate the fourth harmonic (FHG) with a wavelength of 266 nm and a pulse energy of $> 3\,\mathrm{nJ}$.

A critical issue for time-resolved measurements is a low-jitter trigger signal. Standard digital delay generators have a typical jitter of $\approx 100\,\mathrm{ps}$ and even sophisticated electronics does not much better than $\approx 10\,\mathrm{ps}$. In contrast, the jitter of mode-locked laser pulses is usually in the order of $\approx 1\,\mathrm{ps}$. To benefit from this precision, the trigger pulses are generated by the laser pulses and a fast photodiode. The two AOMs are driven by a common delay generator (SRG DG 535), which is synchronized to the laser pulse train. Both AOMs are working at the same pulse repetition frequency, but with independently selectable delays for on- and off-switching. So, two windows for laser and trigger are opened, whose jitter does not effect the time interval of the pulses relative to each other. The temporal distance of the windows is tunable in 12.5 ns-steps (that is the time between two pulses @ 80 MHz pulse repetition frequency). The jitter between trigger and signal pulse was measured with a sampling oscilloscope (Tektronix CSA 830) and found to be less than 8 ps, including all electrical noise.

Figure 2a shows a selected laser pulse (lower line) and the transmission window given by the AOM (upper line). The resolution of this measurement is limited by the bandwidth of the oscilloscope (1 GHz) and the rise-time of the photodiode (300 ps). The pulse-duration of 8.5 ps is measured with a background-free intensity autocorrelation, shown in Fig. 2b. Rise- and fall-times as short as 5 ns are required for the transmission window to provide proper single-pulse switching. Such values can only be achieved with cutting edge AOMs that generate small Bragg-zones for visible radiation (e.g. AA.MQ280-vis). The green beam has to be focused to a waist of $< 50\,\mathrm{m}$, that corresponds to a peak power density of $> 3.2\,\mathrm{GW/cm^2}$. Precise alignment and a dust-free environment are premises for the stable operation of this laser system.

[3] FHG: Beta-Bariumborat: β-BaB_2O_4 (BBO).

This work is supported by the Stiftung Rheinland-Pfalz für Innovation.

References

[1] LUMERA LASER GmbH, Opelstrasse 10, D−67661 Kaiserslautern, www.LUMERA-LASER.com, Phone: +496301703180, Fax: +496301703189, Email: info@LUMERA-LASER.com.

6.18 The influence of amorphous carbon coating on encrustations of indwelling catheter surfaces

L. Kleinen, K. Jung, B. Hillebrands[1]

The blockage and encrustation of urethral catheters by crystalline bacterial biofilms remains a major complication in the care of patients undergoing long-term indwelling bladder catheterization. Approximately 25% of all nosocomial infections are related to bladder catheterization. These infections are initiated by microorganisms attaining to the bladder via the catheter. Proliferation of urease-producing bacteria, e.g. Proteus mirabilis, leads to a splitting of urea into ammonia and bicarbonate, and subsequently to a dramatic increase in the urinary pH. The alkaline environment supports the precipitation of phosphate salts which deposit as infection stones on the catheter surface (Fig. 1). Occasionally, the mineral brushite ($CaHPO_4 \cdot 2H_2O$) can be formed at pH levels between 6.5 and 7.2; at higher pH levels it can transform into carbonate apatite.

In this study we investigated the influence of amorphous carbon coating on surfaces of indwelling catheters in respect of its ability to reduce the extent of encrustation.

A 50 nm thick carbon layer was deposited on the catheter surfaces by Plasma Enhanced Chemical Vapour Deposition (PECVD) using a commercially available inductively coupled plasma beam source (COPRA™ , CCR GmbH Rheinbreitbach). This source is characterized by a very effective rf excitation of the plasma. The gas pressure can be chosen very low and the delay time of the gas molecules in the source is short. Therefore predominantly $C_2H_2^+$ or C_2H^+ ions leave the plasma source (Fig. 2). In the deposition process the ion energy and the ion flux are reduced by a factor of ten with respect to the conditions typical for the production of diamond-like carbon films [1]. Thus

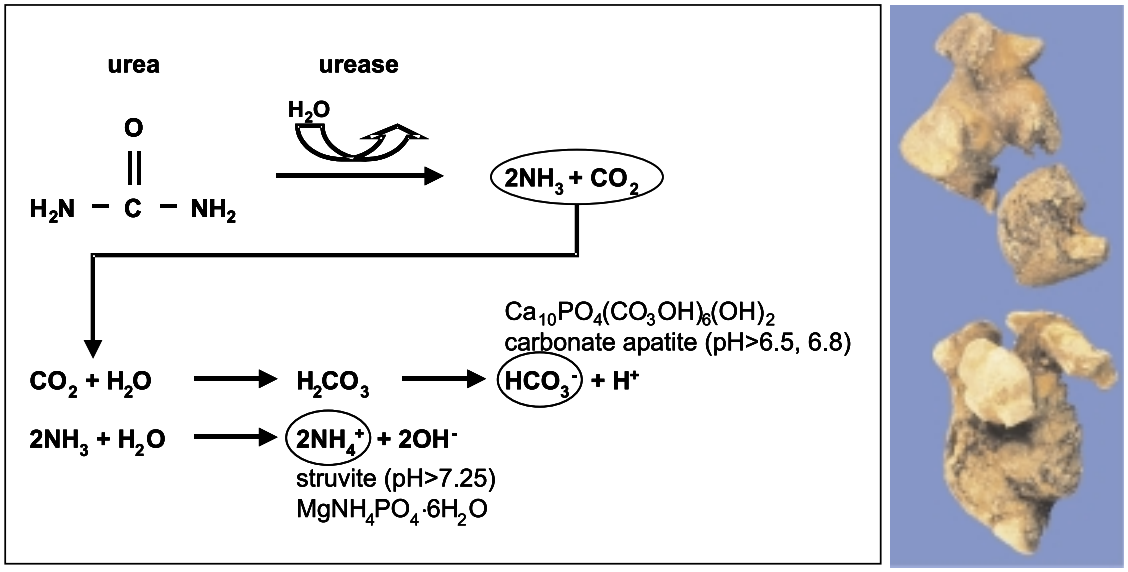

Fig. 1: Reaction scheme of infection stone formation (left). Struvite-carbonate apatite stone which has completely filled the kidney (right).

[1] In collaboration with H. Busch and U. Grabowy, NTTF GmbH Rheinbreitbach, and N. Laube, Department of Urology, Universität Bonn.

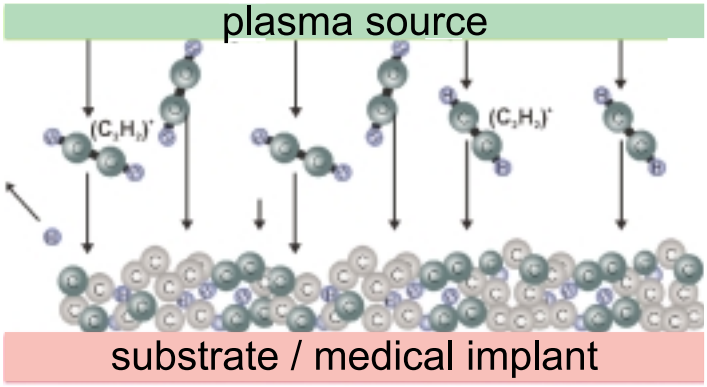

Fig. 2: Scheme of the PECVD-process. Ionized acetylene gas released by the plasma source is deposited as amorphous carbon on the catheter surface.

the energy flux density is reduced by two orders of magnitude. The temperature of the substrate is practically not increased during the deposition process. Therefore this technique qualifies even for coating highly temperature sensitive materials (e.g. polymers) with amorphous carbon. Despite the fact that the impinging ions have only a kinetic energy of 20 eV, the deposited films are rather hard and scratch resistant with respect to steel. The films exhibit a Vickers hardness of $H = 10\,\mathrm{GPa}$ and an elasticity of $E = 60\,\mathrm{GPa}$. The ratio E/H of 6 is in agreement with the constraint model of Angus [2]. That means the carbon films are thermodynamically stable.

For the investigation of the crystallization processes under constant conditions, an in-vitro constant-flow-crystallizer model and a standardized test procedure were developed (Fig. 3). 24 commercial indwelling catheters were incubated in synthetic urine for 12h. Urea-splitting was started by the addition of urease. Encrusted surfaces were analyzed with SEM; the chemical composition and

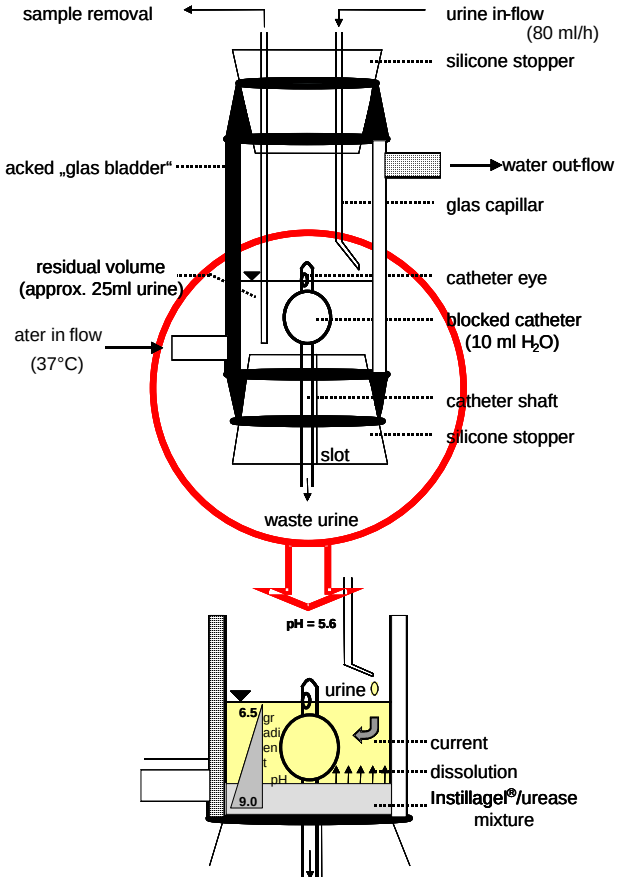

Fig. 3: Schematic view of the glas-bladder-model for standardized investigation of encrustation processes on indwelling catheters (top); detailed view (bottom).

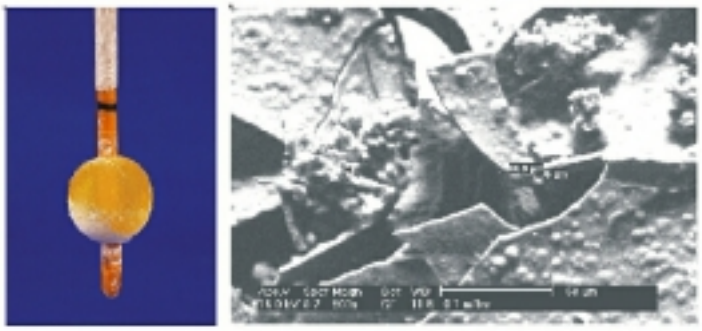

Fig. 4: Encrusted catheter after 12 h incubation (left); SEM picture of mineral deposits on uncoated catheter surface (right).

the amount of the minerals deposited on the catheter surface were determined.

After 12 hours of incubation the catheters (n=24) showed mineral deposits (Fig. 4, left). Encrustation was analyzed with SEM (Fig. 4, right). Crystallized minerals were identified as carbonate apatite, struvite, and brushite. A 50 % decrease of encrustation was found for coated catheters (Fig. 5).

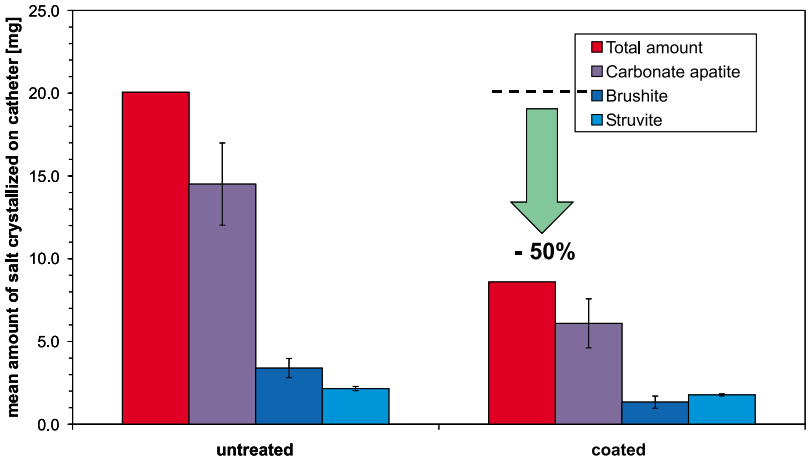

Fig. 5: Mean values of the amounts of stone material precipitated within 12 hours of incubation on the upper 5 cm of the expanded catheters. Different mineral phases are analyzed: apatite (dark grey), brushite (grey), struvite (light grey). Left: uncoated, right: coated.

Therefore carbon coating is a new strategy to improve the surface of indwelling catheters in order to protect them from rapid encrustation. The results of the presented pilot study clearly show that the amout of mineral phases which precipitated on the coated test catheters surfaces can be reduced by 50 % compared to untreated catheters [3]. Further experiments will be performed to understand the mechanisms of this effect, which leads to a broad range of applications. Encrustation reducing thin films also qualify for coatings on uereter stents and other endwelling instruments for the urinary tract.

Work supported by the Stiftung Rheinland-Pfalz für Innovation.

References

[1] R. Kleber, M. Weiler, A. Krüger, S. Sattel, G. Kunz, K. Jung, H. Ehrhardt, Diam. Rel. Mat. **2**, 246 (1993).
[2] J.C. Angus, P. Koidl, S. Domitz, “Carbon Thin Films”, in: Plasma Deposited Thin Films (Eds.: J. Mort, F. Jansen), CRC press, Cleveland (1986).
[3] N. Laube, L. Kleinen, K. Schenk, Management und Krankenhaus, August (2003).

Chapter 7: Publications

Most publications can be downloaded from http://www.physik.uni-kl.de/hillebrands.

7.1 published

1. *Confined dynamicc excitations in structured magnetic media*
   S.O. Demokritov, B. Hillebrands, A.N. Slavin
   IEEE Tran. Mag. **38**, 2502 (2002).

2. *Anisotropy of magneto-optical spectra in ultrathin Fe/Au/Fe bilayers*
   J. Grondilova, M. Rickart, J. Mistrik, K. Postava, S. Visnovsky, T. Yamaguchi, R. Lopusnik, S.O. Demokritov, B. Hillebrands
   J. Appl. Phys. **91**, 8246 (2002).

3. *Ultrafast magnetic switching*
   B. Hillebrands, J. Fassbender
   Nature **418**, 493 (2002).

4. *Effective dipolar boundary conditions for dynamic magnetization in thin magnetic stripes*
   K. Yu. Guslienko, S.O. Demokritov, B. Hillebrands, A.N. Slavin
   Phys. Rev. B **66**, 132402 (2002).

5. *Interlayer interaction in a Fe/Cr/Fe System: Dependence on the thickness of the chrome interlayer and on temperature*
   S.O. Demokritov, A.B. Drovosekov, N.M. Kreines, H. Nembach, M. Rickart, D.J. Kholin
   Journal of Experimental and Theoretical Physics **95**, 1062 (2002).

6. *Temperature dependence of interlayer coupling in Fe/Cr/Fe layered system*
   S. O. Demokritov, A.B. Drovosekov, N.M. Kreines, H. Nembach, M. Rickart, D.I. Kholin, Sov. Phys. JETP **95**, 10621 (2002).

7. *Spin dynamics in confined magnetic structures II*
   B. Hillebrands, K. Ounadjela (Eds)
   Springer, Berlin (2003).

8. *Magnetization dynamics investigated by time-resolved Kerr effect magnetometry*
   J. Fassbender
   in: *Spin dynamics in confined magnetic structures II*, Eds. B. Hillebrands, K. Ounadjela
   Springer, Berlin (2003).

9. *Confined dynamic excitations in structured magnetic media*
   S.O. Demokritov, B. Hillebrands, A.N. Slavin
   IEEE Trans. Magn. **38**, 2502 (2003).

10. *Temperature dependence of interlayer coupling in a Fe/Cr/Fe wedge sample, MOKE and MBLS studies*
    S. O. Demokritov, A.B. Drovosekov, D.I. Kholin, N.M. Kreines
    J. Magn. Magn. Mater. **258-259**, 391 (2003).

11. *Collison properties of quasi-one-dimensional spin wave solitons and two-dimensional spin wave bullets*
A.N. Slavin, O. Büttner, M. Bauer, S.O. Demokritov, B. Hillebrands, M.P. Kostylev, B.A. Kalinikos, V.V. Grimalsky, Yu. Rapoport
Chaos, **13**, 693 (2003).

12. *Coherent precessional magnetization reversal in microscopic magnetic memory elements*
H.W. Schumacher, C. Chappert, P. Crozat, R.C. Sousa, P.P. Freitas, J. Miltat, J. Fassbender, B. Hillebrands
Phys. Rev. Lett. **90**, 017201 (2003).

13. *Control of interlayer exchange coupling in Fe/Cr/Fe trilayers by ion beam irradiation*
S.O. Demokritov, C. Bayer, S. Poppe, M. Rickart, J. Fassbender, B. Hillebrands, D.I. Kholin, N.M. Kreines, O.M. Liedke
Phys. Rev. Lett. **90**, 097201 (2003).

14. *Probing interface magnetism in the FeMn/NiFe exchange bias system using magnetic second-harmonic generation*
L.C. Sampaio, A. Mougin, J. Ferré, P. Georges, A. Brun, H. Bernas, S. Poppe, T. Mewes, J. Fassbender, B. Hillebrands
Europhys. Lett. **63**, 819 (2003).

15. *Ion irradiation of exchange-bias systems for magnetic sensor applications*
J. Fassbender, S. Poppe, T. Mewes, J. Jurszek, B. Hillebrands, D. Engel, M. Jung, A. Ehresmann, H. Schmoranzer, K.U. Barholz, R. Mattheis
Appl. Phys. A **77**, 51 (2003).

16. *Phase diagrams and energy barriers of exchange-biased bilayers with additional anisotropies in the ferromagnet*
T. Mewes, H. Nembach, J. Fassbender, B. Hillebrands, J.V. Kim, R.L. Stamps
Phys. Rev. B **67**, 104422 (2003).

17. *Formation of envelope solitons from parametrically amplified and conjugated spin wave pulses*
A.A. Serga, S.O. Demokritov, B. Hillebrands, A.N. Slavin
J. Appl. Phys. **93**, 8758 (2003).

18. *Phase control of non-adiabatic parametric amplification of spin wave packets*
A.A. Serga, S.O. Demokritov, B. Hillebrands, Seong-Gi Min, A.N. Slavin
J. Appl. Phys. **93**, 8585 (2003).

19. *Spin wave wells with multiple states created in small magnetic elements*
C. Bayer, S.O. Demokritov, B. Hillebrands, A.N. Slavin
Appl. Phys. Lett. **82**, 607 (2003).

20. *Dynamics in magnetic stripes*
B. Hillebrands
Festschrift in honor of Prof. Dr. Gernot Güntherodts 60th anniversary, Aachen, May 2 (2003).

21. *Ultraschnelle magnetische Speicher*
J. Fassbender, B. Hillebrands
Physik in unserer Zeit **34**, 102 (2003).

22. *Parametric generation of soliton-like spinwave packets in active rings based on ferromagnetic films*
A.A. Serga, M. Kostylev, B.A. Kalinikos, S.O. Demokritov, B. Hillebrands, H. Benner
JETP Lett. **77**, 350 (2003).

23. *Amorphe Kohlenstoffschichten, Geeignete Materialien zur Beeinflussung von Katheterenkrustationen*
N. Laube, L. Kleinen, K. Schenk
Management und Krankenhaus, August (2003).

7.2 in press

1. *Brillouin light scattering spectroscopy*
B. Hillebrands
in: Novel techniques for characterizing magnetic materials, Yimey Zhu, editor, Kluwer Academic Press, in press.

2. *Induced four fold anisotropy and bias in compensated NiFe/FeMn double layers*
T. Mewes, B. Hillebrands, R.L. Stamps
Phys. Rev. B, in press.

3. *Experimental observation of symmetry breaking nonlinear modes in an active ring*
S.O. Demokritov, A.A. Serga, V.E. Demidov, B. Hillebrands, M. Kostylev, B.A. Kalinikos
Nature **426**, 159 (2003), in press.

4. *Magnetismus*
B. Hillebrands, S. Blügel
in: Bergmann-Schäfer, Experimentalphysik Band 6 (Festkörper)
de Gruyters Verlag, in press.

7.3 submitted

1. *On the mechanism of irradiation enhanced exchange bias*
S. Poppe, J. Fassbender, B. Hillebrands
submitted to Appl. Phys. Lett..

2. *General methods for the determination of the stiffness tensor and mass density of thin films using Brillouin light scattering: study on tungsten carbide films*
T. Wittkowski, G. Distler, K. Jung, B. Hillebrands, J.D. Comins
submitted to Phys. Rev. B..

3. *Low energetic ion embedding by ECWR plasma, the given production technology to form TMR barriers for MRAM*
W. Maas, J. Langer, B. Ocker, S.O. Demokritov, B. Hillebrands, B.F.P. Roos, M. Weiler
submitted to Vacuum.

4. *Magnetic interlayer coupling across semiconducting EuS layers*
   U. Rücker, S.O. Demokritov, J. Nassar, P. Grünberg
   submitted to Europhys. Lett..

5. *Self-Generation of Two-Dimensional Spin-Wave Bullets*
   A.A. Serga, S.O. Demokritov, B. Hillebrands, A.N. Slavin
   submitted to Phys. Rev. Lett..

6. *Separation of the three magnetization vector components for time-resolved magneto-optic Kerr effect measurements*
   H. Nembach, M.C. Weber, J. Fassbender, B. Hillebrands
   submitted to J. Appl. Phys..

7. *Picosecond optical control of the magnetization in exchange biased NiFe/FeMn bilayers*
   M.C. Weber, H. Nembach, J. Fassbender
   submitted to J. Appl. Phys..

8. *High resolution magnetic patterning of exchange coupled multilayers*
   V.E. Demidov, D.I. Kholin, S.O. Demokritov, B. Hillebrands
   submitted to Appl. Phys. Lett..

7.4 Ph.D. theses

1. *Systematik epitaktischer magnetischer Austausch-Verschiebungs-Schichtsysteme*
   Tim Mewes, Ph.D. thesis, Universität Kaiserslautern, Nov. 2002.

2. *Modifikation des Austausch-Verschiebungseffektes in Ferro-/Antiferromagnet-Bilagen durch lagenweise und ortsaufgelöste Ionenbestrahlung*
   Stefan Poppe, Ph.D. thesis, Universität Kaiserslautern, May 2002.

Chapter 8: Conferences, Workshops, Schools and Seminars

(shown in chronological order with the speaker named)

8.1 Conferences

8.1.1 Invited talks

S.O. Demokritov:
Spin wave dynamics in structured magnetic media
Congress American Vacuum Society, Denver, USA, November 2002

B. Hillebrands:
Dynamics in patterned magnetic structures
2002 MRS-Fall-Meeting, Boston, USA, December 2002

J. Fassbender:
Maßgeschneiderte Materialien für die Magnetoelektronik
Symposium “Grundlagenorientierte Materialwissenschaften”,
Universität Braunschweig, Germany, December 2002

B. Hillebrands:
Dynamik in magnetischen Nanostrukturen
DFG-Rundgespräch, Bad Honnef, Germany, March 2003

B. Hillebrands:
Dynamics in magnetic stripes
LEA workshop, Grenoble, France, May 2003

B. Hillebrands:
Fast magnetization dynamics
ICM 2003, Rom, July/August 2003

8.1.2 Contributed talks and posters

5 contribution:	47th Annual Conference on Magnetism and Magnetic Materials Tampa, Florida, USA, November 2002
10 contributions:	DPG-Frühjahrstagung Dresden, Germany, March 2003
1 contribution:	ICMCTF, San Diego, USA, April/May 2003
1 contribution:	E-MRS Tagung, Strasbourg, France, June 2003
4 contributions:	18th ICMFS Conference, Madrid, July 2003
3 contributions:	ICM 2003, Rom, July/August 2003
1 contribution:	Diamond 2003, Salzburg, Austria, September 2003
1 contribution:	FKA 12, Wien, Austria, September 2003
1 contribution:	ECASIA 2003, Berlin, Germany, October 2003
1 contribution:	18th European Conference on Biomaterials, Stuttgart, Germany, October 2003

8.2 Invited colloquia and seminars

S.O. Demokritov:
Dynamics in patterned magnetic stuctures
IBM, New York, USA, November 2002

B. Hillebrands:
Spin waves: a model system to study nonlinear wave propagation and amplification in confined anisotropic materials
CREOLE, University of Central Florida, Orlando, USA, November 2002

J. Fassbender:
Magnetisierungsdynamik und Schaltverhalten von dünnen magnetischen Schichten
FU Berlin, Festkörperphysikalische Kolloquium, December 2002

B. Hillebrands:
Dynamik in magnetischen Mikro- und Nanostrukturen
Universität Münster, Physikalische Kolloquium, Germany, January 2003

S.O. Demokritov:
Spin wave dynamics in structured magnetic media: closer to reality
University of Nebraska, Lincoln, USA, February 2003

S.O. Demokritov:
Spin wave dynamics in strongly non-uniform magnetic fields
University of Ferrara, Italy, March 2003

T. Wittkowski:
Brillouin-Lichtstreuung zur Charakterisierung elastischer und struktureller Eigenschaften dünner Schichten
Universität Chemnitz, Germany, March 2003

T. Wittkowski:
Untersuchung dünner Schichten mittels Brillouin-Streuung
Fachhochschule Mittweida, Germany, March 2003

T. Wittkowski:
Brillouin-Lichtstreuung zur Charakterisierung elastischer und struktureller Eigenschaften dünner Schichten
Institut für Physik, TU Chemnitz, Germany, May 2003

C. Bayer:
Spin wave dynamics in structured magnetic media
University of Minnesota, MRSEC-Seminar, USA, May 2003

B. Hillebrands:
Dynamics in magnetic stripes
Festkolloquium anlässlich des 60. Geburtstags von Prof. Dr. Gernot Güntherodt, RWTH Aachen, Germany, May 2003

B. Hillebrands:
Dynamik in magnetischen Mikro- und Nanostrukturen
Universität Göttingen, Physikalisches Kolloquium, Germany, May 2003

J. Fassbender:
Funktionale magnetische Schichten - neue Möglichkeiten durch Ionenbestrahlung
Forschungszentrum Rossendorf, Dresden, Germany, August 2003

8.3 Invited lectures

S.O. Demokritov:
Magnetic dynamics in structured systems
University of Perugia, Italy, March 2003

J. Fassbender:
Basics of magnetization dynamics
Training days of the EU-RTN network ULTRASWITCH, Leuven, Oct. 9 – 10, 2003

8.4 Contributions to other meetings

S. Poppe:
Maßgeschneiderte magnetische Materialien
3. Ionenstrahlmeeting, Stuttgart, Germany, November 2002

J. Fassbender:
Konzepte zum Schalten der Magnetisierung - ein Weg zu schnelleren magnetischen Speichern
DFG-Graduierten-Kolleg ”Nichtlineare Optik und Ultrakurzzeitphysik”, Kaiserslautern, Germany, June 2003

J. Fassbender:
Magnetische Strukturierung mittels Ionenstrahlen
Universität Augsburg, Germany, June 2003

J. Fassbender:
Dünne magnetische Schichten
IFOS Kaiserslautern, Germany, July 2003

J. Fassbender:
Magnetische Strukturierung mittels Ionenstrahlen
Ionenstrahlmeeting Dresden, September 2003

T. Wittkowski:
Brillouin-Lichtsteuung zum Nachweis akustischer Oberflächenphononen in BN-beschichteten dünnen Fasern
10th c-BN Expert Meeting, Mittweida, Germany, October 2003

Appendix: Impressions from our Group Ceremonies

Ph.D. defense Dr. Tim Mewes

Ph.D. defense Dr. Stefan Poppe

Retirement Dr. Kurt Jung